



# The Morganton Scientific

North Carolina School of Science and Mathematics

Journal of Student STEM Research

<https://doi.org/10.62329/YGNY9127>

## Table of Contents

- 3 *Words from the Editors*
- 4 *Analyzing Carbon-13 NMR Spectra to Predict Chemical Shifts of Carbon Compounds using Machine Learning Algorithms*  
PRANAV AGRAWALA
- 9 *Age Determination of NGC 1952 and PSR B0531+21 Using Radio Observations*  
SYDNEY COVINGTON
- 13 *Using Bromelain Application to Inhibit the Spread of the Tobacco Mosaic Virus and Promote Tissue Regeneration in Red Bell Pepper Plants*  
CHISOM DURU
- 18 *A Novel Approach to Inhibit MAP2K1 Overexpression Present in Melorheostosis Utilizing Moringa oleifera Extracts*  
ASHMITH GUDUDURU
- 24 *Inhibition of TORC1 Pathway in Saccharomyces Cerevisiae to Induce Autophagy Using Graphene Oxide*  
SESHA JONNAVITHULA
- 29 *Assessing the Impact of Water, Algae, Alcohol, and Oil-Based Inks on the Biodegradability of Cellulose in Filter Paper*  
PRERANA KULLA, SOPHIA SOLOMON
- 34 *An Investigation of the Economics Behind Air Emergency Medical Services*  
NOAH LANGBO
- 38 *Predicting Network Traffic Flow with a Multi-Layer Short-Term Memory Model*  
TARAN PUVVALA
- 45 *AQINet: A multimodal deep convolutional neural network to predict Air Quality Index via satellite imagery and meteorological data*  
ZOAIB SIHWALA
- 50 *An Analysis on Genomic Correlation for Gallstone Susceptibility*  
SANJITA SRINATH
- 59 *Effect of Sulfakinin/Cholecystokinin-type Peptide ArSK/CCK1 on Satiety and Energy Metabolism of Asterias vulgaris*  
CAROLINE ZHANG

## Words from the Editor

Welcome to the *Morganton Scientific*, the first edition of the STEM research journal at the North Carolina School of Science and Mathematics in Morganton, North Carolina. This journal showcases student research spanning a variety of fields, including Biology, Chemistry, Engineering, Physics, Computer Science, Mathematics, and interdisciplinary topics.

As members of the first graduating class of NCSSM-Morganton, we filled the blank pages with new stories and milestones that have and will shape our high school career and beyond. During these two years, we've embarked on a new journey together with Mrs. Jennifer Williams, the Chair of Science and advisor of *Morganton Scientific*. Although we initially only knew of each other, through our collaborations in establishing this journal and bonding over our love for science communication, all of us have reflected upon the true meaning of being inaugural.

Fittingly, this year's theme is DNA. Just as DNA establishes the underlying code for life, we hope this journal will establish a new beginning in encouraging students to explore the sciences, at NCSSM, the greater community of North Carolina, and more. Our hope is that students from all around read this journal and are inspired to come to NCSSM and/or discover the world of research.

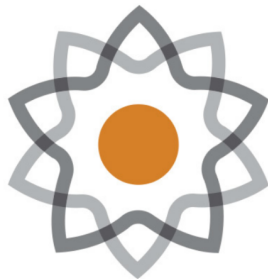
A novel way to showcase research, the *Morganton Scientific* is only the start of the journey. We hope that future years are able to add on to this product, and as DNA mutates and evolves, the journal will as well.

As a journal by and for emerging scientists, it was important to us that we created a medium that progressed with the scientific community. As open science is becoming further integrated into how we share our research, *Morganton Scientific* wanted to follow this example by using MyST, an open-source tool designed to make research transparent, accessible, and inclusive. MyST allows us to make our pieces machine readable, and thus more accessible to online queries. It enables us to be transparent about the research we share, as we can include the data sets or code used for each experiment, making them more easily reproducible. We would like to thank Mr. Taylor Gibson for introducing us to this amazing tool and giving us his time and expertise to help launch the online portion of this journal.

Finally, we would like to give a special thank you to Ms. Jennifer Williams, Dr. Amy Sheck, Mr. Taylor Gibson, Rowan Cockett, Dr. Jonathan Bennett, and Mr. Kevin Baxter for their continuous support in the creation of this journal.

Bianca Chan, Kovida Vupputuri, Lara Dincer, Tanvi Sharma, and Rachel Joel

Founding Editors



# Analyzing Carbon-13 NMR Spectra to Predict Chemical Shifts of Carbon Compounds using Machine Learning Algorithms

Pranav Agrawala<sup>1</sup> 

<sup>1</sup>North Carolina School of Science and Mathematics 

## The Morganton Scientific

North Carolina  
School of Science and  
Mathematics

Journal of Student STEM Research

### Abstract

Nuclear Magnetic Resonance (NMR) is a fundamental tool in chemistry for elucidating the molecular structure of unidentified substances. The evaluation of  $^{13}\text{C}$  NMR spectra can be challenging due to the numerous factors that affect the peaks and their locations (chemical shifts). Chemists can use NMR spectroscopy in synthesizing new molecules to confirm the identity of the molecule produced. Since the NMR spectrum for the molecule does not exist, the chemists cannot compare their spectra with preexisting spectra to verify their results. To address this, an algorithm that predicts the chemical shifts of the  $^{13}\text{C}$  NMR spectra for compounds based on their molecular structure emerges as a solution, generating artificial spectra for comparison with real ones. This paper delineates a method to formulate such an algorithm using machine learning techniques. Multiple graph neural networks and a classical neural network underwent training on an NMR database to predict the chemical shifts of the  $^{13}\text{C}$  NMR spectra for several molecules. The accuracy of each neural network was tested by analyzing the difference between the predictions and the actual chemical shift values in the database using Mean Absolute Error (MAE). Notably, the graph neural networks had a higher accuracy and precision than the classical neural network. Among them, the Graph Transformer Network emerges as the most proficient performer. Chemists can utilize the Graph Transformer Network model to validate the synthesis of new compounds within a margin of error of approximately 2.599 ppm.

**Keywords** Nuclear Magnetic Resonance, Carbon-13, Machine Learning

### 1. INTRODUCTION

Nuclear magnetic resonance (NMR) spectroscopy is an effective technique to deduce the molecular structure of a chemical compound. The NMR machine produces a spectrum that can be used in the process of structure elucidation. To predict the molecular structure, the relevant spectral features of the graph, such as the peak locations (chemical shifts), splitting pattern of the peaks, and the integration of the peaks, must be extracted and analyzed [1]. Interpreting the meaning behind the spectral features of the graph can help determine the structure of the molecule as the spectral features are affected by electron deshielding from electronegative atoms, magnetic anisotropy from pi bonds, and hydrogen bonding [1]. However, the process of unraveling the spectral features of the NMR spectra based on the molecular structure of the sample can be complex as there are many factors that affect the peaks of the NMR spectra. Machine learning algorithms can be used to predict the spectral features of the NMR spectra of an organic compound based on its chemical structure [2]. The algorithm would learn the relationship between atoms and bonds in a molecule, and how it affects the NMR spectra of that molecule. Simple neural network algorithms simplify molecules by encapsulating each atom's features within a vector, albeit at the cost of losing significant information about interatomic interactions. However, a more effective approach to representing molecules for machine learning algorithms emerges with the utilization of graphs [2]. The graph is composed of nodes, which represent the atoms, that are connected by edges, which represent the bonds between atoms. A graph neural network is a machine learning algorithm that can be used to simulate a compound by mapping out the molecular structure of the compound on a graph. Furthermore, they can be used to predict the chemical shifts of  $^{13}\text{C}$  NMR

Published Jun 27, 2024

Correspondence to  
Pranav Agrawala  
[agrawala24a@nccsm.edu](mailto:agrawala24a@nccsm.edu)

Open Access   
Copyright © 2024 Agrawala. This is an open-access article distributed under the terms of the Creative Commons Attribution 4.0 International license, which enables reusers to distribute, remix, adapt, and build upon the material in any medium or format, so long as attribution is given to the creator.

spectra for carbon compounds more accurately than a classic neural network [2]. The graph neural network algorithm can help scientists while they are producing a new compound as they could use the algorithm to verify if they made the correct compound. Previous studies have shown that graph neural networks are effective in predicting the chemical shifts of <sup>13</sup>C NMR spectra [2]. In this study, I aim to further improve the accuracy of the graph neural networks by introducing novel architectural frameworks that incorporate comprehensive data from both nodes and edges within each graph. The algorithm is tested by comparing the actual chemical shift values of <sup>13</sup>C NMR spectra with the predicted chemical shift values from the algorithm for various carbon compounds. The actual chemical shift values of the <sup>13</sup>C NMR spectra is obtained from the *NMRShiftDb2* database.

## 2. METHODS

### 2.1. Data Preprocessing

The dataset used in this paper is the *NMRShiftDB2* database, which contains the NMR spectra data for 17,473 unique molecules. Some molecules have spectral data for <sup>13</sup>C NMR spectra, other molecules have spectral data for <sup>1</sup>H NMR spectra, while the rest of them have spectral data for both <sup>13</sup>C NMR and <sup>1</sup>H NMR spectra. Since I am only analyzing <sup>13</sup>C NMR spectra, I went through the database and removed the molecules that do not have data for <sup>13</sup>C NMR spectra. Only 7,304 molecules in the dataset had data for <sup>13</sup>C NMR spectra.

Each molecule in the dataset is represented as a graph to be used by the different graph neural networks. The nodes of a graph represent the different atoms in a molecule and the edges of a graph represent the bonds between each atom in a molecule. Let  $e_{i,j}$  represent an edge of a graph where  $i$  represents the initial node and  $j$  represents

Node Feature	Data Type
Atomic Number	Integer (1-118)
Number of Neighbors	Integer
Formal Charge	Integer
Hybridization	One-hot encoded ( $sp$ , $sp^2$ , $sp^3$ , $sp^3d^1$ , $sp^3d^2$ )
Aromaticity	One-hot encoded (yes, no)
Total Numer of Hydrogens	Integer
Number of Radical Electrons	Integer
In Ring	One-hot encoded (yes, no)
Chirality	One-hot encoded (clockwise, counterclockwise, no)

Table 1. Node features

Edge Feature	Data Type
Bond Type	One-hot encoded (single, aromatic, double)
In Ring	One-hot encoded (yes, no)
Is Conjugated	One-hot encoded (yes, no)

Table 2. Edge Features

the terminal node. Since the bonds in a molecule are undirected, the edges in the graph are also undirected, so  $e_{i,j} = e_{j,i}$ . I went through each bond in the molecule and noted the indices of the atom in the bond using two  $1 \times 2$  arrays and combined them in one array in the format,  $[[i, j], [j, i]]$ . The edge indices are extracted using the RDKit Python library by using the SMILES string of each molecule. The SMILES string encodes the molecular structure of a compound in a string object for the computer to read it. I combined all the edge indices in one matrix and stored it in a `torch.Tensor` object using the PyTorch Geometric Python library.

Let  $n$  represent a node in a graph. Each node in a graph has nine node features stored in a  $1 \times 9$  array. The different node features can be shown in Table 1. All the node features are extracted using the RDKit Python library by using the SMILES string of each molecule. The different node feature arrays for each graph are combined into a multidimensional matrix `torch.Tensor` object using the PyTorch Geometric Python library. Let  $N$  represent the multidimensional matrix whose dimensions are the (number of atoms in the molecule)  $\times 9$ . The matrix  $N$  contains all the node features in a molecule such that  $n \in N$ .

In Figure 1 the selected node  $n_1$  illustrates an example of a node feature array with nine elements. The elements refer to the features in Table 1. The selected edge  $e_{1,2}$  shows an example of an edge feature array with three elements and an adjacency list with two  $1 \times 2$  arrays. The elements in the edge feature array refer to the features in Table 2. There are two arrays for every edge as they are undirected. Each node is labeled with a 0 or 1, where 0 represents the node is not carbon and 1 represents the node is carbon. The binary values are stored in the mask array.

Let  $e$  represent an edge in a graph. Each edge in a graph has three edge features stored in a  $1 \times 3$  array. The different edge features can be shown in Table 2. All the edge features are extracted using the RDKit Python library by using the SMILES string of each molecule. The different edge feature arrays for each graph are combined into a multidimensional matrix `torch.Tensor` object using the PyTorch Geometric Python library. Let  $E$  represent the multidimensional matrix whose dimensions are the (number of atoms in the molecule)  $\times 3$ . The matrix  $E$  contains all the edge features in a molecule such that  $e \in E$ .

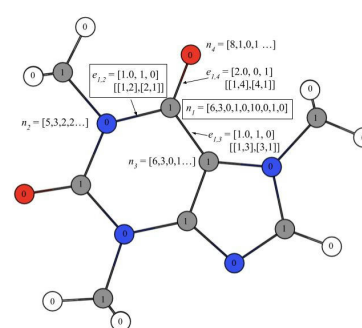


Figure 1. Example of a Molecular Graph

While going through the atoms in the molecule, I stored the atom indices of carbon atoms in an array where the integer 1 indicated that the atom is carbon and the integer 0 indicated that the atom is not carbon. These arrays are called masks and it helps the graph neural networks to identify the nodes that represent the NMR-active atoms in a molecule. The mask array is stored in a *torch.Tensor* object. Let  $m$  represent the mask array whose dimensions are the ‘ $1 \times$  number of atoms in the molecule’. After obtaining all the *torch.Tensor* objects for a molecule, I created an object for each graph that combined the *torch.Tensor* objects for node features, edge features, edge indices, and masks to be used as input for the graph neural networks. Figure 1 shows an example of how the molecules are encoded into graphs where each node and edge represent the atoms and bonds respectively, and each node is labeled with a binary mask to determine whether an atom is carbon or not (Figure 1).

## 2.2. Graph Neural Networks

To predict the chemical shifts of  $^{13}\text{C}$  NMR spectra for carbon compounds, I utilized several different types of graph neural networks. The graph neural networks take in the graphs of the different molecules as the input and output an array of the predicted chemical shifts with size  $1 \times (\text{number of atoms in the molecule})$  for each molecule. The neural networks used Mean Absolute Error (MAE) to calculate the loss for the chemical shifts by subtracting the predicted chemical shifts with the actual chemical shifts and taking the absolute value of the difference. Then, the neural networks find the average error of all the chemical shifts for every molecule in a set. The following equation describes how MAE is calculated:

$$L = \frac{\sum_{m \in D} \sum_{y_a \in m} |y_p - y_a|}{\sum_{m \in D} \sum_{y_a \in m} a} \quad (1)$$

where  $D$  is a set of molecules,  $m$  is a molecule in the set  $D$ ,  $y_a$  is the actual chemical shift of one atom in the molecule  $m$ , and  $y_p$  is the predicted chemical shift for that one atom. After each layer in the graph neural networks, a layer normalization, dropout, and ReLU function is applied to the data, respectively. The layer normalization transforms the data to be on a similar scale and is used to stabilize and speed up the training process [3]. The dropout function randomly ignores a certain number of nodes in the next layer to prevent overfitting in the graph neural network [4]. The ReLU function ensures nonlinearity and prevents the gradients in the graph neural networks from becoming too small by removing negative values in the data.

## 2.3. Graph Transformer Network

One of the graph neural networks used was a Graph Transformer Network. The Graph Transformer Network is a specific type of graph neural network that updates the node features of one node based on the features of its neighboring nodes. The neural network performs an Equation 2 that combines the node features of one node with the node features of its neighboring nodes. For the Graph Transformer Network used in this paper, I took the sum of the node features of the neighboring nodes. Along with the aggregation function, the Graph Transformer Network uses a Equation 3 that performs a dot product with the neighboring node features to determine which of the neighboring nodes are important for the

chemical shift prediction. The weights for the self-attention mechanism is learnable and it gets updated as the Graph Transformer Network is training. In addition to the aggregation function and self-attention mechanism, the Graph Transformer Network multiplies more learnable weights to the node being updated and its neighboring nodes.

The following equation shows how the Graph Transformer Network updates each node in a graph [5]:

$$x'_i = W_1 x_i + \sum_{j \in N(i)} \alpha_{i,j} \cdot W_2 x_j \quad (2)$$

where  $x_i$  is the node before being updated,  $N(i)$  is the neighboring nodes,  $\alpha_{i,j}$  is the self-attention mechanism, and  $W_1$  &  $W_2$  are the learnable weights multiplied to each node. The Graph Transformer Network determines the learnable self-attention mechanism using the following function [5]:

$$\alpha_{i,j} = \text{softmax} \left( \frac{(W_3 x_i)^T (W_2 x_j)}{\sqrt{d}} \right) \quad (3)$$

where  $x_i$  is the node before being updated,  $x_j$  is a neighboring node, and  $W_3$  &  $W_4$  are the learnable weights multiplied to each node in the self-attention mechanism. The softmax function normalizes the self-attention mechanisms from all the neighboring nodes to have a sum of 1. The self-attention mechanism divides by  $\sqrt{d}$  inside the softmax function to maintain a standard normal distribution by keeping a variance of one and mean of zero.

## 2.4. Graph Attention Network

One of the other graph neural networks used in this paper is the Graph Attention Network. The Graph Attention Network is similar to the Graph Transformer Network, except that it uses different functions (Equations Equation 4 & Equation 5) to update each node and calculate the self-attention mechanisms.

The Graph Attention Network uses the following function to update each node in the graph [5]:

$$x'_i = \alpha_{i,j} \cdot W x_i + \sum_{j \in N(i)} \alpha_{i,j} \cdot W x_j \quad (4)$$

where the learnable weights are the same throughout the entire function instead of the function for the Graph Transformer Network that uses two different learnable weights. The Graph Attention Network also applies a dot product to the self-attention mechanism and the node being updated.

The Graph Attention Network uses the following function to calculate the self-attention mechanism [5]:

$$\alpha_{i,j} = \frac{\exp(\text{LeakyReLU}(a^T (W x_i || W X_j || W_2 e_{i,j})))}{\sum_{k \in N(i)} \exp(\text{LeakyReLU}(a^T (W x_i || W X_k || W_2 e_{i,k})))} \quad (5)$$

where  $e_{i,j}$  is the edge feature of the edge connecting nodes  $x_i$  and  $x_j$ ,  $W_2$  is the learnable weights for the edge features, and  $a$  is the learnable attention vector that determines the weight of each neighboring node. The LeakyReLU function has the same functionality as the ReLU function, but allows for negative values at

a low magnitude [6]. The  $\exp()$  function is used to normalize the self-attention mechanisms instead of the softmax function in the Graph Transformer Network, and gets rid of negative values. The  $\|$  operation in the function concatenates the three arrays.

### 2.5. Graph Convolution Network

The last graph neural network used in this paper is the Graph Convolutional Network (GCN). The GCN is different from the Graph Attention Network and Graph Transformer Network as it does not have a self-attention mechanism and uses a different function to update the nodes in a graph. The GCN updates nodes in the graph using the following function [5]:

$$x'_i = W^T \sum_{j \in N(i)} \left( \frac{e_{i,j}}{\sqrt{E_i E_j}} \right) \quad (6)$$

where

$$E_i = 1 + \sum_{j \in N(i)} (e_{i,j}) \quad (7)$$

where  $e_{i,j}$  is the edge feature of the edge connecting nodes  $x_i$  and  $x_j$ . The GCN only uses the edge features in the graph and does not consider the features of the neighboring nodes. The GCN is less complex than the Graph Attention Network and Graph Transformer Network as it uses less data from the graph and only has one set of learnable weights.

### 2.6. Training, Validation, and Testing

The training, validation, and testing of the graph neural networks were performed by splitting the dataset into 80, 10, and 10 percent for the training, validation, and test sets, respectively. Then, the training, validation, and test sets were split into equal size batches for the graph neural networks to be trained faster. The graph neural networks went through one hundred epochs during the training process, where each epoch iterated through the entire training set once. In order to ensure that the loss was decreasing, at the end of each epoch, the graph neural networks went through the validation set and printed the average loss from the validation set using MAE. At the end of the one hundred epochs, the graph neural networks went through the test set and printed the average loss from the test set using MAE to determine the performance of each graph neural network.

## 3. RESULTS AND DISCUSSION

The different graph neural networks were tested several times to determine the graph neural network with the best performance. The Multi-Layer Perceptron (MLP) is a classical neural network model that does not use graphs as input [7]. I used the MLP as a benchmark test for the other graph neural networks to compare the performance of graph neural networks with regular neural networks. To assess the neural networks, I ran each neural network 10 times through the training, validation, and test cycle. In each trial, I randomized the seed for weight initialization to obtain a range of values for the test loss using MAE (Equation 1). The results of each neural network can be seen in Table 3. The test loss values for each neural network represents the average test loss over the 10 trials, plus or minus the standard deviation. The results

show that the Graph Transformer Network has the best performance compared to the other neural networks. The average test loss for the Graph Transformer Network was 2.599 ppm, which is not better than the existing graph neural networks from previous works but is close [2]. The loss is significantly low as the  $^{13}\text{C}$  NMR spectra has chemical shift values ranging from 0 ppm to 220 ppm. The other graph neural networks passed the benchmark test by having lower average test losses than the Multi-Layer Perceptron neural network. This proves that graph neural networks are superior to classic neural networks in predicting the chemical shifts of  $^{13}\text{C}$  NMR spectra for carbon compounds. The difference in test loss between the Graph Convolutional Network and the other two graph neural networks shows that the self-attention mechanisms greatly improve the performance of the graph neural networks. The increased accuracy of the Graph Transformer Network over the Graph Attention Network reveals that using more sets of learnable weights improves the performance of the graph neural network. The plots in Figures Figure 2, Figure 3, Figure 4, and Figure 5 further demonstrate the performance of the Graph Transformer Network over the other neural networks for predicting the chemical shifts of  $^{13}\text{C}$  NMR spectra (Fig. Figure 2, Figure 3, Figure 4, and Figure 5).

For plot (a) in Figures Figure 2, Figure 3, Figure 4, and Figure 5, the neural network is more accurate if the data is closer to the line,  $y = x$  (Fig. Figure 2, Figure 3, Figure 4, and Figure 5). The Graph Transformer Network is the most accurate while the Multi-Layer Perceptron is the least accurate. Also, the Graph Attention Network is more accurate than the Graph Convolutional Network. The variance of the data in the plots in Figures Figure 2, Figure 3, Figure 4, and Figure 5 reveal the preciseness of each neural network (Fig. Figure 2, Figure 3, Figure 4, and Figure 5). The Graph Transformer Network is the most precise with 2.74% of its data being outliers, and the Multi-Layer Perceptron is the least precise with 39.98% of its data being outliers. The Graph Attention Network is more precise than the Graph Convolutional Network as 11.91% of the data from the Graph Attention Network are outliers and 31.76% of the data from the Graph Convolutional Network are outliers. The test loss numbers in Table 3 explains the pattern above as the Graph Transformer Network has the lowest test loss and the Multi-Layer Perceptron has the highest test loss. The plot (b) in Figures Figure 2, Figure 3, Figure 4, and Figure 5 shows the accuracy of the neural networks for predicting the chemical shifts of  $^{13}\text{C}$  NMR spectra for molecules with varying 8 amounts of atoms (Fig. Figure 2, Figure 3, Figure 4, and Figure 5). The plot shows that the neural networks can more accurately predict the chemical shift values of  $^{13}\text{C}$  NMR spectra for molecules containing more atoms. This is due to the increase in data for each molecule as the atoms increase, causing the neural networks to produce more accurate predictions.

Neural Network	Test Loss (ppm)
Graph Transformer Network	$2.599 \pm 0.3169$
Multi-Layer Perceptron	$9.152 \pm 2.543$
Graph Convolutional Network	$8.639 \pm 1.619$
Graph Attention Network	$4.488 \pm 1.379$

Table 3. Performance of Neural Networks

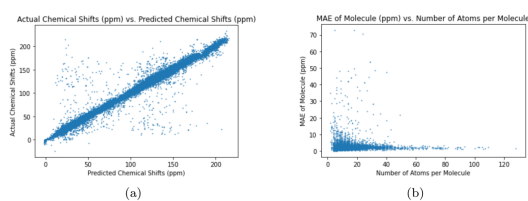


**Figure 2.** Performance of Graph Transformer Network

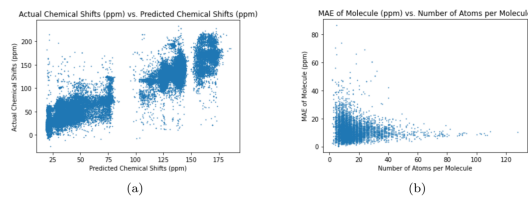


**Figure 3.** Performance of Multi-Layer Perceptron

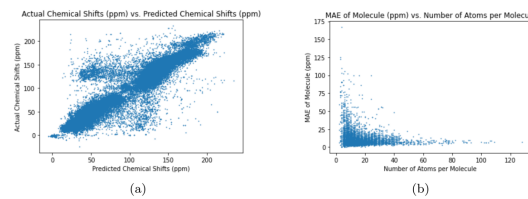


**Figure 4.** Performance of Graph Convolutional Network

## 4. CONCLUSION

In this study, I predicted the chemical shifts of  $^{13}\text{C}$  NMR spectra for carbon compounds using neural networks aiming to assist chemists with confirming the synthesis of new compounds. Leveraging a database of molecules with the chemical shifts of their associated  $^{13}\text{C}$  NMR spectra, I trained and tested the neural networks. These encompassed three different types of graph neural networks and a classical neural network to test whether the graph neural networks can perform better than the classical neural network. I encoded each molecule in a graph, where the nodes are the atoms of the molecules and the edges are the bonds between the atoms, as input for the graph neural networks. I used MAE to evaluate the performance of each neural network. The Graph Transformer Network had a MAE of 2.599 ppm, the Multi-Layer Perceptron had a MAE of 9.152 ppm, the Graph Convolutional Network had a MAE of 8.639 ppm, and the Graph Attention Network had a MAE of 4.488 ppm. The Graph Transformer Network had the best accuracy for predicting the chemical shifts and all three of the graph neural networks performed better than the classical neural network.

The performance of the Graph Transformer Network is not superior but is close to the performance of existing methods, which has a

MAE of 1.355 ppm [2]. The model for the Graph Transformer Network can be used by chemists for verifying the synthesization of new molecules. The performance of the neural networks can be improved by training them with a larger database. For future work, I can test the algorithm for predicting the chemical shifts of other types of NMR spectra and improve the performance of the graph neural by utilizing different architectures.

## REFERENCES

- [1] I. P. GEROTHANASSIS, A. TROGANIS, V. EXARCHOU, and K. BARBAROSSOU, “NUCLEAR MAGNETIC RESONANCE (NMR) SPECTROSCOPY: BASIC PRINCIPLES AND PHENOMENA, AND THEIR APPLICATIONS TO CHEMISTRY, BIOLOGY AND MEDICINE,” *Chem. Educ. Res. Pract.*, vol. 3, no. 2, pp. 229–252, 2002, doi: [10.1039/b2rp90018a](https://doi.org/10.1039/b2rp90018a).
- [2] Y. Kwon, D. Lee, Y.-S. Choi, M. Kang, and S. Kang, “Neural Message Passing for NMR Chemical Shift Prediction,” *Journal of Chemical Information and Modeling*, vol. 60, no. 4, pp. 2024–2030, 2020, doi: [10.1021/acs.jcim.0c00195](https://doi.org/10.1021/acs.jcim.0c00195).
- [3] J. L. Ba, J. R. Kiros, and G. E. Hinton, “Layer Normalization.” [Online]. Available: <https://arxiv.org/abs/1607.06450>
- [4] N. Srivastava, G. Hinton, A. Krizhevsky, I. Sutskever, and R. Salakhutdinov, “Dropout: A Simple Way to Prevent Neural Networks from Overfitting,” *Journal of Machine Learning Research*, vol. 15, no. 56, pp. 1929–1958, 2014, [Online]. Available: <http://jmlr.org/papers/v15/srivastava14a.html>
- [5] M. Fey and J. E. Lenssen, “Fast Graph Representation Learning with PyTorch Geometric.” [Online]. Available: <https://arxiv.org/abs/1903.02428>
- [6] B. Xu, N. Wang, T. Chen, and M. Li, “Empirical Evaluation of Rectified Activations in Convolutional Network.” [Online]. Available: <https://arxiv.org/abs/1505.00853>
- [7] F. Murtagh, “Multilayer perceptrons for classification and regression,” *Neurocomputing*, vol. 2, no. 5–6, pp. 183–197, 1991, doi: [10.1016/0925-2312\(91\)90023-5](https://doi.org/10.1016/0925-2312(91)90023-5).

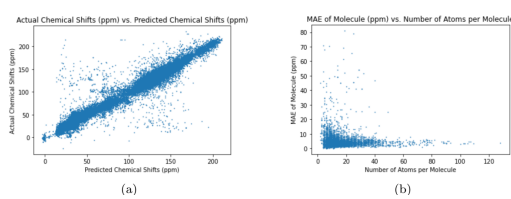
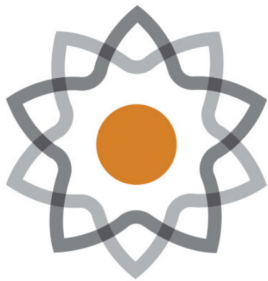


**Figure 5.** Performance of Graph Attention Network



# Age Determination of NGC 1952 and PSR B0531+21 Using Radio Observations

Sydney Covington<sup>1</sup> 

<sup>1</sup>North Carolina School of Science and Mathematics 

## The Morganton Scientific

North Carolina  
School of Science and  
Mathematics

Journal of Student STEM Research

### Abstract

Supernova remnants (SNRs) and pulsars (PSRs) are highly related phenomena: Both can be produced from the same cosmic explosion. NGC 1952 and B0531+21, or the Crab SNR and PSR, are a verified pair. This research uses two strategies to estimate the ages of young SNRs and evaluates their reliability. The first strategy relies on the remnant's expansion rate and radius to determine a convergence date. We operated the Green Bank Observatory 20-meter radio telescope in high-resolution mode to obtain spectra over a high-pass filter at a central frequency of 1420 MHz. While the data depicted a clear 21 cm hydrogen line, the Doppler calculation resulted in a meager expansion rate, which we found inadequate for subsequent age calculations. Second, due to the pulsar's gradual loss of rotational energy over time, its period and period derivatives allowed us to extrapolate a formation date. We adjusted the telescope to low resolution at 1395 MHz. Age determinations reveal stages in SNR life cycles and support or disprove SNR-PSR associations. Several factors, including background radio interference, could impact the spectrum scans. However, the pulsar data produced an actual age within 50 years of the supernova's verified explosion, confirming this method's relative accuracy.

**Keywords** Supernova Remnants, Pulsars, Age Determination

### 1. AGE DETERMINATION OF NGC 1952 AND PSR B0531+21 USING RADIO OBSERVATIONS

Supernova remnants (SNRs) have been astronomical phenomena of interest since ancient times due to their brilliance in the visible spectrum. SNR events are evidenced in the artifacts of early civilizations. Records are believed to have begun in 185 C.E. Common type II supernovae occur due to the discontinuation of fusion in massive stars' iron or nickel cores. However, in type III1 supernovae, the atomic nuclei of oxygen-neon-magnesium cores capture electrons. Both processes drive stellar collapse because of imbalances between gravity and pressure. Protons and electrons meld, forming a small, dense star supported by neutron degeneracy (more massive stars continue to collapse into black holes). Finally, this process produces a shock wave that expands inward and outward—expelling an array of gas and dust in the interstellar medium. Pulsars (PSRs), a form of a neutron star, rotate at extremely high velocities. Although they conserve much of their angular momentum, their periods gradually decline. Pulsars are detectable in gamma, x-ray, ultraviolet, or radio wavelengths due to the emission of synchrotron radiation from their magnetic poles.

A PSR's characteristic age can be deduced from its period and derivative. The characteristic age assumes significant reductions in the initial period and an absence of magnetic field decay. Its accuracy indicates the relevance of these characteristics. The actual age, meanwhile, uses a pulsar's braking magnitude and reveals whether multiple sources affect its spin-down.

The Crab Nebula, a remnant of a supernova and a type III plerion located within the constellation Taurus, and its associated pulsar are the subjects of this research. Age determinations assist historians in connecting SNRs to Chinese records of "guest stars." However, we focus on the Crab because of sufficient evidence from the year it was first observed, proving the accuracy of our results. Additionally, ages confirm pulsar associations: A pulsar may gradually drift from a remnant's center [1]. We compare

Published Jun 27, 2024

Correspondence to  
Sydney Covington  
[covington24s@nccsm.edu](mailto:covington24s@nccsm.edu)

Open Access 

Copyright © 2024 Covington. This is an open-access article distributed under the terms of the Creative Commons Attribution 4.0 International license, which enables reusers to distribute, remix, adapt, and build upon the material in any medium or format, so long as attribution is given to the creator.

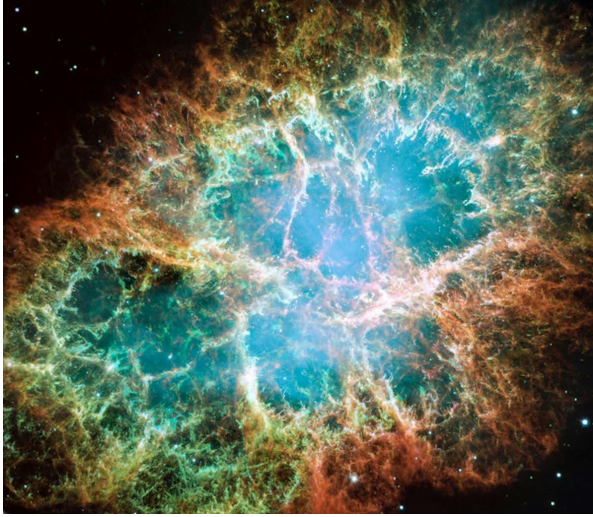


**Figure 1.** An optical image of the NGC 1952 taken by the Hubble Space Telescope in 2005. The central glow highlights the pulsar.

two methods in their effective determination of the Crab SNR's age: The first utilizes the remnant's expansion, and the second relies on the spin properties of its pulsar.

## 2. METHODS

Initially, our research relied on the operation of the Pisgah Astronomical Research Institute's 12-m radio telescope. We sought to measure the diameter of the remnant using multiple continuum scans. However, the telescope could not produce these scans due to the SNR's uneven distribution of hydrogen gas, nor was its data acquisition system designed to detect fast pulsars.

### 2.1. Radio Observations

The Green Bank 20-m radio telescope with an L-band receiver (1.15-1.73 GHz) was used for all original observations.

#### 2.1.1. Telescope Settings: SNR Data:

We produced two spectrum scans of the Crab SNR to estimate its expansion rate. This approach relied on measuring the Doppler shift of the hydrogen 21 cm emission line (with a precise frequency of 1420.406 MHz) and assumed that the shell had undergone no acceleration while dispersing from a point. The pulsar's energy input, combined with the shell's evolving interaction with the interstellar medium, would cause numerous complications [2]. We pulled frequency values from the minimum coordinates of the spectral features displayed by our scans and averaged the corresponding pairs. We then substituted these values into Equation [Equation 1](#) to find a velocity difference for the slightly redshifted and blueshifted radio waves (due to the nearer approaching side of the shell and the further receding side). Finally, with measurements for the expansion velocity, we aimed to estimate a convergence date from the radio size of the remnant.

$$\Delta v = \frac{\Delta v}{v} \times C \quad (1)$$

#### 2.1.2. Telescope Settings: PSR Data:

Run	Object	Coordinates and Apparent Magnitude	Time of Observation (UT)	Date
1	NGC 1952	RA 05:35:54.67 DEC 22:01:49.1 Mag. 8.4	17:51:05	2023-06-27
2	NGC 1952	RA 05:35:54.67 DEC 22:01:49.1 Mag. 8.4	21:02:37	2023-07-01
3	B0531+21	RA 05:34:31.9 DEC 22:00:52.1 Mag. 16.5	19:00:04	2023-07-24
4	B0531+21	RA 05:34:31.9 DEC 22:00:52.1 Mag. 16.5	20:01:56	2023-07-25
5	B0531+21	RA 05:34:31.9 DEC 22:00:52.1 Mag. 16.5	19:09:29	2023-07-26

**Table 1.** A summary of completed observing runs for the supernova remnant NGC 1952 and pulsar B0531+21.

We conducted three scans of PSR B0531+21, as described in [Table 2](#), to determine the approximate period. Green Bank's systems produced the data in processed Prepfold Plots [Figure 2](#). Due to the spin-down of the pulsar, the period,  $P$ , gradually decreases over many years. The period derivative,  $\dot{P}$ , describes this change. We found  $\dot{P}P$  using the Prepfolds, as well as a recorded period from the Jodrell Bank Observatory in 1982 [3].

Setting	NGC 1952	B0 531+21
Receiver Mode	Highres	Lowres
Central Frequency (MHz)	1420	1395
Filter	HI	HI
Pattern	Track	Track
Duration (sec)	60	180
Integration Time (sec)	0.5	0.0001
Number of Channels	1024	1024
Min. Sun Separation (degrees)	12	0
Min. Elevation (degrees)	20	20

**Table 2.** Control parameters for all telescope observations.

## 2.2. Characteristic and True Ages

We calculated the characteristic age, denoted  $\tau_c$ , using Equation [Equation 2](#), which required only the period and period derivative.

$$\tau_c = \frac{P}{2\dot{P}} \quad (2)$$

With Equation [Equation 3](#), we then estimated the true age,  $\tau$ . Unlike the characteristic age, the true age of a pulsar incorporates  $n$ , the magnetic braking index or the loss of rotational energy due to ionized material traveling along the pulsar's magnetic field lines, and  $P_0$ , the initial period upon the formation of the pulsar.

$$\tau = \frac{P}{(n-1)\dot{P}} \times \left[ 1 - \left( \frac{P_0}{P} \right)^{n-1} \right] \quad (3)$$

$$P = kP^{2-n} \quad (4)$$

A differentiated and rearranged form of Equation [Equation 4](#), which describes the relationship between the period, the constant,  $k$ , and the braking index, allowed us to solve for  $n$ :  $n = 2 - \frac{P\ddot{P}}{\dot{P}^2}$ . The derivations of  $\ddot{P}P$  and  $P_0$  require complex models actively being explored. The process is further complicated by numerous glitches or random and disruptive spin-up events experienced by the Crab PSR. However, recent studies have given estimates for  $P_0$  [4], as well as [5] between glitches: values which we use here.

## 3. RESULTS

### 3.1. SNR Rate of Expression

The Crab remnant is composed primarily of hydrogen gas. Neutral hydrogen produces the 21 cm line, which is evident as a sharp emission feature around 1420 MHz [Figure 1](#). The 21 cm undergoes slight dispersion in energy and quickly passes through the Earth's atmosphere, making it observable with little interference. The averages of the spectral features' minima, 1420.16 MHz and 1420.67 MHz, resulted in a total expansion velocity of 108 km/s.

However, the data may have been skewed by various factors. For example, it is possible that the sharp peak was produced by background sources and not the composition of the remnant itself. The Crab SNR has a relatively small angular size (4-8 arcmin) compared with the telescope's wide field of view. We did not produce further scans due to these significant uncertainties, nor did we carry out subsequent age calculations. H. Yang and R. A. Chevalier [6] estimate that the velocities of most shell features range approximately between 1260-1700 km/s. "Daisy" telescope scans process the sky surrounding an object, allowing the observer to discern radio-emitting sources within a set radius. We may implement this method in future trials to recognize sources of error.

### 3.2. PSR Period, Braking, and Age

The pulse profile (top left of [Figure 2](#)) represents the period produced from folded data and reveals recurring signals. The three measurements resulted in an average period of 0.0338149930 seconds. Thus, with the February 15, 1982 record of 0.0332676584 seconds, we found the period derivative to equal  $4.1855 \cdot 10^{-13} \text{ ss}^{-1}$ .

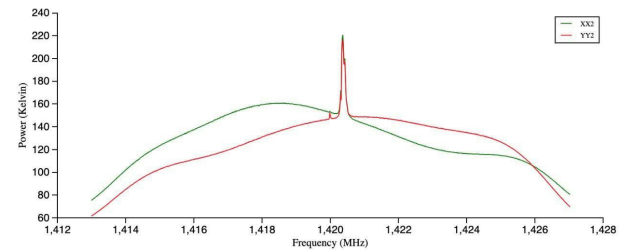


**Figure 2.** A spectrum scan from observing run 1 displaying the linearly polarized components of the signal ( $X2$  and  $Y2$ ), plotted as power ( $K$ ) versus frequency (MHz).

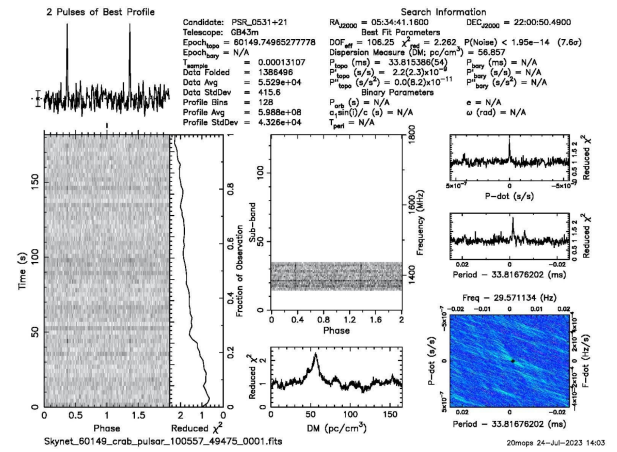


**Figure 3.** A pulsar dataset (compiled by Green Bank into a Preppold Plot) depicting a regular, well-defined signal from observing run 3.

### 3.2.1. Characteristic Age:

We determined the characteristic age to be  $4.0395 \cdot 10^{10}$  seconds or 1280.9 years. For millisecond pulsars, the characteristic age can be many times greater than the actual age, which indicates that  $P_0$  is similar to  $P$ . Although the approximation above is reasonable, the actual age demonstrates higher accuracy. Using Equation [Equation 4](#) and a period second derivative of  $-2.7 \cdot 10^{-24}$ ,  $n$  was found to be 2.52. The braking index is slightly less than the expected value of 3 if the spin-down were due solely to magnetic dipole radiation; therefore, other factors contribute to the pulsar's loss of rotational velocity [7].

### 3.2.2. True Age:

Utilizing Equation [Equation 3](#) and a value of 0.0183 seconds for  $P_0$ , the actual age of B0531+21 is approximately 1020 years. The Crab Supernova was first recorded in July of 1054 C.E., resulting in an actual age of 969.67 years. Lastly, an experimental error of 5% was computed, indicating a relatively accurate result. In comparison, the characteristic age produced an error of 32.09%.

Chinese Sung Dynasty astronomers described the remnant in the Sung Shih annals, and the Japanese documented it in the texts Mei Getsuki and Ichidai, stating, "It shone like a comet and was as bright as Jupiter" [2]. It is also evidenced in a pictographic representation of the ruins of the Anasazi's Peñasco Blanco.

## 4. DISCUSSION AND CONCLUSION

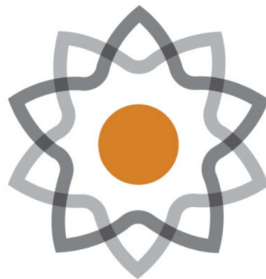
Age determinations derived from spectrum scans of the Crab SNR's radio expansion velocity are impacted by the remnant's competing traits and the likelihood that most of the nebular ejecta does not move directly toward or away from Earth. Considering the possibility of radio frequency interference (RFI), the expansion velocity could be measured more accurately in the visible spectrum. Published high-resolution photographs taken across several decades could also account for the velocities of individual knots. However, R. L. Nugent [8] notes that their optical velocity closely agreed with other published research, indicating a convergence date 76 years after the 1054 C.E. supernova. Meanwhile, M. F. Bietenholz and R. L. Nugent [9] determined that the Crab's inner "synchrotron-emitting bubble," detectable on the radio, expands faster than the outward optical filaments. They reached this conclusion and accounted for the remnant's less prominent features by applying unique scaling techniques to high-resolution radio and optical photographs. The results of the spectrum scans presented here support the need for advanced observing techniques that capture the remnant's asymmetrical geometries and dynamic physical properties.

Meanwhile, despite undergoing glitches, pulsars' compact structures and the benefits of folded data in distinguishing recurring signals from RFI contribute to very accurate time of arrival measurements. We encounter problems considering that many young SNRs do not contain detectable pulsars – perhaps because these pulsars do not emit signals that can be discerned among the remnant's intense radiation. However, at least 20 pairs of plerions and pulsars are known with certainty to exist. Our research conveys that pulsars provide valuable insight into the age and evolution of SNRs. In contrast to expansive nebulae and supernova ejecta, the properties of pulsars make them a very reliable tool for astronomers.

The research presented in this paper was made possible through the generous allocation of resources and equipment by the Green Bank Observatory. I thank Tim DeLisle and Melanie Crowson at the Pisgah Astronomical Research Institute for their invaluable guidance in operating radio telescopes. Additionally, I appreciate James Happer, a physics instructor at The North Carolina School of Science and Mathematics, for his assistance during the initial stages of brainstorming research topics and for providing valuable suggestions in analyzing spectrum data. I also thank Jacob Brown for his insightful advice regarding potential sources of error.

## REFERENCES

- [1] J. Condon, "Essential radio astronomy," *Contemporary Physics*, vol. 58, no. 3, pp. 278–279, 2017, doi: [10.1080/00107514.2017.1312538](https://doi.org/10.1080/00107514.2017.1312538).
- [2] J. Brandt and J. Williamson, *The 1054 supernova and native American rock art*, vol. 10. Journal for the History of Astronomy, Archaeoastronomy Supplement, 1979.
- [3] A. Lyne and H. Tong, "CRABTIME - Crab Pulsar Timing." [Online]. Available: <https://heasarc.gsfc.nasa.gov/W3Browse/all/crabtime.html>
- [4] C.-M. Zhang *et al.*, "Evolution of Spin Period and Magnetic Field of the Crab Pulsar: Decay of the Braking Index by the Particle Wind Flow Torque," 2022, doi: [10.48550/ARXIV.2212.04674](https://arxiv.org/abs/2212.04674).
- [5] I. Malov, "On the second derivatives of the spin periods and braking indices in radio pulsars," *Monthly Notices of the Royal Astronomical Society*, vol. 468, no. 3, pp. 2713–2718, 2017, doi: [10.1093/mnras/stx619](https://doi.org/10.1093/mnras/stx619).
- [6] H. Yang and R. A. Chevalier, "Evolution of the Crab nebula in a low energy supernova," 2015, doi: [10.48550/ARXIV.1505.03211](https://arxiv.org/abs/1505.03211).
- [7] F. F. Kou and H. Tong, "Rotational evolution of the Crab pulsar in the wind braking model," *Monthly Notices of the Royal Astronomical Society*, vol. 450, no. 2, pp. 1990–1998, 2015, doi: [10.1093/mnras/stv734](https://doi.org/10.1093/mnras/stv734).
- [8] R. L. Nugent, "New Measurements of the Expansion of the Crab Nebula," *Publications of the Astronomical Society of the Pacific*, vol. 110, no. 749, pp. 831–836, 1998, doi: [10.1086/316199](https://doi.org/10.1086/316199).
- [9] M. F. Bietenholz and R. L. Nugent, "New expansion rate measurements of the Crab nebula in radio and optical," *Monthly Notices of the Royal Astronomical Society*, vol. 454, no. 3, pp. 2416–2422, 2015, doi: [10.1093/mnras/stv2112](https://doi.org/10.1093/mnras/stv2112).



# The Morganton Scientific

North Carolina  
School of Science and  
Mathematics

Journal of Student STEM Research

Published Jun 27, 2024

Correspondence to  
Chisom Duru  
[duru24c@ncssm.edu](mailto:duru24c@ncssm.edu)

Open Access 

Copyright © 2024 Duru. This is an open-access article distributed under the terms of the [Creative Commons Attribution 4.0 International license](#), which enables reusers to distribute, remix, adapt, and build upon the material in any medium or format, so long as attribution is given to the creator.

## Using Bromelain Application to Inhibit the Spread of the Tobacco Mosaic Virus and Promote Tissue Regeneration in Red Bell Pepper Plants

Chisom Duru<sup>1</sup> 

<sup>1</sup>North Carolina School of Science and Mathematics 

### Abstract

Plant viruses are a prevalent issue as they pose detrimental effects on agriculture, the food economy, and numerous individuals worldwide. One major effect of these viruses is tissue necrosis (breakdown of tissue), which plays a significant role in the decrease of crop yields. This study focused on the Tobacco Mosaic Virus (TMV), which infects over 350 plant species, causes necrotic symptoms, and exhibits a high transmission rate. Presently, various pesticides are in use that cause health issues in humans and are ineffective as some plants exhibit resistance. Moreover, this research aims to inhibit the spread of TMV in red bell pepper plants and promote tissue regeneration using an enzymatic approach since some enzymes have defense capabilities. A protease derived from pineapple, bromelain, was implemented due to its antimicrobial and anti-inflammatory properties. Bromelain was introduced to the plants as a pre-treatment before infection of TMV to analyze potential antiviral effects. Additionally, bromelain appeared to have correlations with a defensive enzyme located within plants known as phenylalanine ammonia lyase (PAL), which initiates the production of secondary metabolites. Using ImageJ software, the amount of plant tissue damage was highlighted and calculated, and a PAL assay was later conducted in conjunction with UV-Vis Spectroscopy to determine the level of PAL within the infected plants. Based on the experimental results, higher concentrations of bromelain contributed to lower levels of PAL, while lower concentrations of bromelain contributed to higher levels of PAL, indicating that higher treatment concentrations produced more antiviral activity.

**Keywords** Bromelain, PAL, Bell pepper plants

### 1. INTRODUCTION

Tissue necrosis is a common result of most diseases and occurs in numerous living organisms during or after disease introduction. Particular diseases that cause tissue damage are viral infections which overtake an organism and replicate within the host, weakening defense mechanisms and promoting conditions detrimental to overall health. A major field that experiences these negative effects is agriculture, suffering losses of approximately 30 billion dollars each year globally due to plant viruses [1] which are also responsible for about half of crop losses [2]. Additionally, plant viruses are connected to the issue of starvation in various areas of the world as they lead to lower crop yields and poorer quality of the crops produced [3]. The Tobacco Mosaic Virus (TMV) was first discovered in the late 1800s and is known to infect over 350 plant species [4]. The ability of this virus to remain active even when the plant tissue dies creates a major issue as this causes higher rates of transmission and increased levels of crop loss. In response, a variety of pesticides are constantly in use, which have been known to cause gastrointestinal, respiratory, carcinogenic, and other health issues in humans and harm from an environmental standpoint [5]. With such issues, identifying a safe, effective, and efficient way to reduce viral diseases and alleviate symptoms of tissue necrosis in plants is crucial. A possible direction is the application of enzymes to enhance defense systems within a plant during infection, which can lower the effect of disease through various counteractions [6]. The ability of enzymes to catalyze chemical reactions is necessary for most life processes, and in a situation of tissue damage due to disease, enhancing enzyme activity to optimal levels is essential for proper recovery [7].

Moreover, this research investigates the ability of bromelain, a protease derived from pineapple, to inhibit TMV within red bell pepper plants. Bromelain is currently used as a dietary supplement and anti-inflammatory treatment for humans, however, it possesses numerous antimicrobial properties that have been primarily studied against bacteria and fungi, but rarely viruses [8]. This study aims to identify the efficacy of bromelain as a pre-treatment to combat TMV and exhibit antiviral activity within the infected plants. Furthermore, this research could reveal the antiviral capacities of bromelain, which could be beneficial in enhancing agricultural practices and serving as a potential method of biocontrol.

A particular enzyme that is being investigated in this research is phenylalanine ammonia lyase (PAL) because this compound is essential for the initiation of the phenylpropanoid pathway in plants and is responsible for the production of secondary metabolites such as lignin and phytoalexin during plant infection [9]. A major focus of this study is to identify the relationship between bromelain and the compound PAL to observe how bromelain affects PAL activity in plants during infection with TMV. Additionally, when defense-related enzymes are activated early on in plant-defense pathways, the prevention of microbial accumulations is likely [10]. Therefore, using a pre-treatment is an effective approach as plants tend to acquire disease later on, and increasing defense prior to infection is essential [6]. To test the efficacy of the bromelain pre-treatment, varying concentrations of bromelain are used to ensure which is the most optimal in producing antiviral effects. Based on the antiviral, antimicrobial, anti-inflammatory, and protease properties of bromelain, the plants will exhibit antiviral activity, and tissue will be preserved when red bell pepper plants infected with TMV are pre-treated with bromelain.

## 2. MATERIALS AND METHODS

**Seed Planting and Germination Process** Before being pre-treated with bromelain, red bell pepper plants were grown using a Jiffy Seed Starting Greenhouse kit which contains peat pellets for seed germination **Figure 1**. To initiate the germination process, the pellets were watered with about 35 mL of water and left to rise before seed planting. In total, 24 peat pellets were used with 3 seeds in each pellet, resulting in 72 red bell pepper plants. These pellets were watered with approximately 10 mL of water as needed over two weeks.

### 2.1. Preliminary Bromelain Treatment

To test the effects of bromelain on red bell pepper plants before infection, a preliminary treatment was conducted in which two plants from the sample size were treated with different concentrations of bromelain. The first plant received 110 mg of



**Figure 1.** Beginning stages of plants in Jiffy Seed Starting kit

bromelain in a 20 mL solution of water and the second plant received 140 mg of bromelain in a 20 mL solution of water. Each concentration was administered using spray bottles and the plants were consistently watered and received adequate sunlight.

### 2.2. Transplanting and Plant Upkeep

After reaching adequate size, the plants were transplanted into smaller pots containing garden soil; Each plant received approximately 20-100 mL of water over a span of 7 weeks as needed and a sufficient amount of sunlight per day.

### 2.3. Bromelain Pre-Treatment Application

For preparation of the pre-treatment, approximately 40 mg, 80 mg, 200 mg, and 340 mg of bromelain were weighed out and placed in respective beakers containing 20 mL of spring water (these concentrations were based on previous studies that tested bromelain against bacteria and fungi). Each solution was then transferred to the corresponding spray bottles, which were swirled to ensure even distribution of the enzyme. Following this, each concentration was sprayed on the corresponding group of plants.

### 2.4. Inoculation

After two days, all the pre-treated plants were infected with TMV. To inoculate the plant leaves with TMV, a foam applicator was dipped in a vial of diatomaceous earth (abrasive) and dabbed on the leaf epidermis with support under the leaf using a paper towel pad **Figure 2**. The virus was then painted over the surface of the leaf with another foam applicator and left to air-dry before rinsing with sprays of water for about 3 seconds. This process was repeated for 4 leaves on each of the 22 red bell pepper plants, including a control group that did not receive pre-treatment.

### 2.5. Microscope Imaging

Infected leaves from the treatment groups and the control group were collected and placed between glass plates for clear imaging. The respective samples were then aligned with the microscope camera for imaging **Figure 3**. Next, the images were uploaded into the Las X microscope software and acquired for further analysis **Figure 4**.

### 2.6. ImageJ Software Analysis



**Figure 2.** Treating the leaves

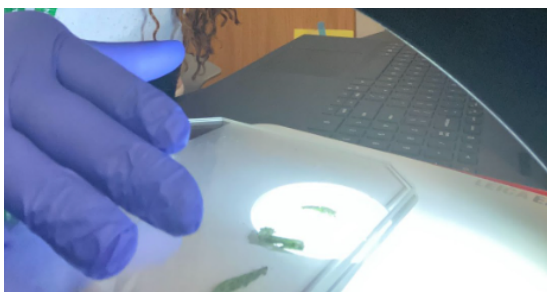


**Figure 4.** Collection of leaf samples

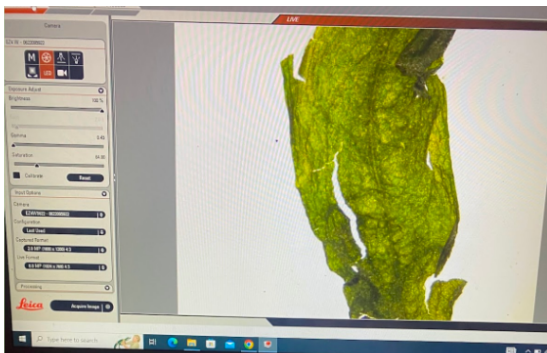


**Figure 4.** Alignment of leaf samples with microscope

To obtain numerical data regarding the amount of leaf damage produced, the software ImageJ was utilized. The images of the damaged leaves were first inputted into the software and were outlined to calculate the total leaf area. The color threshold settings were then changed to adjust the hue, saturation, and brightness levels to highlight the diseased regions of the leaves **Figure 5**. Lastly, the total leaf area and diseased area values were obtained in pixels and used to determine the percent tissue damage.

### 2.7. Phenylalanine Ammonia Lyase (PAL) Assay

The infected plant tissue was collected (approximately 0.03 g) from each treatment group along with the control group and tested to determine PAL concentrations. To begin, each sample was



**Figure 5.** Importing image file into ImageJ Software

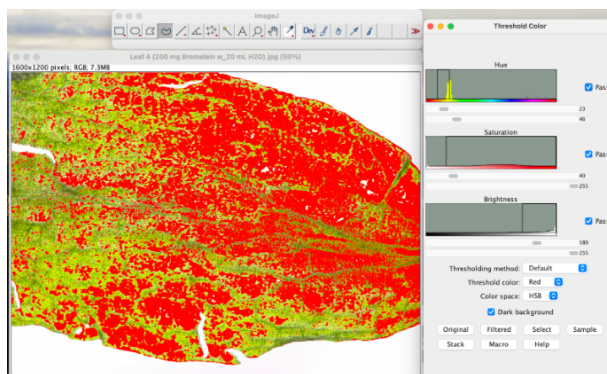


**Figure 6.** Adjustment of color threshold settings (i.e. hue, saturation, and brightness) to highlight tissue damage



**Figure 7.** Transfer of sample cuvette into UV-Vis spectrophotometer

homogenized in an ice water bath and centrifuged for 10 minutes. Next, supernatant was obtained from each tube and placed in new tubes. Appropriate reagents were then added to the samples and the tubes were vortexed.

### 2.8. UV-Visible Spectroscopy

A 1 cm optical path along with a 290 nm wavelength was set for UV-Vis spectroscopy to calculate absorbance values. Using the samples from the PAL assay, 3 mL of each sample was transferred into cuvettes and placed in the spectrophotometer (**Figure 7**). Finally, the concentrations of PAL in the control and treatment samples were calculated.

## 3. RESULTS AND DISCUSSION

### 3.1. Preliminary Bromelain Treatment

Based on the bromelain concentrations administered to the plants (110 mg and 140 mg), it could be understood qualitatively that bromelain had no adverse effects on the plants and seemed to enhance the growing process. The treated plants had a stronger structure and were less flimsy compared to the untreated plants, indicating that bromelain most likely contributes to stronger cell walls within plant cells. In addition, the bromelain-treated plants could go longer periods without water based on increased posture that was observed, highlighting possible capacities of bromelain to promote water retention. It was also observed that the higher concentration of bromelain (140 mg) contributed to healthier outcomes qualitatively compared to the lower concentration (110 mg).

### 3.2. Leaf Damage Calculations

After the ImageJ processing of the infected leaves for the rest of the sample size, the total and diseased area values were obtained in

pixels. Based on the data, higher concentrations of bromelain were associated with greater leaf surface areas, while lower concentrations of bromelain contributed to lower leaf surface areas. The percent tissue damage values amongst the leaves treated with higher bromelain concentrations had larger ranges than those treated with lower bromelain concentrations, highlighting the efficacy of bromelain against TMV in higher dosages. In addition, the average percent damage was higher amongst leaves with greater bromelain concentrations (28.55% for 340 mg & 33.26% for 200 mg) and lower amongst leaves with smaller bromelain concentrations (19.11% for 80 mg & 8.46% for 40 mg), which could be attributed to uncontrolled conditions such as the varying surface areas, the amount of sunlight each plant received, the varying sizes of the leaves, and potential errors in outlining the leaves using the ImageJ software.

### 3.3. Phenylalanine Ammonia Lyase (PAL) Assay

Using the absorbance values from the UV-Vis Spectroscopy and the equation provided by the Elabscience PAL Assay Kit, PAL activity was calculated for each treatment group and the control. From the calculation performed, the results were directly correlated with UV-Vis spectroscopy results as there was an inverse relationship between PAL activity and bromelain concentrations; PAL activity was higher in plants treated with lower concentrations of bromelain and lower in plants treated with higher concentrations of bromelain. With this information, it could clearly be understood that bromelain exhibited antiviral activity and was effective as a pre-treatment against TMV in the infected plants, especially with higher dosages.

### 3.4. UV-Vis Spectroscopy

According to the results obtained by UV-Vis spectroscopy, leaves with higher concentrations of bromelain (340 mg and 200 mg) had lower PAL activity compared to leaves treated with lower bromelain concentrations based on the absorbance values.

This most likely occurred because higher bromelain concentrations contribute to increased levels of antiviral activity, decreasing the need for PAL within the plant, while lower bromelain concentrations contribute to antiviral activity on a lower scale, indicating a higher need for PAL activity. Moreover, higher

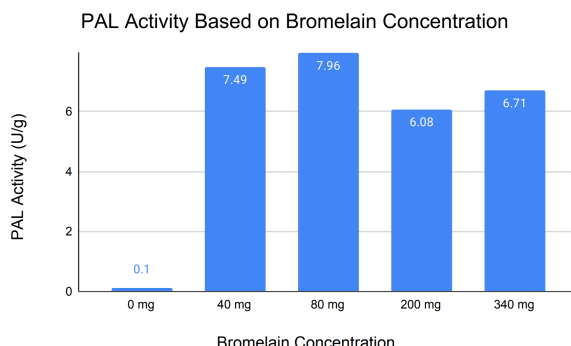


**Figure 8.** Based on the graph, PAL activity was higher in plants treated with lower bromelain concentrations and lower in plants treated with higher bromelain concentrations. This suggests that bromelain in higher dosages contributes to increased antiviral activity as PAL enzyme activity is not as high, while lower dosages contribute to antiviral activity on a lower scale. With little to no PAL activity in the control, bromelain overall appeared to have antiviral effects.

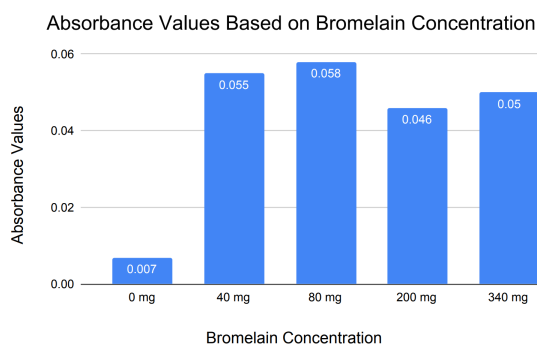


**Figure 9.** From the UV-Vis results, absorbance values were higher in plants treated with lower bromelain concentrations and lower in plants treated with higher bromelain concentrations. In the control, there was no significant absorbance value, which suggests bromelain's efficacy as an antiviral plant treatment.

concentrations of bromelain appeared to be more optimal in assisting plant defense mechanisms and produced greater antiviral activity as PAL levels were lower.

## 4. LIMITATIONS

In this experiment, there were also uncontrolled circumstances that could have affected the results. To begin, the growing conditions of the pepper plants posed variations in the leaf sizes as some plants were closer to sunlight than others, which could have affected plant tissue damage calculations. Additionally, when applying the bromelain pre-treatment, it was not ensured that all the solution reached the plants as the liquid also absorbed into the soil and touched external surfaces. Another aspect that impacted this experiment was the lack of repeated trials due to time constraints, which could have affected the conclusiveness of the results.

## 5. CONCLUSION

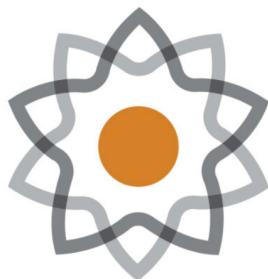
From the data obtained, the use of bromelain as a pre-treatment was effective against TMV as antiviral activity was produced within the infected plants. Moreover, this research highlights the potential of implementing defense enzymes as a mechanism against plant viruses and the capacity of natural substances to combat plant disease effectively with minimal adverse effects. With higher bromelain concentrations, lower PAL values were reflected, which indicated that these concentrations were more optimal as more antiviral activity was exhibited. This was also confirmed with the qualitative data as lower tissue damage was observed in treatment groups with higher bromelain concentrations, and higher tissue damage in treatment groups containing lower bromelain concentrations. Furthermore, this research is groundbreaking in the agricultural field as it could change the perspective of farming and positively impact many individuals worldwide since the use of this enzymatic approach offers newer potential for crop yield and presents a solution to numerous plant diseases.

## ACKNOWLEDGMENTS

I would like to thank Mrs. Jennifer Williams for assisting me with my project idea and being a supportive research mentor. I would also like to extend my gratitude to the Research in Biology program and Summer Research and Innovation program at the North Carolina School of Science and Mathematics-Morganton for offering me this opportunity and facilitating my research.

## REFERENCES

- [1] C. M. Fraser and C. Chapple, "The Phenylpropanoid Pathway in *Arabidopsis*," *The Arabidopsis Book*, vol. 9, p. e152, 2011, doi: [10.1199/tab.0152](https://doi.org/10.1199/tab.0152).
- [2] J. Hilaire *et al.*, "Risk perception associated with an emerging agri-food risk in Europe: plant viruses in agriculture," *Agriculture & Food Security*, vol. 11, no. 1, 2022, doi: [10.1186/s40066-022-00366-5](https://doi.org/10.1186/s40066-022-00366-5).
- [3] R. A. C. Jones, "Global Plant Virus Disease Pandemics and Epidemics," *Plants*, vol. 10, no. 2, p. 233–234, 2021, doi: [10.3390/plants10020233](https://doi.org/10.3390/plants10020233).
- [4] J. Mamo, "Antibacterial and Anticancer Property of Bromelain: A Plant Protease Enzyme from Pineapples (*Ananas comosus*)," *Current Trends in Biomedical Engineering & Biosciences*, vol. 19, no. 2, 2019, doi: [10.19080/ctbeb.2019.19.556009](https://doi.org/10.19080/ctbeb.2019.19.556009).
- [5] P. Nicolopoulou-Stamati, S. Maipas, C. Kotampasi, P. Stamatis, and L. Hens, "Chemical Pesticides and Human Health: The Urgent Need for a New Concept in Agriculture," *Frontiers in Public Health*, vol. 4, 2016, doi: [10.3389/fpubh.2016.00148](https://doi.org/10.3389/fpubh.2016.00148).
- [6] K. Prasannath, "Plant defense-related enzymes against pathogens: a review," *AGRIEAST: Journal of Agricultural Sciences*, vol. 11, no. 1, p. 38–39, 2017, doi: [10.4038/agrieast.v11i1.33](https://doi.org/10.4038/agrieast.v11i1.33).
- [7] T. Anand, A. Chandrasekaran, S. Kuttalam, T. Raguchander, V. Prakasam, and R. Samiyappan, "Association of some plant defense enzyme activities with systemic resistance to early leaf blight and leaf spot induced in tomato plants by azoxystrobin and *Pseudomonas fluorescens*," *Journal of Plant Interactions*, vol. 2, no. 4, pp. 233–244, 2007, doi: [10.1080/17429140701708985](https://doi.org/10.1080/17429140701708985).
- [8] B. López-García, M. Hernández, and B. Segundo, "Bromelain, a cysteine protease from pineapple (*Ananas comosus*) stem, is an inhibitor of fungal plant pathogens: Antifungal bromelain for crop protection," *Letters in Applied Microbiology*, vol. 55, no. 1, pp. 62–67, 2012, doi: [10.1111/j.1472-765x.2012.03258.x](https://doi.org/10.1111/j.1472-765x.2012.03258.x).
- [9] N. Dong and H. Lin, "Contribution of phenylpropanoid metabolism to plant development and plant–environment interactions," *Journal of Integrative Plant Biology*, vol. 63, no. 1, pp. 180–209, 2021, doi: [10.1111/jipb.13054](https://doi.org/10.1111/jipb.13054).
- [10] J. N. Thakker, S. Patel, and P. C. Dhandhukia, "Induction of Defense-Related Enzymes in Banana Plants: Effect of Live and Dead Pathogenic Strain of *Fusarium oxysporum* f. sp. *cubense*," *ISRN Biotechnology*, vol. 2013, pp. 1–6, 2013, doi: [10.5402/2013/601303](https://doi.org/10.5402/2013/601303).



# A Novel Approach to Inhibit MAP2K1 Overexpression Present in Melorheostosis Utilizing *Moringa oleifera* Extracts

Ashmith Gududuru<sup>1</sup> 

<sup>1</sup>North Carolina School of Science and Mathematics 

## The Morganton Scientific

North Carolina  
School of Science and  
Mathematics

Journal of Student STEM Research

### Abstract

Melorheostosis is a rare bone disorder characterized by a mutation in the MAP2K1 gene in the MAPK signaling pathways, overproducing MEK1 protein, resulting in abnormal, flowing bone growth. Treatment and diagnosis options are limited; therefore, this experiment explores the use of *Moringa oleifera*, a promising natural product, as a potential treatment option for melorheostosis. In this experiment *M. oleifera* seed and leaf extract was fed to *Drosophila melanogaster* and DSOR1 protein (an ortholog of the MEK1 protein) was extracted from samples and examined through a western blot. However, experimental results were inconclusive due to technical issues in the western blotting process. This paper serves as a novel method to study MEK1 protein expression in humans through the use of *D. melanogaster* and natural product chemistry. Future research possibilities include rerunning the western blot and optimizing the conditions, testing the synergistic effects of leaf and seed extracts, and investigating moringin (an isothiocyanate found in *M. oleifera* leaves).

**Keywords** Melorheostosis, *Moringa oleifera*, MEK1 inhibition

### 1. INTRODUCTION

Being derived from the Greek words “melos,” which means limbs, “rheos,” which means to flow, and “ostosis,” which relates to bone formation, melorheostosis often results in a “flowing” pattern of excess bone growth along any body part. This is often compared to candle wax melting off of a candlestick, which gives this condition the nickname “dripping candle wax disease.” Melorheostosis is a rare and relatively unexplored bone disorder characterized by irregular and asymmetrical bone growth atop the long bones of a patient’s upper and lower limbs. Symptoms stemming from abnormal bone development include joint pain, stiffness, soft tissue fibrosis, and lesions [1]. Furthermore, with merely 300 reported cases worldwide leading up to 2015, the diagnosis and treatment options haven’t been thoroughly researched and understood [2].

Published Jun 27, 2024

**Correspondence to**  
Ashmith Gududuru  
[gududuru24a@ncssm.edu](mailto:gududuru24a@ncssm.edu)

**Open Access** 

Copyright © 2024 Gududuru. This is an open-access article distributed under the terms of the Creative Commons Attribution 4.0 International license, which enables reusers to distribute, remix, adapt, and build upon the material in any medium or format, so long as attribution is given to the creator.

However, recent research has proposed a potential answer for the previously unknown cause of melorheostosis. From biopsies taken from 15 melorheostosis patients, 8 exhibited a mutation in the MAP2K1 gene [3]. MAP2K1 encodes proteins that are part of the RAS/MAPK signaling pathway. Further research showed that a somatic mutation of the MAP2K1 oncogene causes the overproduction of the specific MEK1 protein, which affects human bone formation. The enhanced MEK1 activity surrounding abnormal mutations supports MAP2K1’s involvement in melorheostosis. Since MAP2K1 and MEK1 are part of a signaling pathway associated with cellular proliferation, a somatic mutation causes an excess quantity of the MEK1 protein. This then results in excess cellular proliferation. This cellular proliferation takes the form of excess candle wax-like growth.

Even though researchers have potentially found a cause, treatment options are severely limited, with surgery being one of the only options for many [4]. Apart from surgery, synthetic drugs are in development that try to combat melorheostosis, but their long-term efficacy is questionable and currently untested. By branching out into the field of natural product chemistry, a concrete treatment option can be derived. Natural product drugs have an advantage over synthetic drugs by containing

bioactive compounds that can attack many biological targets. They also are correlated with decreased preclinical toxicity [5]. With the advantages of natural product chemistry, it is evident that it can be a viable melorheostosis treatment option.

A significant challenge is finding the right natural product to combat the rapid cell proliferation associated with a MAP2K1 mutation in melorheostosis. For thousands of years, a medicinal plant from South Asia has been used as a natural drug for various medical conditions and can be used to combat melorheostosis. *Moringa oleifera* is a fast-growing, deciduous tree primarily grown in India and Bangladesh and has been a staple of regional medicine since the Roman Empire. The roots, leaves, and bark are all utilized to create pastes, powders, and concoctions to treat conditions such as malaria, arthritis, skin lesions, and diabetes [6]. Due to its medicinal benefits, it has nicknames such as the “miracle tree” and “mother’s best friend.” Similar to other plants, *Moringa oleifera* is full of bioactive compounds such as flavonoids and phenolic compounds. However, with it only growing in hot climates, *Moringa oleifera*’s medicinal potential hasn’t been recognized worldwide.

Yet in recent years, researchers have been testing the various properties of the plant to see its effective bioactive compounds regarding diabetes, cancer, and other major diseases. Studies have also shown a significant difference in the medicinal properties of extracts from different parts of the plant. Leaves tend to have better antimicrobial and antidiabetic properties, while roots have better antioxidant properties [7]. Not only does *Moringa oleifera* contain antioxidant, antidiabetic, and antimicrobial compounds, but it has also shown promising inhibitory properties concerning cancer. There are now ten known compounds that have the potential for anticancer substances. These compounds induced cell cycle arrest and apoptosis, which are useful for suppressing mutations and excess cell proliferation [8]. This leads to the question of whether *Moringa oleifera* could be useful in inhibiting the gene expression and production of MEK1 to stop the excess bone growth associated with melorheostosis. The purpose of this research is to effectively extract bioactive compounds from *Moringa oleifera* leaves and seeds to test their inhibitory effects on the MAP2K1 oncogene and the MEK1 protein in *Drosophila melanogaster* (fruit fly) to justify its use in melorheostosis treatment. A fruit fly model is used due to the fact that they contain the DSOR1 gene, which produces MEK1 protein within fruit fly tissue. Since DSOR1 is an ortholog for the MAP2K1 gene, inhibiting expression in fruit flies will be an accurate model for inhibiting MAP2K1 expression in humans.

## 2. METHODS

### 2.1. Collection of Leaf and Seed Samples

*Moringa* leaves were collected in Mecklenburg County, North Carolina. The samples were collected from a potted, young *M. oleifera* plant on 3 different dates. The first sample was collected on August 12, 2023, the second was collected on September 3, 2023, and the third sample was collected on September 9, 2023. Each sample contained 50g of leaves cut with scissors and placed in a sterile plastic bag. Each sample was frozen overnight, and transported to Burke County, North Carolina in an insulated container with a temperature of 0°C. At the lab, leaves were stored in a freezer at

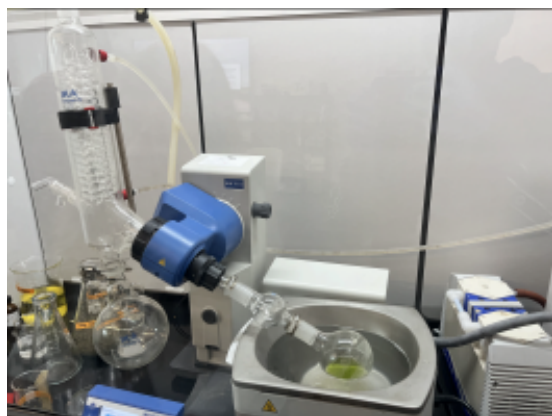


**Figure 1.** Preparation of Crude Leaf Extract Using Rotary Evaporator

-18°C. Seeds had been collected in Mexico and were ordered from Yerbero. Seed samples were ordered on June 15, 2023, and were stored at room temperature until usage.

### 2.2. Preparation of Leaf Extract

Leaves were frozen at least 24 hours before the procedure. Using an oven, the leaves were heated at 50°C for 2 hours and left to dry overnight at room temperature. 20g of dried leaves were crushed using a coffee grinder until they became a fine powder. This fine powder was then extracted at room temperature utilizing a sequence of three solvents in increasing polarity: hexane, methanol, and water. 200 mL of each solvent was used, and each solvent was extracted for 2 and a half hours. After each solvent was extracted for this interval, they were each filtered and evaporated in vacuo. 0.7g of crude extract was gained. The experiment was repeated 2 times to obtain a total of 2.1g of evaporated leaf extract. This mass was then dissolved in 50 mL of bottled spring water.

### 2.3. Preparation of Seed Extract

Using an oven, the seeds were heated at 50°C for 3 hours and continued to dry overnight at room temperature. Wings and shells were removed from the seeds and discarded. 20g of dried seeds were crushed into a fine powder with a coffee grinder and extracted in 1 L of hexane overnight. Hexane extract was filtered and evaporated in vacuo. The extract was transferred into 50 mL of water for 48 hours and evaporated in vacuo after the 48-hour interval. Approximately 0.8g of crude seed extract was collected. The experiment was repeated 2 times to obtain 2.4g of extract. This mass was mixed into 50 mL of bottled spring water.

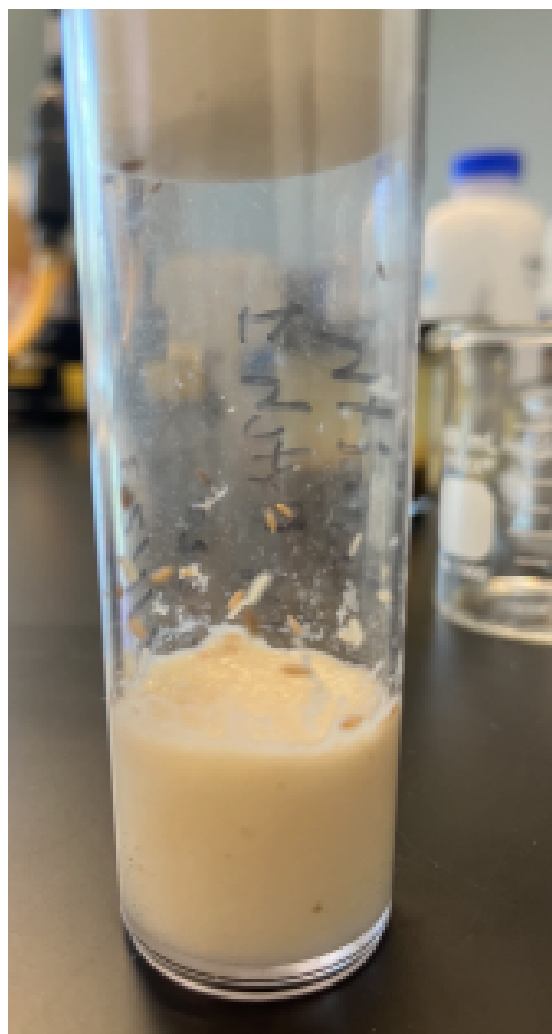
### 2.4. Drosophila Melangogaster Experimental Group Preparation

*D. melanogaster* stocks were ordered from the Indiana Bloomington Drosophila Stock Center in September 2023. The flies used in this experiment were mutated after exposure to ethyl methanesulfonate by Bloomington before shipping. After the flies were transported to Burke County, NC, they were left to breed for 2 months. After each life cycle of a vial of fruit flies (containing ~20 fruit flies), larvae were transferred to a new labeled vial so they could lay new eggs. After the breeding period, flies were separated into 21 vials (1 for each experimental and control group), with ~12 flies per vial. Aqueous seed and leaf extracts were mixed into fly food at different concentrations depending on the treatment groups.

Extracts (3 vials of each)	Concentration
Control	0 mg/mL
Leaf Extract	2 mg/mL
Leaf Extract	5 mg/mL
Leaf Extract	10 mg/mL
Seed Extract	2 mg/mL
Seed Extract	5 mg/mL
Seed Extract	10 mg/mL

**Table 1.** *D. melanogaster Experimental and Control Groups*

After the flies had fed on their food either containing or lacking extract for a period of 3 weeks, they were sacrificed to collect tissue. Fly heads were cut off due to the high concentration of DSOR1 in the body. If the heads were included, the possibility to overload an assay increases as there is too much protein in 1 sample. DSOR1 was extracted from fly tissue through a process of heating the tissue mixed into RIPA buffer at 90°C and extracting the supernatant from the heated microcentrifuge tubes. A total of 16 protein samples were collected.

**Figure 2.** *Fruit Fly Sample*

Leaf Samples	Seed Samples
Control 1	Control 1
Control 2	Control 2
2 mg/mL	2 mg/mL
2 mg/mL	2 mg/mL
5 mg/mL	5 mg/mL
5 mg/mL	5 mg/mL
10 mg/mL	10 mg/mL
10 mg/mL	10 mg/mL

**Table 2.** *Protein Samples Collected From Fly Experimental and Control Groups*

Leaf Samples	Protein Concentration (mg/mL)	Seed Samples	Protein Concentration (mg/mL)
Control 1	21.103	Control 1	29.712
Control 2	31.376	Control 2	35.04
2 mg/mL	27.034	2 mg/mL	31.724
2 mg/mL	33.66	2 mg/mL	23.211
5 mg/mL	23.846	5 mg/mL	32.728
5 mg/mL	29.838	5 mg/mL	29.087
10 mg/mL	32.763	10 mg/mL	32.539
10 mg/mL	34.381	10 mg/mL	35.873

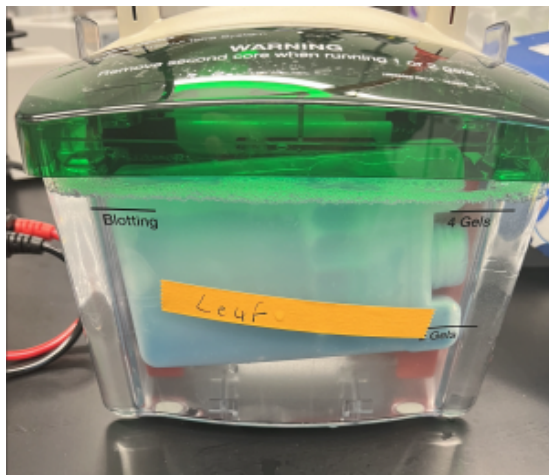
**Table 3.** *Nanodrop Protein Concentrations*

The Nanodrop protein concentrations fluctuate randomly due to the fact that this is the quantification for all protein inside of the flies, not just the target protein. To isolate the target protein, a western blot was run. The first step is to run a gel electrophoresis using a Bio-Rad protein gel instead of a DNA gel. This protein gel will capture the proteins in the membrane to create bands, similar to a DNA gel electrophoresis. The main difference is that proteins are captured on the gel to create bands instead of DNA. The leaf and seed samples are run on different gels with one devoted to just the leaf extract and one for the seed extract. A protein standard was used to create a reference for any other bands that may appear on the gel. The last lane is left empty to determine whether the gel is contaminated or sterile. A Tetra-Cell is used to run the gel electrophoresis and western blot.

After the gel has run, a blotting sandwich created with blotting paper, filter pads, a nitrocellulose membrane paper, and the gel is placed inside of the Tetra-Cell to transfer the protein bands from the gel to the nitrocellulose paper so that antibodies can be added at a later step.

After the protein bands have transferred from the gel to the nitrocellulose paper, antibodies are added to the paper and rocked. The membrane was incubated with 7 ml of blocking buffer for 45 minutes on a rocking platform. Blocking buffer was discarded and 7mL of primary antibody was added to the rocking platform and left to incubate for 1 hour. 7 ml of wash buffer was added to the membrane for 3 minutes on a rocking platform. The washing

Lane	Sample
Lane 1	Protein Standard
Lane 2	Control 1
Lane 3	Control 2
Lane 4	2 mg/mL
Lane 5	2 mg/mL (duplicate)
Lane 6	5 mg/mL
Lane 7	5 mg/mL (duplicate)
Lane 8	10 mg/mL
Lane 9	10 mg/mL (duplicate)
Lane 10	Empty

**Table 4.** Description of Lanes on a Protein Gel for both Leaf and Seed Samples**Figure 3.** Image of Tetra Cell

process was repeated two more times. The membrane was then incubated with 7 ml of secondary antibody for 1 hour. The membrane was rinsed in 7 ml of wash buffer 3 times for 3 minutes each. Wash buffer was discarded and 7 ml of HRP color detection reagent was added to the rocking platform to incubate for 10–30 minutes. The membrane was rinsed twice with distilled water and blotted dry with a paper towel. Finally, the paper was left to air dry for 30 minutes and then covered in plastic wrap. This process was done twice: once for the leaf gel and once for the seed gel.

### 3. RESULTS

After running the western blots, the two air dried membrane papers were observed to determine the effects of *M. oleifera* on DSOR1 protein expression. However, the results were inconclusive as the blots did not show enough color to see any bands apart from the protein standard.

Looking at these two sheets, it is evident that the transfer process did not complete properly, leaving both sheets blank as they lack any bands of protein and only a faint ladder. For comparison, the image below shows the difference between the thickness and opacity of the bands on a nitrocellulose paper that had received the protein bands transferred properly compared to the leaf extract.

**Figure 4.** Leaf Sample Nitrocellulose Paper**Figure 5.** Seed Sample Nitrocellulose Paper

It is clear that on a gel that was run properly, the bands have different colors, clear borders, and are easily visible and distinguishable. This likely means that the western blot did not run properly, and the effects of the treatment are not known.

### 4. DISCUSSION

Building on the results above and interpreting the factors that may have influenced the western blot, some possible reasons for why the blot malfunctioned could be determined. A likely issue could be the power supply for the Tetra-Cell that the Western Blot is run in. In the laboratory where the Western blot was performed, power is supplied to the Tetra-Cell through a surge protector that is connected to the wall. However, the surge protector lacks the ability to conduct enough voltage to properly power the Tetra-Cell. This causes the runtime of the blot to increase to account for the lower voltage. This affects how well the gel transfers to the nitrocellulose paper as low voltages or runtimes causes less of the paper to transfer.

The greatest possibility for error is in regards to the application of antibodies to the nitrocellulose paper after the Tetra-Cell was run. If too little antibody was poured onto the paper, there would not have been enough to bind to the target protein. Still, even if the antibody had bound to the protein, it wouldn't be visible if the colorimetric agent did not visualize the bands on the paper. Horseradish Peroxidase (HRP) was used in this experiment to bind to the primary and secondary antibodies, however, if the amount of HRP is too small, it will not be able to produce color on the paper because there isn't enough to bind to the protein and create clear bands. This would mean that the antibodies could have bound to the target

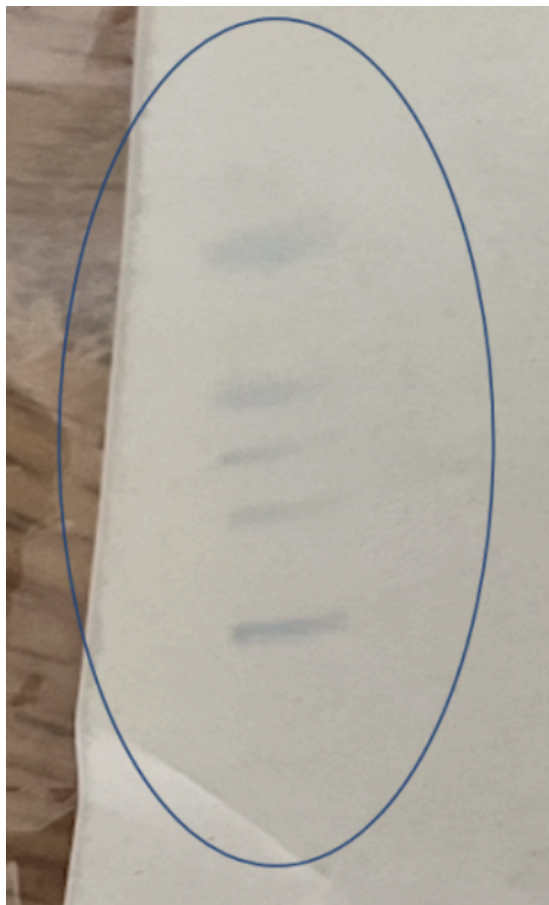


**Figure 7.** Protein Bands on Leaf Sample

protein, but there is no visual information that justifies this theory, so the results are inconclusive.

Since the western blot was the issue, this also means that the effects of the treatment are unknown. Due to the fact that the Nanodrop quantifies the total amount of protein in each sample and not the target protein, the effects of seed and leaf extract cannot be identified because the target protein was not measured. If the experiment was to be repeated and the specific bands of protein were to appear on the western blot, ImageJ (a computer program to analyze an image of the western blot) could be used to quantify the amount of protein between samples and determine whether *M. oleifera* is a viable inhibitor of DSOR1 in fruit flies.

While the experiment had multiple issues, its successful aspects should be acknowledged as well. Due to the minimal amount of research dedicated to melorheostosis in humans and in medical models, the experimental methods described in this paper have not been performed before regarding the quantification of MEK1 protein in humans or DSOR1 proteins in fruit flies. This paper can be used as a proof of concept of how extracts can be taken from *M. oleifera* and used on *D. melanogaster* to inhibit protein expression. The nanodrop concentrations illustrate that *M. oleifera* can be exposed to fruit flies and proteins can be extracted from fruit flies with the methods described in this paper. The faint bands on the completed western blot cannot be used to definitively establish a link between the treatment groups and protein expression, but show that a minimal amount of protein was transferred through the gel. Under different

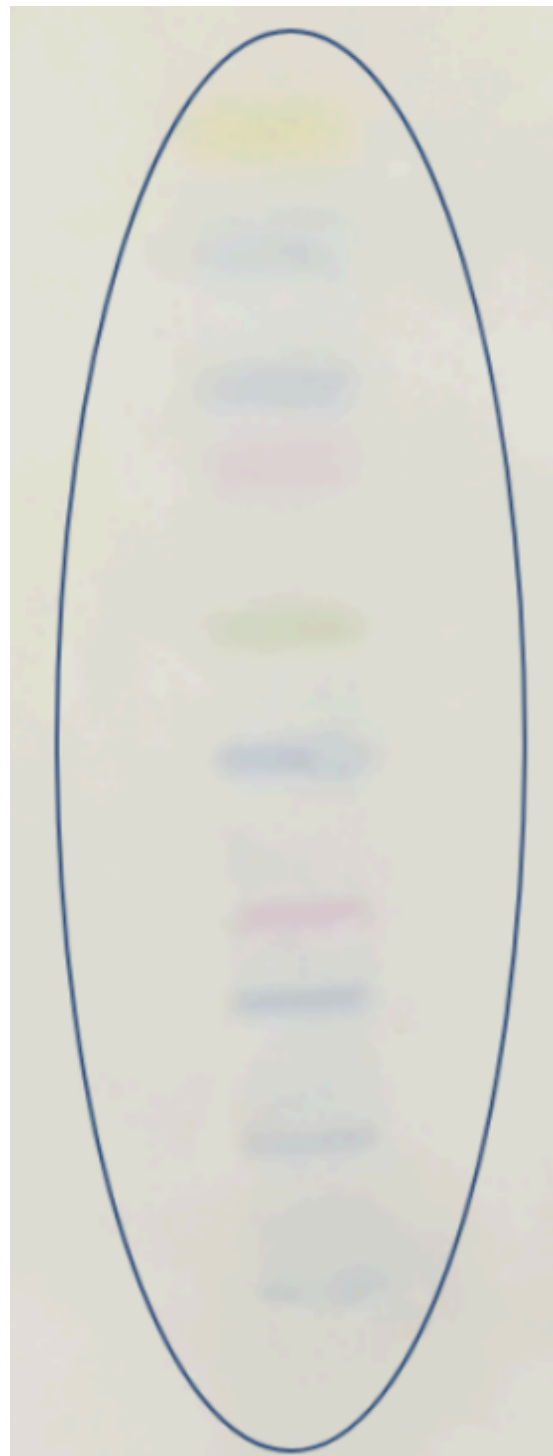


**Figure 7.** Protein Bands on Nitrocellulose Paper that Ran Properly

conditions, this experiment could be replicated to produce results that can be analyzed.

## 5. CONCLUSION

Although the results of the western blot were inconclusive, the data gathered throughout the experiment is enough to draw conclusions and predict the efficacy of *M. oleifera* as a treatment for melorheostosis. On the positive side, proteins were able to be

extracted from the fruit flies. This is shown by the Nanodrop protein quantification, which shows the total amount of protein in each sample. This means that the western blot itself was the confounding factor, as the process of breeding, feeding, and sacrificing fruit flies yielded enough protein to be quantified on a western blot. Utilizing another set of samples and the remaining tissue would allow the experiment to be repeated to possibly gain results.

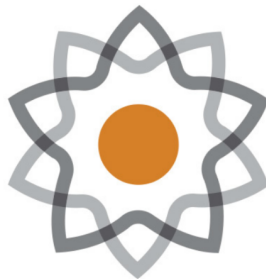
After examining the possible errors that could have contributed to the inconclusive results, it is evident that much more future work should be done to answer the research question posed at the beginning of this experiment. Firstly, the western blot should be rerun with the proper conditions to accommodate the Tetra-Cell and the proper amount of antibody. Instead of using HRP as a colorimetric agent, fluorescence and a plate reader should be used to quantify the amount of protein on the nitrocellulose paper. This is beneficial for multiple reasons: a fluorescent agent will not deal with color that is visible to humans, which reduces the chance for a researcher to mistake the thickness and color of the bands due to bias. Using a plate reader to quantify the results will also be more accurate than a computer software analyzing an image because the photo quality, lighting of the picture, and angle could all be variables that affect the quantification of protein on ImageJ.

Beyond rerunning the experiment and fixing mistakes, in order to dive deeper into the potential of *M. oleifera*, running western blots with different experimental groups that change the concentration of extract and blots that change the samples in each lane will help determine whether leaf extract or seed extract is a better option. Furthermore, using these results, another extract could be created that combines the leaves and the seeds so that the synergistic effects can be tested against the extracts that are separate. Branching off from crude extracts, utilizing an isothiocyanate known as moringin to create an extract might be another possible solution. Moringin is located within the leaves and seeds of *M. oleifera*, and has been used in cancer research to test its inhibitory capabilities. With the inhibitory effects of isothiocyanates being a relatively new field of research, the use of moringin as an inhibitor for protein production and cell growth can prove to be useful, as a connection between inhibitory isothiocyanates and MAPK pathways has already been established in previous studies. Further than justifying the use of *M. oleifera* as a potential treatment option for melorheostosis, this future research can justify the use of isothiocyanates as an avenue for natural product drug development.

The author would like to thank the NCSSM Research in Biology Program, Mrs. Jennifer Williams, and Dr. Mareca Lodge.

## REFERENCES

- [1] C. N. Fick *et al.*, "Melorheostosis: A Clinical, Pathologic, and Radiologic Case Series," *American Journal of Surgical Pathology*, vol. 43, no. 11, pp. 1554–1559, 2019, doi: [10.1097/pas.0000000000001310](https://doi.org/10.1097/pas.0000000000001310).
- [2] V. Vyskocil, K. Koudela, T. Pavelka, K. Stajdlova, and D. Suchy, "Incidentally diagnosed melorheostosis of upper limb: case report," *BMC Musculoskeletal Disorders*, vol. 16, no. 1, 2015, doi: [10.1186/s12891-015-0455-z](https://doi.org/10.1186/s12891-015-0455-z).
- [3] H. Kang *et al.*, "Somatic activating mutations in MAP2K1 cause melorheostosis," *Nature Communications*, vol. 9, no. 1, 2018, doi: [10.1038/s41467-018-03720-z](https://doi.org/10.1038/s41467-018-03720-z).
- [4] S. Chou, C. Chen, J. Chen, S. Chien, and Y. Cheng, "Surgical treatment of melorheostosis: Report of two cases," *The Kaohsiung Journal of Medical Sciences*, vol. 28, no. 5, pp. 285–288, 2012, doi: [10.1016/j.kjms.2011.11.009](https://doi.org/10.1016/j.kjms.2011.11.009).
- [5] C. F. Stratton, D. J. Newman, and D. S. Tan, "Cheminformatic comparison of approved drugs from natural product versus synthetic origins," *Bioorganic & Medicinal Chemistry Letters*, vol. 25, no. 21, pp. 4802–4807, 2015, doi: [10.1016/j.bmcl.2015.07.014](https://doi.org/10.1016/j.bmcl.2015.07.014).
- [6] A. Chi'textcommabelow s *et al.*, "Bioactive Compounds in *Moringa oleifera*: Mechanisms of Action, Focus on Their Anti-Inflammatory Properties," *Plants*, vol. 13, no. 1, p. 20–21, 2023, doi: [10.3390/plants13010020](https://doi.org/10.3390/plants13010020).
- [7] T. Tshabalala, A. Ndhlala, B. Ncube, H. Abdelgadir, and J. Van Staden, "Potential substitution of the root with the leaf in the use of *Moringa oleifera* for antimicrobial, antidiabetic and antioxidant properties," *South African Journal of Botany*, vol. 129, pp. 106–112, 2020, doi: [10.1016/j.sajb.2019.01.029](https://doi.org/10.1016/j.sajb.2019.01.029).
- [8] P. Wisitpongpan, N. Suphrom, P. Potup, N. Nuengchamnong, P. C. Calder, and K. Usuwanthim, "In Vitro Bioassay-Guided Identification of Anticancer Properties from *Moringa oleifera* Lam. Leaf against the MDA-MB-231 Cell Line," *Pharmaceuticals*, vol. 13, no. 12, p. 464–465, 2020, doi: [10.3390/ph13120464](https://doi.org/10.3390/ph13120464).



# The Morganton Scientific

North Carolina  
School of Science and  
Mathematics

Journal of Student STEM Research

## Inhibition of TORC1 Pathway in *Saccharomyces cerevisiae* to Induce Autophagy Using Graphene Oxide

Sesha Jonnavithula<sup>1</sup> 

<sup>1</sup>North Carolina School of Science and Mathematics 

### Abstract

Alzheimer's Disease (AD) is a neurodegenerative brain disorder that affects close to six million people in the US alone. The disease is characterized by amyloid beta plaque buildup in the brain which limits proper communication and connection between neurons. Patients with AD were shown to have lower rates of autophagy in neuronal cells. Autophagy is the cellular process by which waste buildup is broken down through lysosomal activity. In mammals, the activated mTORC1 pathway inhibits autophagy in the presence of growth factors and amino acids. To explore the potential of using autophagic activity to break down amyloid beta plaques, *Saccharomyces cerevisiae*, which conserves mTORC1 as TORC1, could be used as a model organism. This project focuses on the inhibitory effectiveness of Graphene Oxide (GO) on the TORC1 pathway in *S. cerevisiae*. Firstly, the cytotoxicity of GO to the *S. cerevisiae* species was tested to ensure GO did not hamper cell proliferation by growing *S. cerevisiae* in a medium which included various concentrations of GO. Then, a fluorescent marker, Rosella, which indicates autophagic activity was used to measure the effects of GO. The *S. cerevisiae* was transformed with the Rosella plasmid to give it fluorescent properties, following which the *S. cerevisiae* was grown in the presence of various GO concentrations. The resultant emissions revealed the relationship between the concentration of GO and the induction of autophagy through inhibition of the TORC1 pathway. By inducing autophagy, GO could prove to be the key to breaking down amyloid beta plaques and treating AD.

**Keywords** Alzheimer's Disease, Autophagy, Amyloid Beta Plaque, mTOR Pathways

### 1. INTRODUCTION

#### 1.1. Alzheimer's Disease

Alzheimer's Disease (AD) is a neurodegenerative brain disorder that is also classified as a chronic form of progressive dementia [1]. In the US alone, there are almost six million people [2] living with AD with an estimated 500,000 new diagnoses per year [2]. The brains of people diagnosed with AD are characterized by amyloid beta protein plaques and tau protein tangle buildups. These protein aggregates can block neurotransmission between neurons which can result in cell death [3]. Over time, patients with AD experience a decrease in brain matter and cognitive function as neurons die off at a rapid rate due to intense plaque buildup in critical areas [3].

With no cure, the global prevalence of AD is growing with an estimated 60% of the annual 10 million new cases of dementia coming from the disease [4]. Furthermore, the causes behind plaque buildup and the direct relationship between beta amyloid plaques and dementia is still unclear. As the WHO recognizes AD and dementia as public health priority, initiatives to understand and cure AD are increasingly vital to human health [4].

#### 1.2. Autophagy, mTOR Pathways, and Amyloid Beta Plaque Decomposition

The mammalian mTOR is a serine/threonine kinase that is present in two complexes, mTORC1 and mTORC2. mTOR stands for mammalian Target Of Rapamycin, referencing a drug which is known to inhibit the pathway [5].

Published Jun 27, 2024

Correspondence to  
Sesha Jonnavithula  
[jonnavithula24s@nccsm.edu](mailto:jonnavithula24s@nccsm.edu)

Open Access   
Copyright © 2024 Jonnavithula. This is an open-access article distributed under the terms of the Creative Commons Attribution 4.0 International license, which enables reusers to distribute, remix, adapt, and build upon the material in any medium or format, so long as attribution is given to the creator.

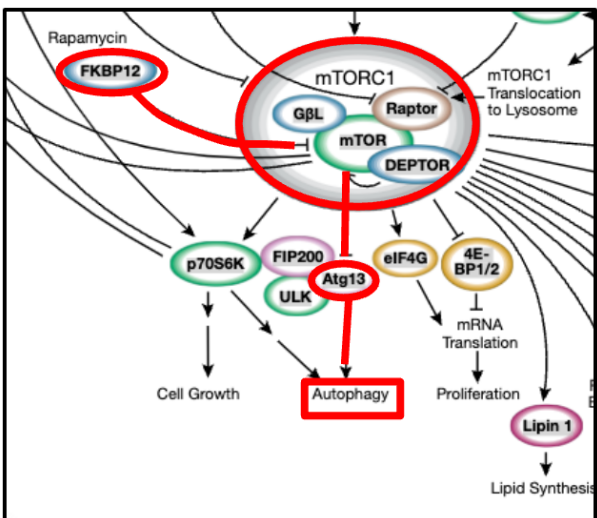


**Figure 1.** The diagram of the mTORC1 pathway showing the activation of autophagy caused by inhibition of the phosphorylated ATG13 in the presence of Rapamycin.

Both mTORC1 and mTORC2 regulate cell proliferation, autophagy and other growth-related processes in response to growth factors, hormones, and glucose [5]. Particularly mTORC1, activated in the presence of amino acids, phosphorylates protein ATG13; this protein inhibits the activation of autophagy, a process by which intracellular lysosomal activity decomposes aggregates.

In patients with AD, lysosomal activities in the brain related to autophagy have been shown to be impaired [6]. Lower levels of Amyloid beta protein clearance through autophagy contributes to plaque buildup and progression of AD in these patients [7]. Therefore, this experiment explores how inducing autophagy through inhibiting the mTORC1 pathway could help break down Amyloid beta plaques and prevent progression of AD.

### 1.3. *Saccharomyces Cerevisiae*

*Saccharomyces cerevisiae* (*S. cerevisiae*) is a species of yeast commonly referred to as Brewer's Yeast. *S. cerevisiae* is an appropriate model organism for autophagy-related research because it conserves a particular regulatory pathway with mammalian cells called mTOR as TOR [8]. Furthermore, *S. cerevisiae* can easily be cultivated and transformed while also maturing quickly and requiring little maintenance. The *S. cerevisiae* strain that was obtained for this project was genetically transformed in order to use fluorescent markers to detect autophagy [9].

### 1.4. Graphene Oxide

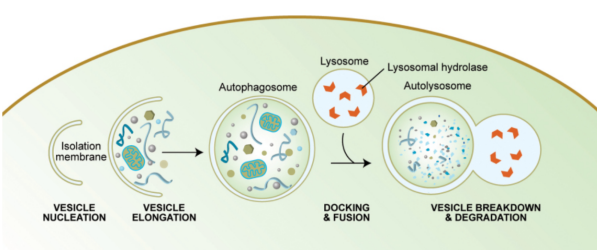


**Figure 2.** The diagram of the autophagy shows the step-by-step process of how autophagy helps break down intracellular molecules.

Graphene Oxide (GO) is made up of a layered carbon structure with functional groups containing oxygen [10]. It has been shown to have promising properties for numerous applications including field-effect transistors, biomolecule sensors, graphene batteries, and conductive films. GO has also been shown to be a potential inhibitor to various intracellular pathways [11]. Particularly, supporting evidence shows that GO could induce autophagy in human microglia and neurons [7]. In this experiment, GO is tested as a potential inhibitor of the TORC1 pathway in *S. Cerevisiae* to induce a dose dependent autophagic response.

### 1.5. Rosella Plasmid

Rosella is a fluorescent reporter of autophagy which is composed of green and red markers. When autophagy is induced emissions of specific wavelengths can be detected after excitations using a spectrophotometer. By transforming the yeast with a Rosella plasmid, this method can be used to detect induced autophagy. 10µL of the Plasmid required for the transformation was obtained from the Dohlman Laboratory at UNC Chapel Hill in an Eppendorf.

## 2. MATERIALS AND METHODS

### 2.1. *S. cerevisiae* Strain

The WB BY4741 strain of *S. cerevisiae* was obtained from Dohlman Laboratory at UNC Chapel Hill with the following selection: his3D1 leu2D0 ura3D0 met15D0 LYS2. All the strains were maintained at 30° C in an incubator on the YPD plates upon which they were shipped and were periodically used to inoculate dispersions.

### 2.2. Plasmid Transformation

To transform the yeast, 10mL of all buffers were formulated according to the following recipes:

#### 2.2.1. Resuspension Buffer:

- 1 mL 10X TE pH 8.0
- 1 mL 1M LiAc
- 8 mL  $H_2O$

Use HCl as needed for pH

#### 2.2.2. 10XTE:

- 100 mM Tris-Cl pH 8.0
- 10 mM EDTA pH 8.0

Use HCl as needed for pH

#### 2.2.3. Transformation Buffer:

- 100 µL 10X TE
- 100 µL 1M LiAc
- 800 µL 50% PEG3350

#### 2.2.4. 50% PEG3350:

- Dissolve 50g PEG3350 into 30ml  $H_2O$
- Warm and stir
- Bring volume to 100mL

All solutions were immediately autoclaved or filter sterilized.

Under sterile conditions, 5mL of Luria Broth (LB) was inoculated using a sterile inoculating loop from the WB BY4741 plate. This dispersion was placed in a shaking incubator at 30°C until saturation. This dispersion was then added to 50mL of LB and incubated at 30°C until the OD<sub>600</sub> was in the range of 0.8-1.2. After vortexing to ensure a homogenous solution, 45mL of the dispersion was separated in three 15mL centrifuge tubes. The yeast was then pelletized in a centrifuge at 3000 RPM for 5 mins before being washed in 15mL water (LB was siphoned off). This washing process was repeated and resulted in a 15mL H<sub>2</sub>O dispersion. This yeast was then pelletized again and 1mL of Resuspension buffer was added after siphoning off the excess H<sub>2</sub>O. The 1mL dispersion was transferred to an Eppendorf and vortexed to ensure homogeneity. The solution was then washed with 1mL of Resuspension Buffer after being pelletized at 18000 RPM for 30 seconds. To obtain an optimal number of yeast cells, the concentration of the solution was determined by counting 10µL of cells in a hemocytometer microscope slide. Using the concentration, the volume of the dispersion required to obtain 1-2 x 10<sup>7</sup> yeast cells was determined.

5mL of Salmon Sperm was submerged in a hot water bath at 90°C for 5 minutes to denature before being cooled in an ice water bath until room temperature was reached. To the Eppendorf containing 10µL of the Rosella plasmid, 50µL of denatured Salmon Sperm, the determined volume of competent yeast cells dispersion, and 600µL of Transformation Buffer were added. After gently vortexing this solution to mix, it was incubated at 30°C for 30 minutes, then at 42°C for 20 minutes. Finally, this solution was washed twice with 1mL of H<sub>2</sub>O after centrifugation for 30 seconds at 2500 RPM before a final volume of 200µL of H<sub>2</sub>O was added. This solution of transformed S. cerevisiae was streaked onto SC-LEU-ampicillin plates to ensure strain selection.

### 2.3. Cytotoxicity Assay

To prepare the 4 concentrations of GO in LB used to test the cytotoxic effect of GO on S. cerevisiae, 6mg of GO flakes was added into 30mL of sterile LB. This dispersion was then sonicated for 3 hours. While vortexing, the 1.25mL wells were each filled with the 200µg/L broth. Then 22.5 mL of sterile LB was added to the solution, causing the concentration of GO to halve to 100µg/L. After the next 6 wells were filled with dispersion, 37.5 mL of sterile LB was added to bring the concentration down to 50µg/L. After the next 6 wells were filled with dispersion, 67.5 mL of sterile LB was added to bring the concentration down to 25 µg/L. This concentration was used to fill the next column of 6 wells. Finally, plain LB was added to two columns as the control group (0µg/L) and the blank. Then, all the wells were inoculated with yeast except the blank column using a sterile inoculation loop. The plate was then placed for 72 hours in an incubating multimode microplate reader at 30°C with orbital shaking at 200 rpm. Optical density at 600 nm was measured automatically in five minute intervals.

### 2.4. Fluorescence Marking Assay

To prepare the two concentrations of GO in LB solutions, 50µg/L and 100µg/L, 25mg of GO flakes was added to 250mL of LB. This solution was sonicated for 5 hours in 30 minute intervals. After each interval, the solution was vortexed. Finally, the resultant dispersion was autoclaved. The 250mL dispersion was then split into two

125mL dispersions with the concentration of each being 100µg/mL. One of the dispersions was then added to 125mL of LB to reduce the concentration to 50µg/mL.

Into a 96 well black plate, 48 wells were filled with 200µL of the 100µg/mL GO-LB dispersion, while the remaining 48 wells were filled with 200µL of the 50µg/mL GO-LB dispersion. Finally, each well was individually inoculated with the transformed yeast and the plate was incubated for 24 hours at 30°C to initiate autophagic processes. The plate was then measured at 485/20 nm excitation and 528/20 nm emission with a resultant fluorescence reading for each well.

## 3. DATA/RESULTS

### 3.1. Cytotoxicity Assay

To determine if GO inhibits the regular growth and cell proliferation rates of S. cerevisiae, the yeast was grown in a growth medium which contained determined concentrations of GO. The Optical Density at 600 nm (OD<sub>600</sub>) determines the level of yeast proliferation in the well with higher OD<sub>600</sub> signifying more proliferation.

**Figure 3** displays a clear logistic growth curve for the S. cerevisiae grown in all concentrations. There is a clear lag, logarithmic, and stationary phase regardless of concentration. In addition, the OD<sub>600</sub> of the non-inoculated blank group remained at 0 which confirms the absence of any contamination. There was no significant difference in the rate or intensity of S. cerevisiae cell proliferation/growth when grown in different concentrations of GO.

### 3.2. Fluorescence Marking Assay

Once it was determined that there were no cytotoxic effects of GO on S. cerevisiae growth, GO was applied in the growth medium of the transformed S. cerevisiae to determine its effectiveness in inducing autophagy. The fluorescent readings at 485/20 nm excitation and 528/20 nm emission illustrate the ubiquity of autophagy induction in the samples.

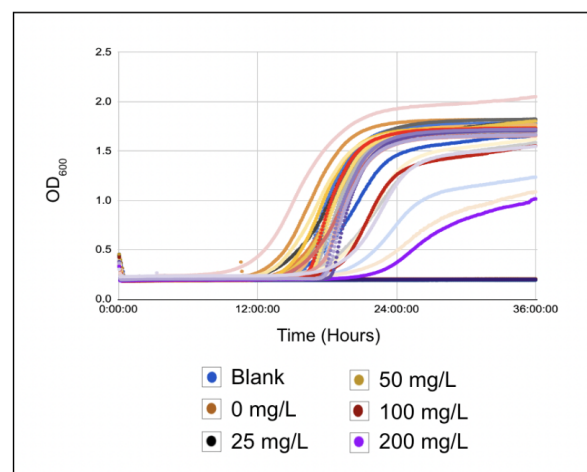


**Figure 3.** Dose dependent OD<sub>600</sub> growth curve: The Optical Density of each well at 600 nm was measured every 5 minutes and plotted over time resulting in a logistic growth curve showing the proliferation of S. cerevisiae in all inoculated wells.

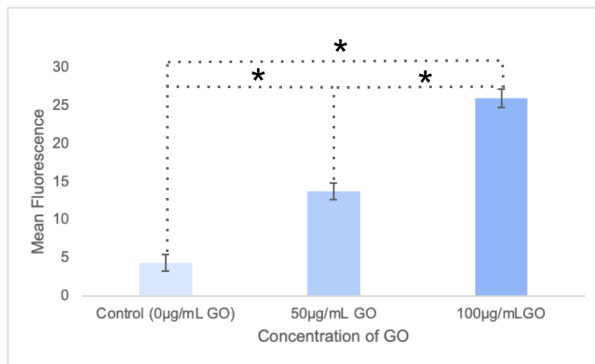


**Figure 4.** Fluorescent analysis of dose dependent autophagy induction: The fluorescence emission at 528/20 nm was recorded for 32 wells for each group including the control. The average of these values were plotted.

Figure 4 displays a significant dose dependent trend of fluorescence increasing with higher GO concentrations. A mean fluorescence reading of 4.38 was recorded for the control group; the 50 $\mu$ g/mL GO group had a mean fluorescence reading of 13.8; finally, the 100 $\mu$ g/mL GO group recorded a mean fluorescence reading of 26.0.

#### 4. DISCUSSION AND LIMITATIONS

##### 4.1. Cytotoxicity of Graphene Oxide to *S. cerevisiae*

Figure 3 demonstrates that GO does not have a significant cytotoxic effect on the cell proliferation of *S. cerevisiae*. The OD<sub>600</sub> of each well, regardless of GO concentration, traced the standard logistic curve of *S. cerevisiae* growth. Furthermore, the curves representing the 0 mg/L, 25 mg/L, 50 mg/L, 100 mg/L, and 200 mg/L groups all overlapped throughout the 36 hours without significant variances, showing the same proliferation rate regardless of concentration. Therefore, higher GO concentrations did not have cytotoxic effects on *S. cerevisiae*. Because GO is not cytotoxic to *S. cerevisiae*, it can be tested as an autophagy inducer in *S. cerevisiae*.

##### 4.2. Autophagic Response of *S. cerevisiae* to Graphene Oxide

Figure 4 demonstrates a dose-dependent effect of GO on autophagic rate of *S. cerevisiae* in the wells. When comparing either group which included GO, 50 $\mu$ g/mL or 100 $\mu$ g/mL, to the control group with no GO, there was a significant difference in the mean fluorescence reading. With both of these groups with GO compared to the control, there was significantly higher mean fluorescence indicating significantly higher autophagic activity. In other words, the presence of GO inhibited the TORC1 pathway and activated autophagy in the *S. cerevisiae*.

This effect also appears to be dose-dependent as greater concentrations of GO resulted in significantly higher rates of autophagy. This is shown in the significant difference in mean fluorescence between the 50 $\mu$ g/mL group and the 100 $\mu$ g/mL group. This dose dependence indicates that more quantity of GO is more effective in inhibiting the TORC1 pathway in *S. cerevisiae* and inducing autophagy.

The induction of autophagy at a dose dependent rate also incites a greater potential for amyloid beta plaques to be broken down with higher concentrations of GO.

#### 4.3. Limitations

The scope of this study focused on inducing autophagy in *S. cerevisiae*, not directly on amyloid beta plaques. Therefore, though suggestions that amyloid beta plaques could be broken down at greater rates in the presence of GO due to autophagy can justifiably be made, more research is necessary for conclusive results.

Furthermore, cytotoxicity of GO to *S. cerevisiae* was determined for the chosen concentrations, however, higher/lower concentrations should be tested to determine the viable range for GO.

Another limitation is that the transformation of the yeast with the Rosella plasmid occurred over the course of three work days. Overnight, certain mixtures of ingredients from the middle of the protocol were left sitting which could have affected the quality of the produced *S. cerevisiae* strain.

#### 5. CONCLUSIONS AND FUTURE WORK

The results from the cytotoxicity assay and the fluorescent indicator assay support that Graphene Oxide is a viable candidate to break down amyloid beta plaques. The initial cytotoxicity assay validated the results by providing evidence that GO was not cytotoxic to the *S. cerevisiae* and did not inhibit cell proliferation. By transforming the *S. cerevisiae* to include a fluorescent indicator of autophagy, the process by which amyloid beta plaques can be broken down, the inhibitory effects of GO on the TORC1 pathway which regulates autophagy became clear. The data strongly supports that autophagy is not only induced by the presence of GO, but also that greater concentrations of GO result in a dose dependent increase in autophagic response.

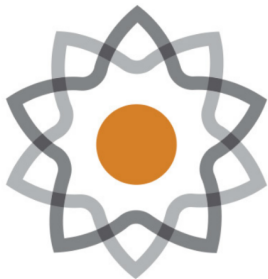
The next step is to determine the effects of GO directly on amyloid beta plaques in model organisms such as *Caenorhabditis elegans* or *Drosophila melanogaster* which can directly model said plaques. Moreover, the effects of a continuous reintroduction of GO into the growth medium could provide insight into the inhibition of the TORC1 pathway. Finally, Western Blot or ELISA assays which can test the presence and concentration of autophagy-related proteins (ATG 13) could further confirm the induction of autophagy.

#### ACKNOWLEDGEMENTS

I would like to sincerely thank Mr. James Happer and Mrs. Jennifer Williams for providing me with the opportunity as well as constant guidance and feedback throughout my research journey. Their unwavering support and mentorship has been invaluable in overcoming the obstacles and roadblocks. I would also like to sincerely thank Dr. Henrik Dohlman and Mr. Dalton Taylor of the Department of Pharmacology - Dohlman Laboratory at the University of North Carolina Chapel Hill for providing me with the strain of yeast and the Rosella plasmid as well as guidance and support. I would also like to thank the North Carolina School of Science and Mathematics which provided me with the opportunity to conduct a research project as a part of the Research in Science program. Finally, thank you to Carolina Biological Supply and Thermo Fisher for supplies.

## REFERENCES

- [1] N. I. of Aging, "What Is Alzheimer's Disease?" [Online]. Available: <https://www.nia.nih.gov/health/alzheimers-and-dementia/what-alzheimers-disease>
- [2] *Alzheimer's & Dementia*, vol. 18, no. 4, pp. 700–789, 2022, doi: [10.1002/alz.12638](https://doi.org/10.1002/alz.12638).
- [3] A. S. of Canada, "How Alzheimer's disease changes the brain." [Online]. Available: <https://alzheimer.ca/en/about-dementia/what-alzheimers-disease/how-alzheimers-disease-changes-brain>
- [4] W. H. Organization, "Dementia." [Online]. Available: <https://www.who.int/news-room/fact-sheets/detail/dementia>
- [5] Z. Zou, T. Tao, H. Li, and X. Zhu, "mTOR signaling pathway and mTOR inhibitors in cancer: progress and challenges," *Cell & Bioscience*, vol. 10, no. 1, 2020, doi: [10.1186/s13578-020-00396-1](https://doi.org/10.1186/s13578-020-00396-1).
- [6] M. S. Uddin *et al.*, "Autophagy and Alzheimer's Disease: From Molecular Mechanisms to Therapeutic Implications," *Frontiers in Aging Neuroscience*, vol. 10, 2018, doi: [10.3389/fnagi.2018.00004](https://doi.org/10.3389/fnagi.2018.00004).
- [7] X. Li, K. Li, F. Chu, J. Huang, and Z. Yang, "Graphene oxide enhances  $\beta\eta$ -amyloid clearance by inducing autophagy of microglia and neurons", *Chemico-Biological Interactions*, vol. 325, p. 109126–109127, 2020, doi: [10.1016/j.cbi.2020.109126](https://doi.org/10.1016/j.cbi.2020.109126).
- [8] Y. Inoue and W. Nomura, "TOR Signaling in Budding Yeast," in *The Yeast Role in Medical Applications*, InTech, 2018. doi: [10.5772/intechopen.70784](https://doi.org/10.5772/intechopen.70784).
- [9] N. Rangarajan *et al.*, "Potassium starvation induces autophagy in yeast," *Journal of Biological Chemistry*, vol. 295, no. 41, pp. 14189–14202, 2020, doi: [10.1074/jbc.ra120.014687](https://doi.org/10.1074/jbc.ra120.014687).
- [10] A. Jíříková, O. Jankovský, Z. Sofer, and D. Sedmidubský, "Synthesis and Applications of Graphene Oxide," *Materials*, vol. 15, no. 3, p. 920–921, 2022, doi: [10.3390/ma15030920](https://doi.org/10.3390/ma15030920).
- [11] A. Trusek, E. Kijak, and L. Granicka, "Graphene oxide as a potential drug carrier – Chemical carrier activation, drug attachment and its enzymatic controlled release," *Materials Science and Engineering: C*, vol. 116, p. 111240–111241, 2020, doi: [10.1016/j.msec.2020.111240](https://doi.org/10.1016/j.msec.2020.111240).



# The Morganton Scientific

*North Carolina  
School of Science and  
Mathematics*

Journal of Student STEM Research

Published Jun 27, 2024

Correspondence to  
Prerana Kulla  
kulla25p@ncssm.edu

Open Access   
Copyright © 2024 Kulla & Solomon. This is an open-access article distributed under the terms of the Creative Commons Attribution 4.0 International license, which enables reusers to distribute, remix, adapt, and build upon the material in any medium or format, so long as attribution is given to the creator.

## Assessing the Impact of Water, Algae, Alcohol, and Oil-Based Inks on the Biodegradability of Cellulose in Filter Paper

Prerana Kulla<sup>1</sup> , and Sophia Solomon<sup>1</sup> 

<sup>1</sup>North Carolina School of Science and Mathematics 

### Abstract

This study evaluated the effects of several ink types on the biodegradability of cellulose. Paper is one of the main components of cellulosic waste, which is a major environmental problem worldwide. The effects of several ink types, such as alcohol-based, water-based, algae-based, and oil-based inks, on the degradation of cellulose were studied. Given the abundance of cellulose in many everyday commodities, cellulose breakdown is essential for waste management and environmental sustainability. A new cellulase-producing fungus discovered in Burke County was used in the study to evaluate how filter paper treated with various inks degraded. Different types of inks showed different levels of degradation based on visual observations; oil- and alcohol-based inks showed negligible degradation, whereas water and algae-based inks showed significant degradation. The qualitative observations were verified by quantifying enzyme activity and substrate degradation through spectrophotometer experiments. According to statistical analysis, inks based on water and algae degraded cellulose at higher rates than control samples, while inks based on oil and alcohol degraded at lower rates. The study shows how various ink types affect the environmental impact of cellulose biodegradability and highlights the possibilities of water- and algae-based inks as sustainable substitutes. To further understand the precise mechanisms behind ink impacts on cellulose degradation and to optimize ink formulations for increased environmental sustainability, more research is necessary.

**Keywords** Cellulose biodegradation, Ink sustainability, Enzyme activity

### 1. INTRODUCTION

Cellulosic waste is becoming more and more of a global problem. Organic components of cellulosic wastes include paper, tissue, filters, fabric, and wood [1]. Cellulose's abundance and commercial availability make it a common raw material used in producing many commodities. Unfortunately, much of the waste from these goods is often disposed of through burning biomass, which is not restricted to developing countries alone but is considered a global phenomenon [2]. Agricultural and industrial wastes are some of the leading causes of environmental pollution. Proper biotechnological utilization of these wastes will eliminate their pollution and turn them into useful by-products [3]. Due to the massive applicability of cellulase, it has been used in various industrial processes such as the production of biofuels – like bioethanol [2]. Cellulose is a linear polymer of glucose residues connected by  $\beta$ -1, 4-glycosidic bonds. Cellulose degradation is accomplished by “cellulases,” which are the enzymes that hydrolyze the  $\beta$ -1,4-linkages found in cellulose [2]. Cellulose breaks down into glucose by a very specialized process called depolymerization, which only requires a small number of saprophytes [4]. However, the degradation rates can be affected when ink comes into contact with cellulose, whether on a box or paper packaging. Biodegradation of cellulose is significant, and it is proven that the degradation rate is negatively affected by petroleum ink. The most crucial worldwide issue now is environmental pollution caused by petroleum and petrochemical goods. Ecological life is severely harmed by these waste emissions derived from petroleum [5]. Due to this issue and the goal of reducing pollution, sustainability, and waste reduction, many companies have invented and used water, algae, alcohol, and many other types of inks. Making sure that the majority of the ingredients utilized in the formulation

are biobased, biodegradable, or do not qualify as crucial raw resources is essential to producing sustainable inks [6].

Cellulases produced by fungi and bacteria play the most important microscopic role in the breakdown of cellulose. High-yield cellulose-degrading bacteria are environmentally friendly, inexpensive, convenient, and do not cause secondary pollution. Several studies have shown that these functional bacteria isolated from cellulose-rich waste environments can considerably accelerate the degradation of cellulose, improve the conversion efficiency of agricultural waste composting, and speed up the process of composting. Studying their ability to produce enzymes and degrade cellulose will help to find high-quality strains that can efficiently break down cellulose [7].

When the first black ink made from algae was invented by two molecular biology Ph.D. candidates at Colorado State University, they were studying biofuels and bioproducts. They later founded Living Ink Technologies, which makes Algae Black – a greener pigment substitute for carbon black made from petroleum. Algae-based inks, which have no volatile organic compounds and are renewable and biodegradable, are thought to be the most sustainable. Water-based inks, when applied in flexography and gravure printing, contain up to 60% volatile organic compounds. The benefits of this liquidity are now the main focus of environmental conservation initiatives [8]. Alcohol-based inks are considered environmentally sustainable due to their lower levels of volatile organic compounds, biodegradability, and often lower toxicity. Some formulations use ethanol derived from renewable resources, contributing to a reduced environmental impact. Additionally, the energy efficiency of production processes further enhances the overall sustainability of alcohol-based inks [8]. Oil-based inks can be environmentally harmful due to petroleum-based solvents, high Volatile organic compounds (VOC) levels, including toluene, benzene, and xylene, and the environmental impact of petroleum extraction ([psprint.com](https://psprint.com)). Along with the algae ink, water-based ink, alcohol-based ink, and oil-based ink, this study also included a control variable that had no ink on the filter paper.

However, the larger question is whether these new inks are efficient in progressing the biodegradability of cellulose (in the form of filter paper). Do they hinder its biodegradability? By answering these questions, we can measure to what extent the environment will be affected by the type of ink. This study explores whether the type of ink significantly correlates with the biodegradability of our cellulose substrate in the presence of *Pseudopithomyces* fungus found here in Burke County.

## 2. METHODS

### 2.1. Cellulose Substrates and Inks

Whatman 1 Filter paper which has a diameter of 70 mm was used as the cellulose substrate. Four inks were used in this experiment. Water-based ink came from SiegWerk Environmental Inks. Oil-based ink came from Painters Opaque Paint Markers. Algae-based ink was acquired from EcoEnclose and developed by Living Ink Technologies. Lastly, alcohol-based ink came from a standard black permanent Sharpie marker.

### 2.2. Preparation of Experimental Setup

The four different inks were applied to each substrate piece, and one piece was left blank to use as the control. It ensured that each piece of filter paper was fully covered with ink. The algae ink was applied onto the substrate by smearing it with gloves. The water-based ink was applied using an Anilox hand ink roller. This was done twice, which resulted in a total of ten samples. 10 Fisher Brand 75cm<sup>2</sup> vented cap culture flasks were obtained and each was filled with 30 ml of clear Miracle Grow solution. The plates of the unidentified Burke County fungal cultures were obtained. A 1000 ml pipette tip was used to puncture a hole in the agar of the fungal plate, and a sterile wooden stick was used to place the cut fungal sample into the culture flask. This was repeated ten times, for each culture flask. Each substrate was then placed into its labeled flask. A sterile plastic loop was used to adjust the substrate and flatten it, so it was completely submerged in the Miracle Grow.

### 2.3. Biodegradation Experiment

Different experimental groups were used for this experiment. The ink for each test group was acquired from the aforementioned sources listed above. Each filter paper (cellulose) was treated with a distinct ink type; this resulted in ten samples. Approximately one layer of ink was applied to the filter paper.

### 2.4. Analytical Technique

To quantify the degradation of the filter paper and how it varied within each of the experimental groups, a Vernier Go Direct SpectroVis Plus spectrophotometer was used. The spectrophotometer was used in each respective solution to measure the absorbance of light based on how dark in color it was. Seven cuvettes, one 15 mL conical tube, 1.5 mM Substrate (p-nitrophenol), Resuspension Buffer, Stop Solution, and the enzyme were gathered. One out of the ten samples from the experiment was chosen to serve as the enzyme for each spectrophotometer trial. The conical tube was labeled "Enzyme Reaction". Five of the cuvettes were labeled E1-E5. The remaining two cuvettes were labeled "Start" and "End". 500 uL of stop solution was pipetted into each cuvette. Three mL of 1.5 mM Substrate was pipetted into the enzyme reaction tube. 250 uL of the enzyme extract sample was pipetted into the enzyme reaction tube. The timer was started. 500 uL was pipetted out of the enzyme reaction tube and into the cuvettes labeled E1-E5 in designated increments (E1 at 1 minute, E2 at 2 minutes, E3 at 4 minutes, E4 at 6 minutes, and E5 at 8 minutes). 500 uL of suspension buffer was added to the sixth cuvette as well as a drop of the enzyme sample to be used as a blank for the experiment. This was used to calibrate the spectrophotometer before measuring the absorbance. In order to find the absorbance levels for the spectrophotometer the Beer-Lambert law was used. This law describes the relationship between the concentration of an analyte in a solution and the amount of light it absorbs. This relationship is formulated as  $A = \epsilon bc$ , where A represents the absorbance of light by the solution,  $\epsilon$  denotes the molar absorptivity of the analyte, b is the path length (the length of the solution through which the light passes), and c stands for the analyte's concentration. By doing a spectral scan, we found that at 415 nm, the absorbance was the highest therefore, we stuck with that absorbency. Each cuvette (E1-E5) was carefully wiped down with a KimWipe before being placed in the spectrophotometer. This was repeated for each of the other four

cuvettes. This entire procedure was then repeated using each of the other nine samples. Google Sheets was used to record the data collected from the spectrophotometer. GraphPad Prism software was used to analyze the data.

### 3. RESULTS

In order to measure the degradation of the substrate in the 10 samples, an enzyme assay was performed and the results were measured using a spectrophotometer. Given that there were two samples of each experimental group, it was expected for both samples to be relatively similar to each other in terms of how much they degraded. Some of the results produced held true to that belief while others did not.

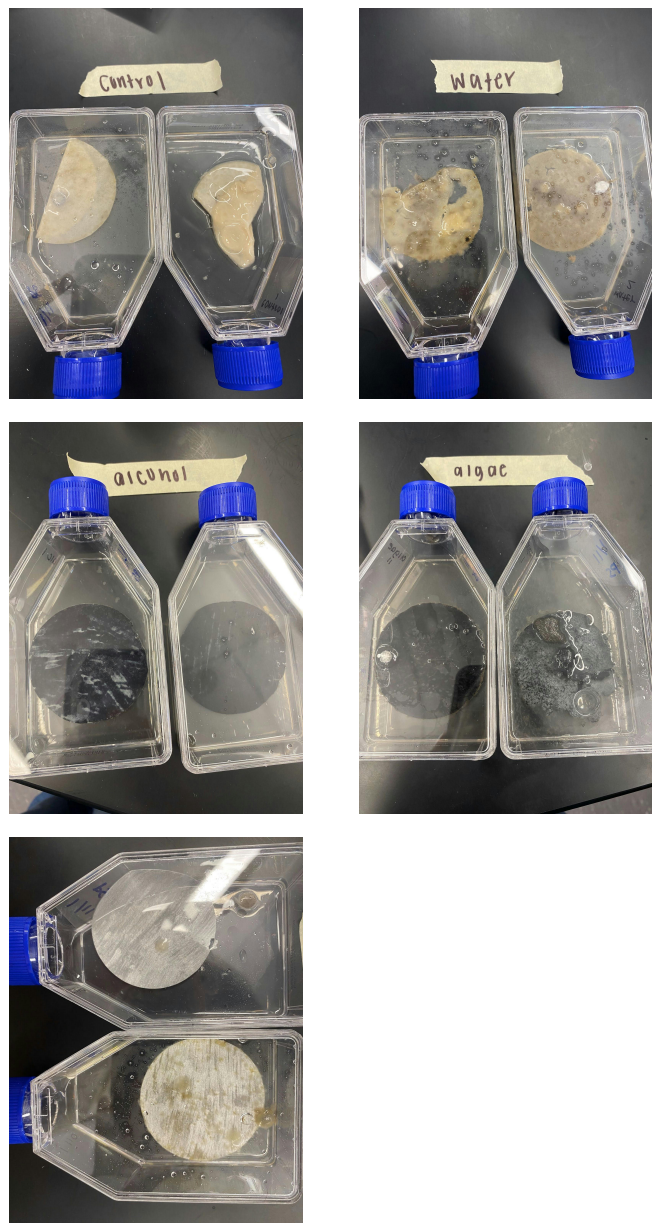


**Figure 1.** Degraded samples (replicate 1): control

Visual examination of the results revealed (shown in Figure 1) that algae ink and water-ink treated substrates were very degraded.

Time Elapsed (in min)	Water 2	Water 1	Control 2	Control 1	Oil 1	Oil 2	Alcohol 1	Alcohol 2	Algae 1	Algae 2	Miracle Gro
1	0.698	0.468	0.455	0.725	0.582	0.521	0.622	0.478	0.746	0.601	0.477
2	0.684	0.664	0.545	0.712	0.6	0.545	0.637	0.554	0.781	0.629	0.486
4	0.737	0.731	0.49	0.766	0.65	0.562	0.642	0.568	0.877	0.691	0.44
6	0.851	0.782	0.538	0.765	0.648	0.535	0.655	0.575	1.023	0.727	0.468
8	0.858	0.853	0.588	0.807	0.699	0.57	0.663	0.569	1.12	0.83	0.502

**Table 1.** All values obtained from spectrophotometer for each enzyme for each enzyme assay performed (one done for each sample) at 415 nm

However, one of the algae ink samples was more degraded than the other. Algae 1's filter paper had lost its original circular shape and had fungal growth on its surface. Algae 2's filter paper was still mostly circular, yet it also had extensive fungal growth on its surface and appeared to have extreme deterioration. Water 1 filter paper was extremely degraded, having turned a yellowish-brown color from the surface fungal growth. It lost much of its original surface area and had holes that the fungus had eaten. Water 2's filter paper also had a brownish-yellow color with its surface entirely covered in fungal growth, but it had more of its original surface area remaining. Control 1 and 2 filter papers were visibly less degraded than the algae and water-based ink samples, yet they both had a beige color from fungal growth. Contrastingly, the oil-based inks were the least degraded. The original silver color of the filter papers of Oil 1 and 2 was still visible and the paper seemed to maintain its original thickness and shape. Interestingly, Oil 1 had some fungal growth on the surface while Oil 2 did not. Alcohol 1 and 2 filter papers did not appear to have much growth on the surface or degradation.

Further steps were taken to analyze and learn more about the visual notes that were made. As mentioned in the methods section, an enzyme assay was conducted. Our results were measured by how yellow it turned when the p-nitrophenol (1.5 mM substrate) came into contact with the stop solution, thus showing how active the enzyme was. By receiving spectrophotometer results and quantifying the intensity of the yellow color produced in the cuvette samples, our results were compiled into Table 1. As seen with each of the samples, the value of the spectrophotometer reading of absorbance increased over time meaning that the enzyme activity increased as it degraded the substrate. Miracle-Gro was also run through the enzyme assay on its own to ensure that it as a medium was not accounting for the relatively high starting spectrophotometer readings but rather that it was the enzyme itself. Putting Miracle-Gro into the stop solution at selected intervals did cause a pH-influenced color change with an absorbance range of 0.44-0.502 (as shown in Table 1). Upon graphing this and finding the line of best fit, it was determined that the linear slope was around 0.002 which is very close to zero. All ten samples' spectrophotometer results were graphed and a line of best fit was made to find the slope (as shown in Table 2).

After recording the slopes of all ten samples, the average slope of the 1 and 2 samples of each ink type was calculated. These new

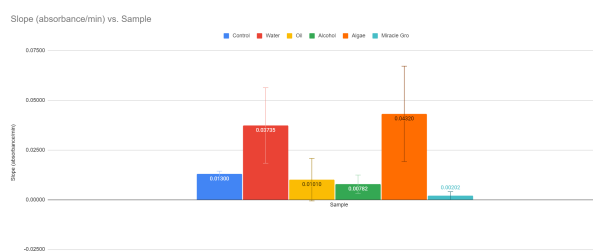
Sample	Slope (absorbance/min)
Control 1	0.0137
Control 2	0.0123
Water 1	0.0276
Water 2	0.0471
Oil 1	0.0156
Oil 2	0.00459
Alcohol 1	0.00543
Alcohol 2	0.0102
Algae 1	0.0554
Algae 2	0.031

**Table 2.** Slopes of each sample's absorbance found in the Enzyme Assay

slopes, adding the slope of Miracle-Gro as well, were visualized in a bar chart (shown in Figure 2). Notably, the average slope of Water was 0.0374 absorbance/min compared to the average slope of Control of 0.0130 absorbance/min. The average slope of Algae was even higher, at 0.0432 absorbance/min. The average absorbance/min of Oil was 0.0101, while Alcohol's value was even lower at 0.0078. Miracle Gro's slope was the lowest, as expected, at 0.0020 absorbance/min. The error bars in Figure 2 were calculated using the 95% confidence interval of the standard error. Two-tailed 0.05 significance p-values were also calculated for the slopes of each ink type in relation to the control group. The p-value for Control and Algae was 0.132. The p-value for Control and Water was 0.130. The p-value for Control and Oil was 0.653. The p-value for Control and Alcohol was 0.172. The p-value for Alcohol and Algae, the two extremes of the average slopes, was 0.104. Our p-values showed that the differences seen between ink types were not statistically significant, given our preliminary data.

#### 4. DISCUSSION

The visual examination of the samples yielded important information about how different types of ink affect the biodegradability of cellulose. Significant degradation of the filter paper was seen in both water-based and algae-based inks, with notable variation between the two samples of algae ink. On the other hand, oil-based and alcohol-based inks exhibited the least amount of degradation, preserving their original look with little fungal development. These qualitative findings could support the theory that the type of ink used affects the biodegradability of

**Figure 2.** Barchart showing the average of the absorbance slopes of samples 1 and 2 of each ink type

cellulose, with oil-based and alcohol-based inks inhibiting degradation if this experiment was replicated with multiple trials. It's important to consider, however, that the application of the ink to the different filter paper is very hard to control. When applying the alcohol-based ink which was in the form of a Sharpie marker, it was easy to add strips of the ink. This method is much closer to having one layer of ink on the filter paper—which was the goal. However, with other experimental groups such as the algae ink, it was much harder to control the amount of ink that was meant to be on the filter paper since the liquid ink was painted on. This method was uncontrolled and could have had confounding effects on the results.

While conducting this experiment, questions arose as to whether or not the absorbance values were a result of the enzyme activity or whether the results came from the activity of the medium that was used: Miracle-Gro. Instead of using an enzyme sample in this unplanned experimental group, only a Miracle-Gro solution was used. These results showed a change in color but the increase in absorbance over time was a negligible amount.

The age of substrate used while performing the enzyme assay was crucial. 1.5 Mm substrate was used and the exact vial that was being used was not initially tracked. There were multiple 1.5 Mm substrate vials, all of varying ages. One of the experiment groups had a different 1.5 Mm substrate used which produced peculiar findings as this 1.5 Mm substrate generated significantly lower readings on the spectrophotometer. Upon realizing this, the new substrate was removed and throughout the rest of the experiment, the older vial was used. Therefore, the sample that led to this finding was discarded.

The spectrophotometer-assisted enzyme assay produced quantitative data that supported the qualitative observations. As the substrate broke down over time, the absorbance values showed rising enzyme activity, with variances seen among various ink kinds. Calculating the average slopes of absorbance/min for every type of ink revealed different tendencies in the rates of cellulose degradation. In comparison to control samples, inks based on water and algae showed larger average slopes, suggesting faster degradation. Oil-based inks, on the other hand, had lower slopes, indicating slower rates of deterioration. These results could have had some confounding effects too. Two different spectrophotometers were used when collecting data. Due to having to recalculate the absorbance for one of the samples, it was found that one of the spectrophotometers had slightly lower absorbance quantities than the other spectrophotometer used. In the future, it is important for only one spectrophotometer to be used. This could perhaps be mitigated by using a well plate so that all the samples are calculated at the same time and using a microplate reader to avoid confounding factors such as the surrounding temperature and CO<sub>2</sub> levels.

To assess the statistical significance of the observed differences, further analysis including error bars, t-tests, and p-values was conducted. The statistical significance of each ink type can be determined by comparing both samples' slopes with control sample slopes. Error bars show the variation within each experimental group, giving information about the reliability of the results. A lower p-value (< 0.05) would indicate a higher level of statistical significance, confirming the influence of ink type on cellulose

degradability. By conducting more trials in the future, a lower p-value would likely be found to prove that the differences across ink types are statistically significant.

Nonetheless, our work shows that water-based ink from Siegwerk Environmental Inks and algae ink from Living Ink Technologies does not hinder the degradation of filter paper by *Pseudopithomyces*, a known cellulose degrader. While it cannot be concluded whether they expedited the degradation of the substrate, algae and water-ink-treated substrates performed as well as the control substrates. According to EcoEnclose (Living Ink's packaging partner), Living Ink's algae ink is sustainable, renewable, and biodegradable. Our study did not measure the biodegradability of the ink itself, but we showed that it didn't impede *Pseudopithomyces*'s decomposition of the substrate. Our study is unique from previous studies in that the substrate was covered in different inks to test their effect on the degradation efforts of a known cellulose-degrading microbe. Past studies have looked strictly at the cellulase activity of organisms without ink as a factor. An aforementioned study isolated cellulose-degrading bacteria from various invertebrates and tested their activity against filter paper, similarly using a spectrophotometer in their enzyme assay [2]. Inversely, another previously mentioned study isolated printing ink-degrading bacteria from soil polluted by printing machine waste discharge to see if these microorganisms could be used to break down petroleum-based ink [5]. As shown, our study bridged the gap between previous literature.

Substantial room exists for future work. The research findings from the results can be used to find an ink that enhances cellulose degradation based on the types of inks that were found to degrade the fastest. For example, the algae-based ink would likely be one of the fastest degrading inks, possibly enhancing the enzyme's degradation (however this cannot be concluded without more trials). In the future, it will be ensured that numerous trials are conducted to promote the specificity of the results along with their statistical significance in terms of p-value. The substrate, enzyme, and all other factors will stay fully consistent throughout the experiment to avoid any confounding factors. Only one spectrophotometer will be used throughout, preferably one where samples can be inputted through well plates. This could perhaps be a microplate reader. That way, CO<sub>2</sub> levels, surrounding temperature, and other variables will stay consistent since the microplate reader will be used.

This work is supported by the North Carolina School of Science and Mathematics in Morganton with the help of Jennifer Williams.

## REFERENCES

- [1] C. J. Knill and J. F. Kennedy, "Degradation of cellulose under alkaline conditions," *Carbohydrate Polymers*, vol. 51, no. 3, pp. 281–300, 2003, doi: [10.1016/s0144-8617\(02\)00183-2](https://doi.org/10.1016/s0144-8617(02)00183-2).
- [2] P. Gupta, K. Samant, and A. Sahu, "Isolation of Cellulose-Degrading Bacteria and Determination of Their Cellulolytic Potential," *International Journal of Microbiology*, vol. 2012, pp. 1–5, 2012, doi: [10.1155/2012/578925](https://doi.org/10.1155/2012/578925).
- [3] J. A. R. Jadhav A. R., "Study on the Use of Agricultural Wastes for Cellulase Production by Using *Aspergillus Niger*," *IOSR Journal of Pharmacy and Biological Sciences*, vol. 6, no. 4, pp. 17–20, 2013, doi: [10.9790/3008-0641720](https://doi.org/10.9790/3008-0641720).
- [4] K. Killham and M. Wainwright, "Deciduous leaf litter and cellulose decomposition in soil exposed to heavy atmospheric pollution," *Environmental Pollution Series A*,
- [5] M. A. M. D. Prasanna, N. Siddharthan, K. Raguvaran, P. M. Ayyasamy, N. Hemalatha, and C. Ragavendran, "Eco-friendly bioremediation of petroleum-based inks from printing machine waste implementing native strain *Pseudomonas aeruginosa* MDP14," *Biomass Conversion and Biorefinery*, 2023, doi: [10.1007/s13399-023-05101-z](https://doi.org/10.1007/s13399-023-05101-z).
- [6] L. Sanchez-Duenas et al., "A Review on Sustainable Inks for Printed Electronics: Materials for Conductive, Dielectric and Piezoelectric Sustainable Inks," *Materials*, vol. 16, no. 11, p. 3940–3941, 2023, doi: [10.3390/ma16113940](https://doi.org/10.3390/ma16113940).
- [7] Z.-L. Li et al., "Decorated bacteria-cellulose ultrasonic metasurface," *Nature Communications*, vol. 14, no. 1, 2023, doi: [10.1038/s41467-023-41172-2](https://doi.org/10.1038/s41467-023-41172-2).
- [8] *Chemistry and Technology of Water Based Inks*. Springer Netherlands, 1996. doi: [10.1007/978-94-009-1547-3](https://doi.org/10.1007/978-94-009-1547-3).



# The Morganton Scientific

*North Carolina  
School of Science and  
Mathematics*

Journal of Student STEM Research

## An Investigation of the Economics Behind Air Emergency Medical Services

Noah Langbo<sup>1</sup> 

<sup>1</sup>North Carolina School of Science and Mathematics 

### Abstract

The use of air ambulance services, a critical component of emergency medical response, has become increasingly prevalent in transporting critically ill or injured patients to medical emergency sites. This essay aims to provide a comprehensive understanding of air ambulance services by exploring their definition, importance in trauma care, and the economic and personal finance aspects associated with these life-saving interventions. The significance of air ambulance services in trauma care is underscored by empirical research, highlighting the advantages of high speed, rapid transportation, and access to specialized medical teams for trauma patients. Furthermore, the laws and current economic conditions of air ambulance services is examined through cost comparisons and analyses of factors influencing cost effectiveness. The findings shed light on the balance between the economic viability of air ambulance services and their life-saving potential. Any approach aimed at addressing these economic issues must consider the many perspectives: economic, medical, political, and more.

**Keywords** EMS, Helicopter, Barriers to Entry, Vertical Demand, Supply, Competition

### 1. INTRODUCTION

Air ambulance services are an essential part of emergency medical response, playing a crucial role in quickly transporting seriously ill or injured patients to medical emergency locations. This essay seeks to offer a thorough insight into air ambulance services by examining their definition, significance in trauma care, and the complex economic and personal financial factors linked to these life-saving interventions.

### 2. WHAT ARE AIR AMBULANCES?

To comprehend the significance of air ambulance services, it's essential to define them. According to D. T. N. Nahan [1], an air ambulance **Figure 1** is a specialized medical transport service that utilizes aircraft for the rapid transportation of critically ill or injured patients to medical emergency sites.

This definition encapsulates the essence of a service designed for swift response, emphasizing high speed, rapid transportation, and suitability for long-distance transports.

### 3. IMPORTANCE OF AIR AMBULANCE SERVICES IN TRAUMA CARE

The importance of air ambulance services in trauma care is underscored by research, such as the study conducted by S. M. Haut *et al.* [2]. This research explores the association between helicopter and ground emergency medical services, delving into the impact of helicopter transport on traumatically injured patients. Covering 61,909 patients transported by helicopter and 161,566 by ground, the study reveals that helicopter transport is associated with improved survival to hospital discharge for major trauma patients in Level I or Level II trauma centers [2].

However, the significance of this impact is debated due to limited resources and acknowledged study limitations. The study highlights the complexities of assessing the effectiveness of air ambulance services, including the lack of regression model testing and the inability to account for treatment

Published Jun 27, 2024

**Correspondence to**  
Noah Langbo  
[langbo24n@ncssm.edu](mailto:langbo24n@ncssm.edu)

**Open Access** 

Copyright © 2024 Langbo. This is an open-access article distributed under the terms of the [Creative Commons Attribution 4.0 International license](#), which enables reusers to distribute, remix, adapt, and build upon the material in any medium or format, so long as attribution is given to the creator.



**Figure 1.** This figure displays a version of an air ambulance maintained by MedCenter Air.

assignment differences. Despite these challenges, the research indicates statistically significant greater odds of survival for patients transported by helicopter, especially for those in Level I trauma centers.

The advantages of air ambulance services, including high speed, rapid transportation, and access to specialized medical teams, align with the critical needs of trauma patients. The swiftness of response and the potential for improved survival rates make air ambulances a crucial component in the continuum of trauma care. As we explore the economic and personal finance aspects of air ambulance services, it is crucial to bear in mind the life-saving impact these services can have on individuals facing critical medical emergencies.

#### 4. COST COMPARISON BETWEEN AIR AMBULANCE AND GROUND EMERGENCY MEDICAL SERVICES

Exploring the economic landscape of air ambulance services in comparison to ground emergency medical services unveils a complex interplay of factors influencing cost-effectiveness. M. K. Delgado *et al.* [3] delve into this intricacy by assessing the cost-effectiveness of helicopter versus ground emergency medical services for trauma scene transport in the United States. The study, analyzing 69,700 helicopter transports for trauma, reveals a critical threshold for cost-effectiveness. Helicopter EMS requires a 15 percent reduction in mortality to offset higher costs, transport risks, and overtriage, even with a 10,000 dollar higher cost in rural areas [3]. What this means, is that from an economic perspective, for the higher cost of air ambulances to be justified, patients using the service should be 15 percent more likely to survive to hospital discharge.

It is important to recognize the difference between the usage of these services in urban versus rural settings. Urban settings are more accessible to ground ambulances and are typically shorter distance routes for air ambulances to use. This, among other factors, is what contributes to the higher cost of air emergency services in rural areas as compared to urban areas.

#### 5. FACTORS INFLUENCING COST EFFECTIVENESS

To comprehend the economic nuances, it's imperative to dissect the factors influencing the cost-effectiveness of air ambulance services.

One factor is the magnitude of costs incurred by the treatment of trauma in any setting, a leading cause of years of life lost, amounting to 406 billion dollars per year [3].

The study by D. Michaels, H. Pham, Y. Puckett, and S. Dissanaika [4] contributes further insights by reviewing the National Trauma Data Bank for outcomes in transferred trauma patients transported by helicopter or ground ambulance. Despite the higher costs and limitations of helicopter transport, patients transferred by air show improved survival rates. Logistic regression adjusted for confounders indicates a 57.0 percent lower likelihood of death for helicopter-transported trauma patients [4].

#### 6. ANALYSIS OF COST EFFECTIVENESS STUDIES

Analyzing cost-effectiveness studies sheds light on the balance between the economic viability of air ambulance services and their life-saving potential. M. K. Delgado *et al.* [3] emphasize the need for a mortality reduction threshold of fifteen percent, indicating that the economic justification for helicopter EMS hinges on achieving this improvement in patient outcomes. The results of Michaels analysis, on a first glance, appear to meet this minimum adjustment of fifteen percent in mortality rates.

This analysis underscores the intricacies involved in assessing the cost-effectiveness of air ambulance services. It's not merely about comparing the direct costs but understanding the broader economic impact of trauma on families, EMS, and our broader healthcare system.

#### 7. RELATIONSHIP BETWEEN COST AND INCREASE IN SURVIVAL RATES

The relationship between cost and an increase in survival rates is a critical aspect of the economic evaluation of air ambulance services. The study by S. M. Haut *et al.* [2] provides valuable insights by linking helicopter transport to statistically significant greater odds of survival, especially for patients in Level I trauma centers. The adjusted analysis indicates a 1.5 percent increased absolute rate of improved survival for helicopter transport to Level I trauma centers [2]. The adjusted analysis conducted by Haut considers that patients whose healthcare providers decided to transport via air ambulance are typically in a more critical condition.

It is important to note the distinction between the conclusion of Haut that a 1.5 percent increase in survival was observed with Michaels' conclusion that a 57 percent increase in survival was observed. This is likely due to a difference in the considerations taken about the patient's initial condition when using a particular mode of medical transport was made by an emergency medical response team.

While these services entail a financial burden, the potential improvement in survival rates, especially for patients in critical conditions, adds a layer of complexity to the economic evaluation. This is where the field of behavioral economics enters into view: how does an increased chance of survival justify the increased cost in the human mind? Further research could be conducted to analyze this.

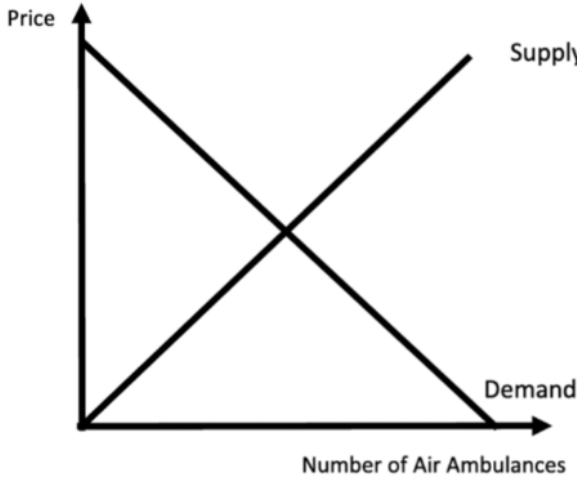


**Figure 2.** This figure displays an ideal supply and demand curve for the air ambulance market [5]. As the supply of air ambulances increases, the price should, in theory, decrease with more ambulances.

## 8. ADDRESSING THE HIGH COSTS OF AIR AMBULANCE SERVICES

550,000 annual air ambulance users face a median cost of 36,000 dollars per trip M. M. D. Goldbeck [5].

The market concentration by notably few firms and the lack of insurance incentives contribute significantly to these exorbitant costs. Notably, the government's hands are tied due to the Airline Deregulation Act of 1978 [6], limiting its authority to address market distortion in the air ambulance industry.

Addressing the pricing and billing challenges is crucial for making air ambulance services more economically sustainable. You might expect a standard supply and demand curve as in many industries (Figure 2), though Goldbeck and Mahoney [5] represent the actual vertical demand curve in the air ambulance industry (Figure 3).

The difference between Figure 2, which represents a standard economic market, and Figure 3, which represents the market of air emergency medicine, is that as the supply of air ambulances increases, the price remains unaffected. In a normal market, when more of a good becomes available, the equilibrium point of the supply-demand curve causes a lower price. Are vertical demand market conditions desired in a life-and-death market? This unique aspect creates a complex economic landscape, where the urgency of the service complicates traditional market dynamics.

Regulatory and policy considerations play a pivotal role in addressing the high costs of air ambulance services. Striking a balance between ensuring fair pricing for consumers and maintaining the financial viability of air ambulance providers requires a nuanced approach. When alterations to the field or air ambulance services could cause lives to be lost, any action taken to address these economic issues must be done so with the utmost caution.

## 9. ECONOMIC IMPACT OF AIR AMBULANCE SERVICES

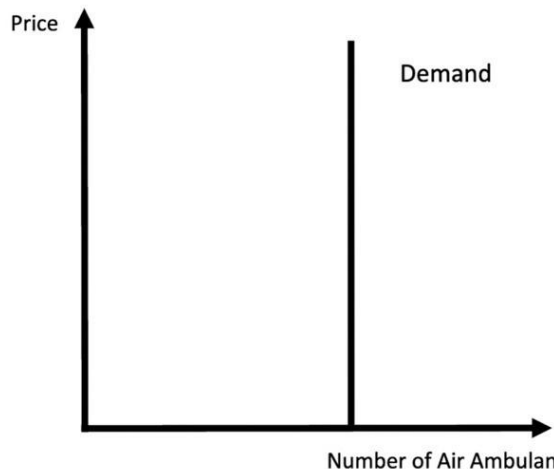


**Figure 3.** This figure displays the actual supply and demand curve for the air ambulance market [5]. As the supply of air ambulances increases, the price remains unaffected as the demand is not dependent on the number of air ambulance services. Please note this is a simplification of the actual market conditions

The economic impact of air ambulance services extends beyond the immediate costs borne by patients. It encompasses a broader perspective, including the impact on the healthcare system and the financial burden imposed on patients and insurance providers.

Examining the broader healthcare system, ltd Brainy Insights Ltd [7] points out that trauma, stroke, and heart attack incidences drive the demand for air medical services. The rising incidence of chronic diseases that Brain Insights LTD forecasts will further contribute to the expansion of the market for air ambulance services. As more and more people are facing life threatening conditions in the not-too-distant future, the demand for these services will increase, begging the question, can our current system handle such demand?

The financial burden on patients and insurance providers is a critical aspect of the economic impact. The high median cost of 36,000 dollars per trip poses a significant financial challenge for individuals requiring air ambulance services. Moreover, the concentration of market power among a relatively small number of firms exacerbates the financial strain on consumers.

The high barriers to entry in the air ambulance services industry create significant difficulties for new entrants. These barriers, such

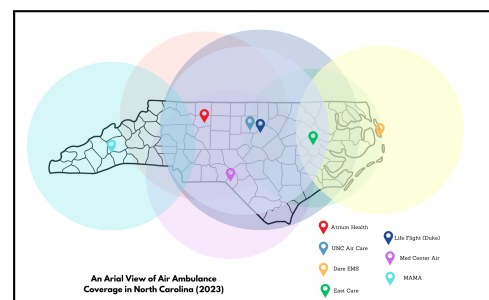


**Figure 4.** This figure displays the air ambulance service territories throughout North Carolina in 2023.

as high startup costs, stringent regulations, and the need for specialized equipment and expertise, make it challenging for new companies to enter the market. As a result, the lack of competition contributes to the concentration of market power among a few firms, further exacerbating the financial strain on consumers and limiting options for patients and insurance providers.

## 10. AIR AMBULANCE SERVICES ACROSS NORTH CAROLINA

When examining the state of North Carolina and the United States, it becomes apparent that issues concerning air ambulance services are prevalent. [Figure 4](#), which has been compiled to demonstrate the availability of such services in North Carolina, reveals that only a few helicopters are operational in certain regions. Most of the helicopter stations depicted house only one helicopter, yet they are responsible for covering extensive areas.

Consequently, when one helicopter is unavailable due to prior engagements, it strains the system, necessitating helicopters to travel towards the outer boundaries of their designated regions, as indicated by the circles surrounding each station. As demand escalates, as previously discussed, this strain on the system intensifies. This shortage of available helicopters in North Carolina will likely extend to a national level within the United States in the coming years.

## 11. CONCLUSIONS

In conclusion, the analysis of air ambulance services reveals a complex landscape involving medical, economic, and policy considerations. The significance of air ambulance services in trauma care, particularly in improving survival rates for major trauma patients, cannot be overstated. The speed, access to specialized care, and rapid transportation offered by air ambulances play a crucial role in addressing critical medical situations.

The cost comparison between air ambulance and ground emergency medical services brings to light various factors influencing cost effectiveness. M. K. Delgado *et al.* [3] emphasize the need for a 15 percent reduction in mortality for helicopter EMS to be cost-effective, even with higher costs in rural areas. D. Michaels, H. Pham, Y. Puckett, and S. Dissanaike [4] further highlight improved survival outcomes for trauma patients transported by helicopter despite higher costs.

Addressing the high costs of air ambulance services is imperative for ensuring accessibility and affordability. Goldbeck and Mahoney [5] shed light on the challenges posed by market concentration and the lack of regulatory authority to address pricing issues. Striking a balance between fair pricing and economic sustainability requires both regulatory and policy considerations.

The economic impact of air ambulance services extends beyond immediate costs. Trauma, stroke, and heart attack incidences drive demand, contributing to the market's expansion [7]. However, the financial burden on patients, with a median cost of 36,000 dollars per trip, poses challenges highlighting the need for comprehensive solutions that consider both healthcare providers and patients.

In summary, the economic sustainability of air ambulance services demands a multifaceted approach. Regulatory frameworks must address pricing challenges, ensuring fair practices that balance the urgency of service with consumer protection. The economic impact on both the healthcare system and individual patients underscores the importance of finding solutions that foster accessibility, affordability, and sustainability in air ambulance services. Steps to find these solutions must be done soon or else we might find ourselves in an under-resourced and under-prepared nation to address the rising number of medical emergencies.

## ACKNOWLEDGEMENTS

The author thanks Ms. Karima Radwan from Raleigh Charter High School and Ms. Beth Thomason from the North Carolina School of Science and Math for their assistance with this work without which this research would not have been conducted.

## REFERENCES

- [1] D. T. N. Nahan, "What Is an Air Ambulance?" [Online]. Available: <https://www.iclinique.com/articles/first-aid-and-emergencies/air-ambulance>
- [2] S. M. Haut *et al.*, "Association Between Helicopter vs Ground Emergency Medical Services and Survival for Adults With Major Trauma," *JAMA*, vol. 307, no. 15, p. 1602–1603, 2012, doi: [10.1001/jama.2012.467](https://doi.org/10.1001/jama.2012.467).
- [3] M. K. Delgado *et al.*, "Cost-Effectiveness of Helicopter Versus Ground Emergency Medical Services for Trauma Scene Transport in the United States," *Annals of Emergency Medicine*, vol. 62, no. 4, pp. 351–364, 2013, doi: [10.1016/j.annemergmed.2013.02.025](https://doi.org/10.1016/j.annemergmed.2013.02.025).
- [4] D. Michaels, H. Pham, Y. Puckett, and S. Dissanaike, "Helicopter versus ground ambulance: review of national database for outcomes in survival in transferred trauma patients in the USA," *Trauma Surgery & Acute Care Open*, vol. 4, no. 1, p. e211, 2019, doi: [10.1136/tsaco-2018-000211](https://doi.org/10.1136/tsaco-2018-000211).
- [5] M. M. D. Goldbeck, "Addressing the High Costs of Air Ambulance Services." [Online]. Available: <https://www.americanactionforum.org/insight/addressing-the-high-costs-of-air-ambulance-services/>
- [6] H. W. Cannon, "95th Congress (1977-1978): Air-line Deregulation Act." [Online]. Available: <https://www.congress.gov/bill/95th-congress/senate-bill/2493>
- [7] Ild Brainy Insights Ltd, "Air Ambulance Market Size Worth \$20.07 Billion by 2030: The Brainy Insights." [Online]. Available: <https://www.globenewswire.com/news-release/2023/02/21/2612639/0/en/Air-Ambulance-Market-Size-Worth-20-07-Billion-by-2030-The-Brainy-Insights.html>



# The Morganton Scientific

*North Carolina  
School of Science and  
Mathematics*

Journal of Student STEM Research

Published Jun 27, 2024

**Correspondence to**  
Taran Puvvala  
[puvvala24t@ncssm.edu](mailto:puvvala24t@ncssm.edu)

**Open Access** 

Copyright © 2024 Puvvala. This is an open-access article distributed under the terms of the [Creative Commons Attribution 4.0 International license](#), which enables reusers to distribute, remix, adapt, and build upon the material in any medium or format, so long as attribution is given to the creator.

 Published by Curvenote

## Predicting Network Traffic Flow with a Multi-Layer Short-Term Memory Model

Taran Puvvala<sup>1</sup> 

<sup>1</sup>North Carolina School of Science and Mathematics 

### Abstract

In the dynamic realm of digital communication, managing and optimizing network traffic is critical. Efficient forecasting of network traffic volumes, crucial for maintaining network quality, poses significant challenges due to the volatile nature of data flow. This study introduces a novel approach using Long Short-Term Memory (LSTM) networks to enhance forecasting accuracy. We compare a multi-layer LSTM, designed to capture complex dependencies within the data, with a traditional single-layer LSTM, offering insights into their respective capabilities. The multi-layer LSTM's architecture allows it to excel in understanding deeper temporal patterns, making it a significant advancement over simpler models. By employing these two architectures, our research aims to improve predictive performance in network traffic forecasting, crucial for optimized network management and planning. The findings reveal that the multi-layer model significantly outperforms its single-layer counterpart, demonstrating the potential of sophisticated LSTM networks in practical applications.

**Keywords** Time-Series, LSTM, Single-layer, Multi-layer

### 1. INTRODUCTION

The forecasting of network traffic volume stands as a cornerstone in the management and optimization of modern data networks [1]. In a digital landscape where data consumption and transmission have surged exponentially, the ability to predict network traffic is paramount. This importance stems from the increasing reliance on online services and cloud computing, with networks serving as the backbone of digital communication [2]. Accurate forecasting enables service providers to maintain network efficiency and quality of service, ensuring that the burgeoning demands of users are met effectively and reliably.

Network traffic volume forecasting is a complex endeavor, often formulated as a Time Series Forecasting (TSF) problem [3]. This task involves constructing models that estimate future traffic volumes based on historical data patterns. However, the inherent challenges of this task arise from the unpredictable and dynamic nature of network traffic, influenced by user behavior, technological shifts, and socio-economic factors. Understanding these dynamics is crucial for creating effective predictive models and maintaining robust network operations [4].

The challenge of forecasting network traffic is amplified by the high dimensionality and large data volumes typical of modern networks. Factors such as emergency situations, varying user demands, and technological changes add layers of complexity to the forecasting process. Accurate predictions require models capable of understanding and adapting to these multifaceted and often nonlinear dynamics [5]. Technologies such as Vehicle-to-Everything (V2X) communications enhance traffic prediction by providing real-time data from vehicles and infrastructure, which can be integrated to forecast traffic flows more accurately [6]. Similarly, advancements in artificial intelligence (AI) facilitate the analysis of complex data patterns, enabling more precise predictions of network traffic behaviors. These technologies contribute significantly to the mapping and predictive capabilities necessary for dynamic network management [6].

Despite its critical importance, network traffic forecasting remains a challenging task. Current methods often struggle to accurately capture the intricate and volatile patterns of network data. Traditional models may not fully account for the nonlinear temporal dependencies and are generally ill-equipped to

handle sudden fluctuations in traffic. This limitation can lead to suboptimal network resource allocation and management, potentially impacting service quality and user experience [7], [8].

Given these complexities, this study aims to explore the application of Long Short-Term Memory (LSTM) networks in predicting network traffic volumes.

Multi-layer Long Short-Term Memory (LSTM) networks offer significant advantages in this context over traditional single-layer LSTMs or other simpler models. By utilizing multiple layers, multi-layer LSTMs can capture more complex and subtle patterns in data, which are often missed by simpler approaches. This capability is especially critical given the complex, nonlinear dynamics of network traffic, which include interactions across various time scales.

Our research focuses on whether LSTM models, renowned for their capability to process time-series data with intricate temporal patterns, can enhance the accuracy of network traffic forecasts. The study specifically examines and compares the efficacy of multi-layer and single-layer LSTM architectures in this context. The overarching goal is to contribute to more efficient and effective network traffic management strategies, aligned with the evolving demands of the digital era [9].

## 2. COMPUTATIONAL APPROACH / METHODS

In the realm of time-series forecasting, the meticulous design and implementation of computational models play a pivotal role in uncovering underlying patterns and predicting future trends. The methods adopted in this study reflect a harmonious blend of advanced data pre-processing techniques, the intricate architecture of neural networks, and strategic model training and testing procedures. By delving into the specifics of Long Short-Term Memory (LSTM) networks and their implementation, we aim to provide a transparent and thorough understanding of the methodologies that underpin our analysis. This exposition not only serves to clarify the technical intricacies of our approach but also to underscore the robustness and reliability of the derived results.

### 2.1. Preprocessing

The foundational step in our analysis was the meticulous preprocessing of a comprehensive traffic dataset. Our database used is a publicly available computer traffic set from Stanford University [10]. This set comprises of 8 different servers with over 500,000 rows of information regarding them. The data provides daily traffic metrics, was initially subjected to a thorough cleansing process. Key to this phase was the conversion of date entries into a standardized chronological format, facilitating temporal analyses. Focus was particularly directed towards the total traffic variable, representing daily traffic volumes, which was extracted for subsequent processing. Recognizing the sensitivity of neural networks to data scale, we normalized these traffic volume figures using min-max scaling:

$$x_{norm} = \frac{x - x_{min}}{x_{max} - x_{min}} \quad (1)$$

### 2.2. LSTM Overview

Long Short-Term Memory (LSTM) networks, an advanced variant of recurrent neural networks (RNNs), are specifically designed to

address the challenges of learning long-range temporal dependencies [11]. Traditional RNNs, while theoretically capable of handling such dependencies, often fall short in practice due to issues like vanishing or exploding gradients. LSTMs overcome these hurdles with their unique architecture, making them highly effective for timeseries analysis and forecasting.

**Core Components of LSTM Networks** At the heart of an LSTM network are its LSTM units, each comprising four key elements:

- **Forget Gate:** This gate determines which information should be discarded from the cell state. It takes the previous hidden state and the current input, passes them through a sigmoid function, and outputs a number between 0 and 1 for each number in the cell state. A value close to 1 indicates “keep this information,” while close to 0 signifies “discard this information.” [12]
- **Input Gate:** This component decides what new information is to be stored in the cell state. It involves two parts: a sigmoid layer which decides which values will be updated, and a tanh layer that creates a vector of new candidate values that could be added to the state [12].
- **Cell State:** The cell state is the key to LSTMs’ ability to retain long-term dependencies. It runs straight down the entire chain of the network, with only minor linear interactions. This design allows information to flow unaltered and mitigates the risk of vanishing gradients [12].
- **Output Gate:** Finally, the output gate determines what the next hidden state should be. The hidden state contains information about previous inputs, and is used for predictions. The sigmoid layer decides which parts of the cell state to output, and then a tanh layer creates a vector of all the cell state values, which is multiplied by the sigmoid output, producing the final output of the LSTM unit [12].

#### 2.2.1. LSTM in the Context of Traffic Forecasting::

In our study, the LSTM’s ability to capture temporal dynamics is harnessed for predicting traffic volumes. Traffic data, inherently sequential and time-dependent, presents an ideal case for applying LSTM networks [2]. By learning from past traffic patterns and their progression over time, the LSTM model can forecast future traffic trends with a high degree of accuracy. This predictive capability is particularly crucial for short-term forecasting, where understanding immediate trends is vital for effective traffic management and planning.

#### 2.3. Data-Reshaping for LSTM

A crucial step in our implementation process was the preparation of the traffic volume data to make it suitable for LSTM processing. LSTM networks require the input data to be in a specific format, typically a 3-dimensional array. This format is essential because LSTMs are designed to process data in sequences and need to understand the order and context of the input data. The three dimensions required for LSTM input are:

- **Samples:** Each sample represents an independent instance from the dataset. In our case, each sample corresponded to a specific day’s data.

- **Time Steps:** This dimension represents the number of time intervals we consider for each sample. In our implementation, we used the look back parameter, set to 1, indicating that the model uses the traffic data from one previous time step (i.e., the previous day) to make a prediction for the current time step.
- **Features:** This dimension corresponds to the number of attributes or variables used for each time step. In our traffic dataset, this involved the normalized traffic volume data.

#### 2.4. Our LSTM Implementation

In our research, the utilization of Long Short-Term Memory (LSTM) networks was a deliberate choice, aimed at leveraging their renowned capability for modeling time-series data, particularly in capturing temporal dependencies and patterns inherent in traffic volume data. To explore the full potential of LSTM networks in this context, we employed two distinct architectures: a multi-layer LSTM and a single-layer LSTM model. This dual-model approach was instrumental in comprehensively assessing the advantages and limitations of varying LSTM complexities in traffic forecasting.

The multi-layer LSTM model, characterized by its layered structure of LSTM units, was designed to capture more complex and nuanced patterns in the data. This model consisted of two LSTM layers: the first with 30 units and the second with 10 units. The rationale behind this specific architecture was to enable the model to learn higher-level temporal features in the first layer and then refine and distill these features in the subsequent layer, thus potentially enhancing the accuracy of the predictions [13]. The multi-layer approach was hypothesized to be particularly adept at handling the intricate temporal relationships and potential nonlinearities present in traffic data.

In contrast, the single-layer LSTM model, with its singular LSTM layer of 30 units, served as a comparative baseline. This simpler model was intended to provide a benchmark against which the performance of the more complex multilayer model could be evaluated. The choice of 30 units for this model was a balance between computational efficiency and the model's capacity to capture significant temporal dependencies in the data.

For both models, the look back parameter was set to 1, indicating that each prediction was based on the data from the immediately preceding day. This parameter choice was driven by our focus on short-term forecasting, aiming to understand and predict day-to-day fluctuations in traffic volumes. The models were also configured to output a single value, representing the predicted traffic volume for the next day. Additionally, We compiled the multi-layer and single-layer LSTM models using the mean squared error (MSE) as the loss function, a common choice for regression problems. The Adam optimizer was selected for its efficiency in handling sparse gradients and adaptive learning rate adjustments, which are crucial for managing time-series data. The optimizer's role was pivotal in iteratively updating the network weights based on the training data, aiming to minimize the loss function throughout the training process.

The utilization of both a multi-layer and a single-layer LSTM model provided us with a nuanced understanding of how different LSTM architectures influence forecasting accuracy in the context of traffic

data. This approach allowed us to not only assess the effectiveness of LSTM networks in traffic volume prediction but also to explore the trade-offs between model complexity and predictive performance. By comparing the outcomes of these two models, we aimed to derive insights that could inform the optimal use of LSTM networks in similar time-series forecasting tasks, particularly those involving daily data with significant short-term temporal dependencies.

#### 2.5. Training and Data Splitting

The training of our LSTM models was executed with a meticulous strategy, tailored to optimize their performance for short-term traffic forecasting. This process involved training the models over 100 epochs with a batch size of 1. We intentionally opted for a small batch size, as it allows for more frequent updates to the model weights, a technique that can be particularly advantageous in the context of time-series data. Frequent updates enable the model to adjust more dynamically to the nuances and variations in the data, thus enhancing its predictive accuracy.

A key aspect of our training regimen was the implementation of a training-testing split in the dataset. 80% of our data was used for testing while the remaining 20% was tested on. This split was crucial for evaluating the models' performance on data that they had not encountered during the training phase. We allocated a significant portion of our dataset for training, while reserving a smaller, yet adequate, portion for testing. This division ensured that the models were exposed to a comprehensive range of data scenarios during training, while still preserving a representative sample for unbiased evaluation during the testing phase.

Incorporated into our training strategy was the early stopping mechanism, a powerful tool in combating overfitting—a common challenge in machine learning where a model becomes overly attuned to the training data and performs poorly on new, unseen data. The early stopping callback was configured to monitor the training loss, ceasing the training process if no improvement in this metric was observed for a consecutive span of 10 epochs. This approach not only helped in conserving computational resources but also played a pivotal role in ensuring that the models preserved their ability to generalize to new data. The objective was to find an optimal balance between underfitting and overfitting, thereby achieving the best possible model performance on both the training and testing datasets.

During the training phase, a critical focus was on the learning process of the LSTM units, particularly on their ability to utilize their inherent gates—forget, input, and output. These gates are instrumental in the LSTM's capability to process and retain relevant information while discarding what is deemed irrelevant. The effective utilization of these gates is what empowers LSTMs to excel in modeling time-series data, such as our traffic volume predictions. It is this sophisticated mechanism of information processing and retention that enables LSTMs to capture and learn from the temporal dependencies inherent in sequential data, a characteristic pivotal to their success in our traffic forecasting task.

## 3. RESULTS

	Average MAE	Average MSE	Average RMSE	Overall Average Accuracy
Multi-Layer LSTM	0.1005286	0.02618802	0.1549513	89.5%
Single-Layer LSTM	0.1145322	0.0426393	0.1921245	88.55%

**Table 1.** Results of Both LSTM Models

As shown in [Table 1](#), for performance evaluation, a four-pronged approach was adopted, involving Mean Absolute Error (MAE), Mean Squared Error (MSE), and Root Mean Squared Error (RMSE). These metrics, central to understanding the models' accuracy, are defined as follows:

$$MAE = \frac{1}{n} \sum_{i=1}^n |y_i - \hat{y}_i| \quad (2)$$

$$MSE = \frac{1}{n} \sum_{i=1}^n (y_i - \hat{y}_i)^2 \quad (3)$$

$$RMSE = \sqrt{\frac{1}{n} \sum_{i=1}^n (y_i - \hat{y}_i)^2} \quad (4)$$

$$\text{OverallActualAccuracy} = (1 - MAE) * 100 \quad (5)$$

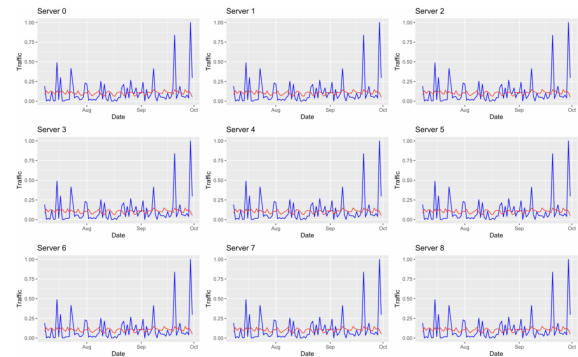
Building upon our established framework for performance evaluation, the outcomes of our LSTM models were thoroughly examined through Mean Absolute Error (MAE), Mean Squared Error (MSE), Root Mean Squared Error (RMSE), and Overall Actual Accuracy. These metrics collectively offered a comprehensive view of the models' predictive capabilities.

### 3.1. Multi-layer Performance

The performance of the Multi-Layer LSTM model was notably promising. The model achieved an average MAE of 0.1005286, indicating that the predictions were, on average, approximately 10.05% off from the actual traffic volumes. This degree of accuracy is particularly significant in the realm of traffic forecasting, where precision can have substantial implications. The predicted vs actual network flow is depicted in [Figure 1](#) where the predicted values seem to stay primarily around the same area. As the prediction is heavily based on the previous value (look back = 1) the model struggled with the predicting peaks.

In terms of MSE, the model exhibited a value of 0.02618802. This figure suggests a consistent performance across predictions with minimal occurrences of extreme errors. The RMSE, standing at 0.1549513, further substantiates the model's accuracy, offering a realistic measure of the error magnitude in the same units as the predicted variable.

A key highlight was the model's Overall Actual Accuracy, which was calculated to be approximately 89.5%. This high level of accuracy underscores the model's effectiveness in capturing the complex temporal patterns within the traffic data, affirming its suitability for short-term forecasting applications.

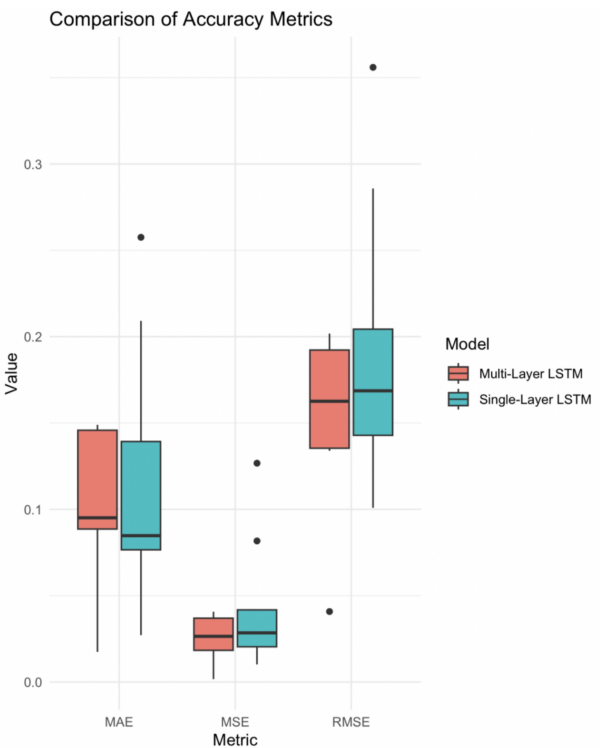
**Figure 1.** Predicted Network Traffic (Red) vs Actual Network Traffic (Blue)

### 3.2. Comparative Analysis

Contrasting these results, the Single-Layer LSTM model, with its simpler architecture, yielded slightly different outcomes. The model recorded an average MAE of 0.1145322, suggesting a deviation of about 11.45% from the actual values. Though marginally higher than the Multi-Layer model, this still signifies a commendable level of accuracy.

The MSE and RMSE values for the Single-Layer model were 0.0426393 and 0.1921245, respectively. These metrics, being higher than those of the Multi-Layer LSTM, point to a greater variance in the predictions and a larger error magnitude. This variance is depicted in [Figure 2](#). The model's Overall Actual Accuracy stood at 88.55%, slightly lower than that highlights the enhanced capability of the multi-layer architecture in handling complex time-series data like traffic volumes.

### 3.3. Statistical Significance

**Figure 2.** Box Plots of Accuracy Metrics Comparing Single & Multi-Layer LSTM Models

The approximately 1.5% increase in accuracy from the single-layer to the multi-layer LSTM model, though seemingly modest, is statistically significant and carries practical implications for network traffic management. This improvement is particularly notable given the complexity and variability of network traffic data, where even slight enhancements can lead to substantial benefits in operational efficiency and service quality.

Statistically, the increase in accuracy indicates a more reliable model that is better at capturing the non-linear and dynamic patterns of network traffic. This is crucial for applications where forecasts directly influence real-time decisions, such as dynamic bandwidth allocation and predictive maintenance. In such contexts, even a small percentage improvement can translate into significant operational advantages, such as reduced downtime and optimized resource allocation.

Moreover, from a statistical perspective, the consistency of improved performance across multiple metrics (MAE, MSE, RMSE) suggests that the multi-layer LSTM is not only occasionally outperforming the single-layer model by chance but is systematically more effective. This consistency reinforces the argument for the robustness of the multi-layer architecture in handling complex datasets typical of network environments.

## 4. DISCUSSION

This research aimed to explore the efficacy of Long Short-Term Memory (LSTM) networks in the context of network traffic volume forecasting, a domain where accurate predictions can significantly impact the Cyber-Space. Our investigation was grounded in the application of two LSTM architectures - a Multi-Layer LSTM and a Single-Layer LSTM - each offering different levels of complexity and potential for capturing temporal dependencies in the data.

### 4.1. LSTM Model Performance

The Multi-Layer LSTM model's superior performance, as evidenced by its lower MAE, MSE, and RMSE, and higher overall accuracy, underscores the value of complex neural network architectures in handling intricate patterns in time-series data. The additional layers in this model provided a more nuanced understanding of the temporal sequence, enabling it to capture subtleties in traffic trends that a simpler model might overlook. This finding aligns with existing literature, which suggests that deeper neural network architectures often yield better results in complex data scenarios, albeit at the cost of increased computational resources and potential risks of overfitting [13].

Conversely, the Single-Layer LSTM model, while not outperforming the Multi-Layer LSTM, demonstrated respectable accuracy, highlighting its utility as a more straightforward and computationally efficient alternative. This model's slightly higher error metrics could be attributed to its limited capacity to model complex temporal relationships, a trade-off that comes with reduced model complexity.

### 4.2. Implications for Traffic Forecasting

The application of Long Short-Term Memory (LSTM) models for network data volume forecasting, as explored in our study, carries

profound implications for network data management and planning. The ability of LSTM models to accurately predict network traffic volumes is particularly crucial in the current era, where the efficient handling of data is integral to network operations.

The enhanced predictive capabilities of LSTM models, as evidenced by their performance in our study, mark a significant advancement in network data forecasting. These models, adept at capturing complex temporal dependencies, allow for a more accurate anticipation of network loads. This is especially relevant given the current landscape of rapid data generation and consumption. Accurate forecasting enables network administrators to proactively manage network resources, allocate bandwidth efficiently, and optimize overall network performance. This proactive approach to network management is invaluable, especially in preventing congestion during peak traffic periods and maintaining high-quality service for users.

Furthermore, the insights gained from LSTM-based forecasting facilitate strategic network planning and informed decision-making. Network operators and service providers can leverage this data to plan infrastructure expansions and technology upgrades, ensuring that networks are equipped to handle future data demands. This strategic foresight aids in aligning network capabilities with projected requirements, thereby enhancing network efficiency and reducing the risk of over or under-provisioning network resources.

Cost efficiency and operational sustainability are additional benefits that stem from improved network data forecasting. By accurately aligning network capacity with actual data demands, network operators can avoid unnecessary expenditures on infrastructure while still satisfying user needs. Additionally, more precise data forecasting contributes to sustainability by optimizing the use of energy resources within network operations [6].

The study's findings also have significant implications for managing the complexities introduced by emerging technologies such as IoT, cloud computing, and 5G networks. These technologies, characterized by their high data throughput and diverse traffic patterns, present new challenges in network management. The ability of LSTM models to process and forecast large volumes of complex data makes them particularly well-suited for navigating these challenges. Accurate forecasting of data traffic from a myriad of devices and services underscores the potential of LSTM models in ensuring the efficient integration and management of these emerging technologies within network infrastructures.

### 4.3. Considerations for Model Selection

In choosing between a Multi-Layer and Single-Layer LSTM model, one must consider factors beyond just predictive accuracy. The complexity of a multi-layer model, for instance, necessitates greater computational resources and may pose challenges in terms of training time and model interpretability. Additionally, issues with resource efficiencies can arise. Multi-layer LSTMs, due to their complexity, require more computational resources, including processing power and memory. This can lead to increased operational costs and longer training times, which may not be feasible for all organizations or in scenarios where rapid deployment of models is necessary. Furthermore, the complexity of multi-layer LSTMs also poses a higher risk of overfitting, especially when the

available data is limited or the feature space is not sufficiently diverse. Overfitting occurs when a model learns the details and noise in the training data to an extent that it negatively impacts the performance of the model on new data. This makes multi-layer LSTMs less suitable for smaller datasets or less complex problem domains where a simpler model could generalize better. On the other hand, a single-layer model, while less computationally demanding, might not adequately capture the complexity of certain datasets.

#### 4.4. Future Direction

Building upon the insights gained from our study on LSTM models for network traffic forecasting, several promising avenues emerge for future research in this domain. These directions aim to expand the scope and efficacy of forecasting models, catering to the evolving needs of network management and optimization.

The integration of additional data sources stands as a critical area for enhancement. By incorporating diverse data sets, such as network usage during special events, cybersecurity incident data, and user behavior patterns, future models can gain a more holistic understanding of network dynamics. This comprehensive approach could significantly improve the accuracy of traffic predictions and offer a nuanced understanding of various factors influencing network load.

Advancements in model architecture also present exciting possibilities. Experimenting with hybrid models that combine the temporal learning capabilities of LSTMs with spatial analysis techniques could yield more sophisticated forecasting tools. For instance, integrating LSTMs with CNNs or graph neural network might provide a deeper insight into both the temporal and spatial aspects of network traffic. Fine-tuning LSTM configurations, exploring different layer structures, and adapting the models to specific network types are key areas that could lead to more optimized and effective forecasting solutions.

The development of real-time forecasting capabilities is another critical frontier. Models that can offer accurate predictions in near real-time would be invaluable for dynamic network management, allowing for rapid responses to emerging traffic patterns and potential network issues. Such capabilities would significantly enhance the responsiveness and adaptability of network operations.

Additionally, the scalability and generalizability of LSTM models across various network architectures warrant further exploration. Testing these models in diverse network environments, such as cloud networks, IoT infrastructures, and 5G networks, would provide insights into their versatility and applicability. This research could help ascertain the models' effectiveness across different settings and identify any necessary adaptations or optimizations.

Finally, the practical application of LSTM-based forecasting models in real-world network management systems is a crucial step towards their widespread adoption. Integrating these models into existing network infrastructure and evaluating their performance in live environments would not only validate their practical utility but also highlight areas for improvement in real-time network traffic management.

## 5. CONCLUSIONS

This study has successfully demonstrated the potential of LSTM networks in the realm of network traffic forecasting, a critical component in the efficient management of modern digital networks. By employing and comparing both multi-layer and single-layer LSTM models, our research has shed light on the capabilities and limitations of these models in handling the complex task of predicting network traffic volumes. The findings from this investigation underscore the effectiveness of LSTM models in capturing intricate temporal dependencies inherent in network data, thus offering a significant contribution to the field of network data management.

Our research confirms that LSTM models, particularly those with multiple layers, can provide a high degree of accuracy in forecasting network traffic. This accuracy is crucial for network operators to proactively manage network resources, ensuring optimal performance and quality of service. The study also highlights the importance of careful data preprocessing and the selection of appropriate model parameters in enhancing the performance of LSTM models. Moreover, the comparative analysis of different LSTM architectures provides valuable insights for researchers and practitioners in choosing the right model based on the specific requirements and constraints of their network environment.

If given the opportunity to further advance this research, several enhancements could be pursued. First, integrating additional types of data, such as real-time traffic updates, weather conditions, and special event schedules, could refine the models' predictive capabilities. This would allow for a more comprehensive understanding of the factors influencing network traffic and could lead to even more robust forecasting models. Additionally, exploring the application of hybrid models that combine the strengths of LSTM with other advanced machine learning techniques like convolutional neural networks or graph neural networks could address some of the limitations observed in traditional LSTM models. These hybrid models could potentially offer a deeper insight into both the temporal and spatial aspects of network traffic.

Moreover, developing real-time forecasting capabilities would be a significant step forward. This would not only enhance the responsiveness of network management systems but also allow for more dynamic adjustments to network operations, ensuring high efficiency and user satisfaction. Implementing these models in a simulated environment to test their real-world applicability and performance before full-scale deployment could mitigate risks and refine the models' effectiveness.

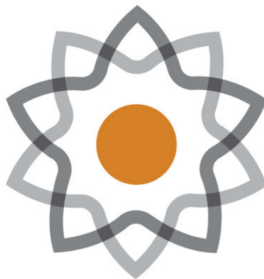
Looking forward, the application of LSTM models in network traffic forecasting opens up exciting possibilities for the development of more intelligent, efficient, and adaptive network management systems. The integration of LSTM-based forecasting models into real-world network operations could mark a significant step towards more proactive and data-driven network management. As the digital landscape continues to evolve, with increasing data traffic and the integration of emerging technologies, the role of accurate and reliable traffic forecasting will become ever more critical.

The author thanks Mr. Robert Gotwals for assistance with this work. Appreciation is also extended to Chiara Sabatti of Stanford

University for creating the publicly available dataset used in this project.

## REFERENCES

- [1] S. Nihale, S. Sharma, L. Parashar, and U. Singh, "Network Traffic Prediction Using Long Short-Term Memory," in *2020 International Conference on Electronics and Sustainable Communication Systems (ICESC)*, 2020, pp. 338–343. doi: [10.1109/ICESC48915.2020.9156045](https://doi.org/10.1109/ICESC48915.2020.9156045).
- [2] A. Khodadadi, "Traffic Forecasting Using Graph Neural Networks and LSTM." [Online]. Available: [https://keras.io/examples/timeseries/timeseries\\_traffic\\_forecasting/](https://keras.io/examples/timeseries/timeseries_traffic_forecasting/)
- [3] V. Kramar and V. Alchakov, "Time-Series Forecasting of Seasonal Data Using Machine Learning Methods," *Algorithms*, vol. 16, no. 5, p. 248–249, 2023, doi: [10.3390/a16050248](https://doi.org/10.3390/a16050248).
- [4] I. Lohrasbinasab, A. Shahroki, A. Taherkordi, and A. Delia Jurcut, "From statistical to machine learningbased network traffic prediction," *Transactions on Emerging Telecommunications Technologies*, vol. 33, no. 4, p. e4394, 2022, doi: [10.1002/ett.4394](https://doi.org/10.1002/ett.4394).
- [5] W. Jiang and J. Luo, "Graph neural network for traffic forecasting: A survey," *Expert Systems with Applications*, vol. 207, p. 117921–117922, 2022, doi: [10.1016/j.eswa.2022.117921](https://doi.org/10.1016/j.eswa.2022.117921).
- [6] K. Zhang, X. Zhao, X. Li, X. You, and Y. Zhu, "Network Traffic Prediction via Deep Graph-Sequence Spatiotemporal Modeling Based on Mobile Virtual Reality Technology," *Wireless Communications and Mobile Computing*, vol. 2021, pp. 1–12, 2021, doi: [10.1155/2021/2353875](https://doi.org/10.1155/2021/2353875).
- [7] J. Liu, N. Wu, Y. Qiao, and Z. Li, "A scientometric review of research on traffic forecasting in transportation," *IET Intelligent Transport Systems*, vol. 15, no. 1, pp. 1–16, 2021, doi: [10.1049/itr2.12024](https://doi.org/10.1049/itr2.12024).
- [8] A. Mozo, B. Ordozgoiti, and S. Gómez-Canaval, "Forecasting short-term data center network traffic load with convolutional neural networks," *PLOS ONE*, vol. 13, no. 2, p. e191939, 2018, doi: [10.1371/journal.pone.0191939](https://doi.org/10.1371/journal.pone.0191939).
- [9] E. Haugsdal, S. Malacarne, and M. Ruocco, "Circle Attention: Forecasting Network Traffic by Learning Interpretable Spatial Relationships from Intersecting Circles," in *Machine Learning and Knowledge Discovery in Databases: Applied Data Science and Demo Track*, vol. 14175, G. De Francisci Morales, C. Perlich, N. Ruchansky, N. Kourtellis, E. Baralis, and F. Bonchi, Eds., Cham: Springer Nature Switzerland, 2023, pp. 106–121. doi: [10.1007/978-3-031-43430-3\\_7](https://doi.org/10.1007/978-3-031-43430-3_7).
- [10] C. Sabatti, "Computer Network Traffic Data." [Online]. Available: <https://chiarasabatti.su.domains/data.html>
- [11] S. Hochreiter and J. Schmidhuber, "Long Short-Term Memory," *Neural Computation*, vol. 9, no. 8, pp. 1735–1780, 1997, doi: [10.1162/neco.1997.9.8.1735](https://doi.org/10.1162/neco.1997.9.8.1735).
- [12] F. Gers, "Learning to forget: continual prediction with LSTM," in *9th International Conference on Artificial Neural Networks: ICANN '99*, 1999, pp. 850–855. doi: [10.1049/cp:19991218](https://doi.org/10.1049/cp:19991218).
- [13] H. N. Bhandari, B. Rimal, N. R. Pokhrel, R. Rimal, K. R. Dahal, and R. K. Khatri, "Predicting stock market index using LSTM," *Machine Learning with Applications*, vol. 9, p. 100320–100321, 2022, doi: [10.1016/j.mlwa.2022.100320](https://doi.org/10.1016/j.mlwa.2022.100320).



# The Morganton Scientific

*North Carolina  
School of Science and  
Mathematics*

Journal of Student STEM Research

## AQINet: A multimodal deep convolutional neural network to predict Air Quality Index via satellite imagery and meteorological data

Zoaib Sihorwala<sup>1</sup> 

<sup>1</sup>North Carolina School of Science and Mathematics 

### Abstract

Air pollution is a pressing ecological issue with significant impacts on both public health and the environment. Poor air quality is a major contributor to respiratory diseases and is linked to millions of deaths annually, but many countries cannot afford air monitoring equipment. This lack of data makes it difficult to assess the health and environmental risks resulting from pollutant exposure. To address this problem, we present a multimodal model to inexpensively predict air quality levels in densely populated areas. Our research leverages both satellite imagery and meteorological data to create accurate air quality predictions. We sourced urban and suburban satellite imagery from the National Agriculture Imaging Program, meteorological data from Open-Meteo, and air quality data from OpenWeatherMap, to create a dataset named AQISet. AQISet is publicly available and free to download. The goal was for the model to implicitly learn spatial features in each image, such as roads, greenery, and bodies of water, and then combine this info with meteorological data to predict AQI. Using multiple computer vision techniques, the model was able to predict AQI with a mean absolute error of 16 AQI and a classification accuracy of 77% based on the EPA's AQI standards categories. Our results establish a baseline for AQI prediction from satellite imagery and are a vast improvement over state-of-the-art pre-trained general computer vision models.

**Keywords** Air Quality Index (AQI), Satellite Imagery, Deep Learning

### 1. INTRODUCTION

The process of respiration is essential for all living organisms, as it enables them to produce energy. Consequently, access to clean air is fundamental for life to be sustained. Exposure to air pollution can lead to a multitude of health issues such as respiratory ailments, cardiovascular diseases, and in severe cases, death [1].

Despite concerted global efforts to mitigate air pollution in recent decades, a startling statistic from 2019 shows that 99% of the world's population resides in areas that fail to meet the World Health Organization's air quality standards [2]. This alarming situation has led to over 4 million deaths annually, predominantly in low and middle-income countries, which account for 89% of these fatalities linked to ambient air pollution.

Air Quality Index (AQI), a metric of air pollution developed by the United States Environmental Protection Agency (EPA), quantifies air pollution levels [3]. AQI is computed based on measurements of several pollutants, chiefly particulate matter ( $PM_{2.5}$  and  $PM_{10}$ ), nitrogen dioxide ( $NO_2$ ), ozone ( $O_3$ ), carbon monoxide (CO), and sulfur dioxide ( $SO_2$ ). These pollutants arise from a variety of sources such as man-made emissions from fossil fuels, as well as natural sources like smoke from volcanoes and wildfires.

Ground-based air quality monitors are typically used to measure the concentration of each pollutant over a certain time frame. These devices vary in size, from small household units to medium and large static monitors strategically positioned around cities, offering continuous data from selected urban locations. These types of sensors utilize active measurement techniques, which use physical or chemical methods to analyze the air in a given area automatically. These sensors can be extremely expensive to manufacture and operate, and costs can range from 15,000 dollars to 40,000 dollars per sensor [4]. This

Published Jun 27, 2024

Correspondence to  
Zoaib Sihorwala  
sihorwala24z@ncssm.edu

Open Access 

Copyright © 2024 Sihorwala. This is an open-access article distributed under the terms of the Creative Commons Attribution 4.0 International license, which enables reusers to distribute, remix, adapt, and build upon the material in any medium or format, so long as attribution is given to the creator.

 Published by Curvenote

Pollutant	Health Risks
Particulate Matter	Irritation of airways, aggravated asthma, and lung cancer.
NO <sub>2</sub>	Inflammation of airways, worsened cough reduced lung function, and increased asthma attacks.
O <sub>3</sub>	Chest pain, coughing, throat irritation, and congestion.
CO	Headache, nausea, rapid breathing, dizziness, and confusion.
SO <sub>2</sub>	Irritation of eyes, nose, throat, and airways, and aggravation of asthma and emphysema.

**Table 1.** Health Risks of Air Pollutants

high cost poses a considerable challenge to lesser developed regions of the world where governments may struggle to afford many air quality monitors to monitor urban and suburban areas adequately. According to the United Nations International Children's Emergency Fund (UNICEF), only about 6% and 24% of children live within 50km of an air quality monitor in Africa and South America respectively [5]. The lack of AQI data in developing countries can lead to unnecessary pollutant exposure and affect regulatory processes, as authorities struggle to assess pollution levels and take appropriate actions.

## 2. PREVIOUS WORK

Other scientists have conducted experiments using satellite data to predict air pollution levels in certain areas. Scheibenreif et al. used imagery and remote sensing measurements from the European Space Agency's Sentinel satellites and a two-stream deep neural network to predict levels of nitrogen dioxide, one of the major pollutants in computing the AQI [6]. Rowley et. al built off of this approach and used the Sentinel satellites along with NO<sub>2</sub> ground monitoring stations to predict levels of NO<sub>2</sub>, O<sub>3</sub>, and PM<sub>10</sub> [7]. They also included a fully connected neural network that utilized additional data such as population and altitude. This project aims to provide a more general prediction of air quality by directly predicting the AQI rather than the pollutants that comprise it.

## 3. DATASET CREATION

At the time this research was conducted, there were no publicly available datasets that included satellite imagery with time, location, AQI, and meteorological data. To train our model, we compiled our own dataset, AQISet, by retrieving data from different sources [8]. We started by collecting the most inflexible of the three, satellite imagery. Since 2002, the US Department of Agriculture has operated the National Agriculture Imagery Program (NAIP), which collects high-resolution imagery across the United States from urban and suburban regions [9]. This data is accessible through Google Earth Engine, a geospatial analysis program that allows users to write Python code to export imagery [10]. We gathered longitude and latitude data for the 100 largest cities in America and then wrote a script to collect 100 1km by 1km images from each city, each with

**Figure 1.** A sample satellite image in AQISet.

1m per pixel resolution. We utilized 25 parallel processes to export all of the imagery. Since the NAIP dataset did not have complete coverage of all the areas we targeted, only 7,621 images were gathered out of an attempted 10,000, but this amount was still suitable for our dataset and model. A sample image is below:

Alongside the imagery, we also collected the time and location of capture for each image so that we could use the timestamp and coordinates of the images to pair them up with AQI and meteorological data. The air quality data was retrieved from OpenWeatherMap, a service that provides global weather and environmental data via API calls. [11]. However, OpenWeatherMap provides pollutant concentrations rather than directly providing AQI values, so we converted the concentrations to AQI in the data preprocessing. The first step was to convert the units of each pollutant from  $\mu\text{g}/\text{m}^3$  to ppb [12]. The equation is as follows:

$$MAE = \frac{\mu\text{g}/\text{m}^3}{12.187M} + (273.15 + C) \quad (1)$$

Where M is the molecular weight of the pollutant and C is the surface temperature in  $^\circ\text{C}$ . Then, we converted these concentrations to an AQI value using an equation and a table of breakpoints provided by the EPA [13]. The equation is as follows [14]:

$$AQI = \frac{I_{hi} - I_{lo}}{C_{hi} - C_{lo}}(C - C_{lo}) + I_{lo} \quad (2)$$

Where C is the pollutant concentration, Chi is the concentration breakpoint greater than or equal to C, Clo is the breakpoint less than or equal to C, and Chi and Clo are the corresponding AQI breakpoints of Chi and Clo respectively.

Finally, the overall AQI is simply the maximum AQI calculated for each pollutant. These AQI values were paired with each image based on time and location. For our meteorological data, we collected four different factors: wind speed, humidity, temperature, and rain. Rain was further split up into 3 categories, a sum of precipitation over 24 hours, 8 hours, and 1 hour. A table of their respective effects on AQI is below.

Weather Factor	Effects on AQI
Rain	Rain can wash away particulate matter, cleansing the air.
Temperature	Higher temperatures accelerate photochemical reactions, resulting in more ground level O <sub>3</sub>
Humidity	Water vapor can serve as nuclei for small particles, which can result in the formation of larger particulates.
Wind Speed	Higher wind speeds can disperse pollutants by blowing them away.

**Table 2.** Effects of Meteorological Factors on AQI

This data was retrieved via API calls to Open-Meteo [15], a meteorological data service, and then paired up with each image in a similar manner to the AQI data.

## 4. MATERIALS

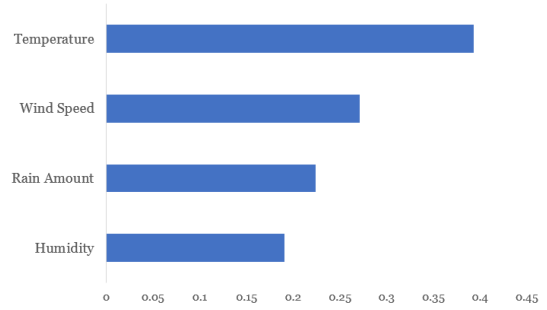
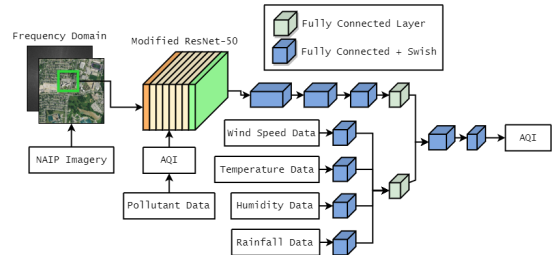
The model was built in Python 3.11.4 using the PyTorch library for machine learning. All of the data was processed using the Pandas library. Smaller testing of the model (less than 5 epochs) was conducted on Michigan State University's (MSU) CVLab GPU server, using 4 Titan V GPUs. Larger tests were run using an NVIDIA V100 Tensor Core GPU from MSU's High Power Computing Center with the UNIX command-line interface. The model uses a learning rate of 0.001 and a batch size of 64 images.

## 5. METHODS

Our model is split into two parts: the image network and the tabular network. The basis of our image network is ResNet-50, a 50-layer convolutional neural network pre-trained for image classification tasks [16]. Although our problem is fundamentally that of regression, the main goal of the image network is to implicitly learn certain features of an image to produce an accurate prediction such as the amount of greenery, roads, cars, buildings, and bodies of water present. These can all affect the overall AQI of an area, and it is crucial to use a deep network so that it is able to learn these complex features in the image. We modified ResNet-50 to include an extra channel of input (which will be discussed later) and increased its initial convolution kernel size from 7x7 to 8x8 to help the model capture broader areas of information from the image while decreasing computational complexity. The output from the modified ResNet-50 is then passed through three fully connected layers with Swish activation. We chose to use Swish over other popular activation functions such as Rectified Linear Unit (ReLU) due to Swish's non-linearity, which allows the model to learn complex relationships between inputs and outputs.

The tabular network is a multilayer perceptron that takes the amount of rain, humidity, temperature, and wind speed as input. These four factors were selected due to their direct effect on and strong correlation with AQI.

The outputs from the image network and the tabular data network are then combined, passed through a few more layers - again with

**Figure 2.** R<sup>2</sup> values of various meteorological factors and AQI.**Figure 3.** AQINet model architecture.

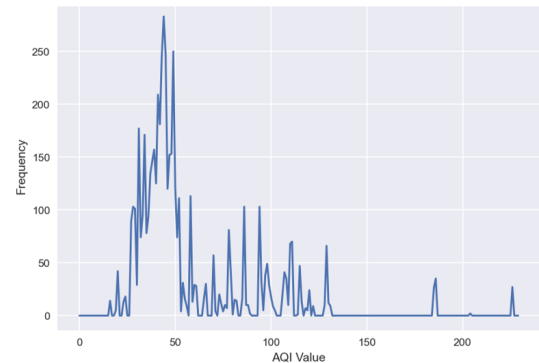
Swish activation - and are eventually narrowed down to a layer with one neuron which holds the AQI prediction.

In the model above, the larger the block, the greater the amount of neurons in the layer. The blocks decrease in size, effectively narrowing down the data passed through each layer until there is a single neuron left.

Before we trained and tested the AQINet model, we had to resolve a major issue stemming from our dataset: AQI imbalance. AQI values are not evenly distributed in the real world, and this is reflected in our dataset as seen below.

The majority of the AQI values range from 25 to 50 AQI, and this imbalance will lead our model to simply predict from the small range of AQI values that are the most frequent. Consequently, the model will be rewarded for a majority of its predictions, and will not learn. There are two methods we took to approach this.

The first method is using upsampling to even out the AQI distribution by taking more samples of images with infrequent AQIs. Instead of feeding our model the entire 1000px by 1000px image, we take N 224x224 patches from the image. N is proportional to the

**Figure 4.** AQI value frequencies in AQISet.

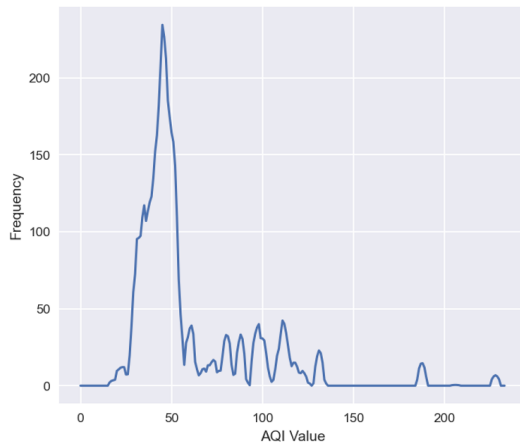


**Figure 5.** The smoothed AQI frequency distribution.

inverse of our frequency graph so that images with infrequent AQI are sampled much more than those with common AQI, effectively evening out AQI distribution in our data.

The second method we use is a weighted loss function to punish the model more for incorrect guesses on infrequent AQI. We started with a standard Mean Squared Error (MSE) loss, the square of the difference between the model's prediction and the ground truth AQI. Then, we computed some weight for each AQI,  $W$ , to scale our MSE loss by.  $W$  is defined as follows:

$$W_i = (N(\mu, \sigma^2) * F(A_i))^{-1} \quad (3)$$

Where  $N$  is a Gaussian kernel with  $\mu$  mean frequency and  $\sigma^2$  variance,  $F$  is our frequency distribution, and  $A_i$  is the ground truth AQI for patch  $i$ . The asterisk (\*) in the equation represents a convolution, rather than multiplication. This convolution serves to smooth our frequency distribution so that our weights are calculated based on large changes in the frequency rather than small inconsistencies. This is illustrated in the graph below.

After computing this weight, the total loss for an image with  $n$  patches is simply the sum of the weights multiplied by MSE loss:

$$\text{Loss} = \frac{k}{n} \sum_{i=0}^n W_i (x_i - y_i)^2 \quad (4)$$

In this equation,  $k$  is a scalar applied to the function to prevent the loss from becoming very small since often  $W$  will be significantly less than 1. A very small loss will adversely affect the training of our model by diminishing the gradients and slowing down the learning. Together both the upsampling and weighted loss solve the issue of data imbalance, and allow the model to predict the full range of AQI values (0-500).

A minor issue with our dataset arises from the limited variance in AQI values at each location from which images were sourced. In each city, the proximity of image capture points—often just a few kilometers apart—resulted in numerous images from nearby areas exhibiting identical AQI values since the data would come from the same sensor. This presents a challenge for our model, as it could lead to overfitting, with the model erroneously predicting specific AQI values that frequently appear in the dataset. To address this, we

introduced a range of noise, varying from -5 to +5 AQI, to each patch taken from an image. We used a Gaussian noise distribution across all of the patches, ensuring that the mean AQI across the patches was equivalent to the original AQI. This noise introduction aims to improve our model's robustness, ensuring better generalization when it inevitably encounters new data in testing.

One discernible feature of poor air quality in images is the haziness or subtle blurring effect caused by dust and other airborne particulates. To capture this trait, we use a 2D Fourier transform to transform our RGB image input into the frequency domain, thereby adding a fourth channel to our image network. The frequency domain is particularly effective in highlighting the haziness of an image since it can reflect it in its low-frequency components. We first converted the RGB image to grayscale by averaging the values from the red, green, and blue input channels. Then, we normalize each pixel value to range from 0-1 rather than 0-255 to improve computational speed. We then treat the pixel values as a stream of numbers, or a signal. This signal is decomposed into sine and cosine waves using the Fast Fourier Transform (FFT). The resulting projected FFT image generally appears darker in areas representing low frequencies, indicative of smooth transitions over time, and brighter in areas with high frequencies, corresponding to finer details in the image. This transformed image is subsequently fed into the model for analysis. Below are a few examples of these transformations.

## 6. RESULTS

In testing, AQINet outperforms ResNet-50 in both Mean Absolute Error and classification accuracy. AQI - more than a 48% improvement. Classification accuracy was based on whether the model could place an image into its corresponding AQI category, based on the EPA's table of AQI categories [14].

## 7. CONCLUSION

This research represents a significant step forward in addressing the pressing issue of air pollution and its consequences for public health. By harnessing the power of satellite imagery and

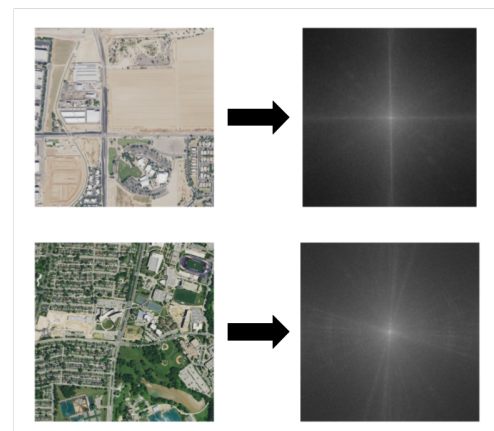


**Figure 6.** Imagery and their Fourier transforms. The top image contains haze, which results in a darker frequency domain. The AQI for the top image is 185, while the bottom image's AQI is 52.

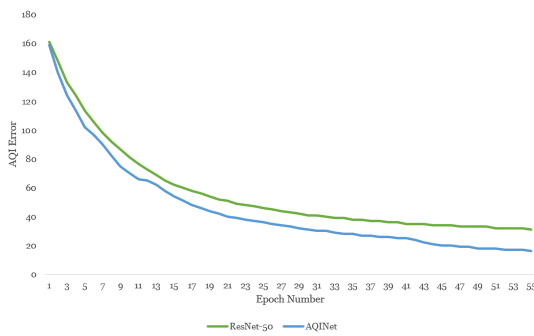


Figure 8. AQI MAE for ResNet-50 vs. AQINet.

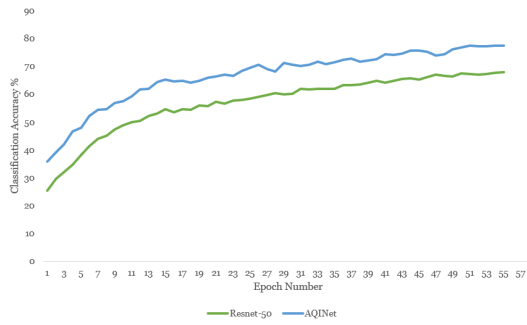


Figure 8. Classification Accuracy for ResNet-50 vs. AQINet.

meteorological data, the developed multimodal model, AQINet, offers an inexpensive solution for predicting air quality levels in developing areas. This model has shown impressive results, achieving a mean absolute error of 16 AQI (on a scale from 0-500) and a classification accuracy of 77%, based on the EPA's AQI standards categories.

The ability to predict AQI from satellite imagery has the potential to revolutionize air quality monitoring, especially in regions with limited access to expensive air quality sensors. This approach can provide a cost-effective means of obtaining widespread air quality data, offering substantial benefits for both researchers and policymakers.

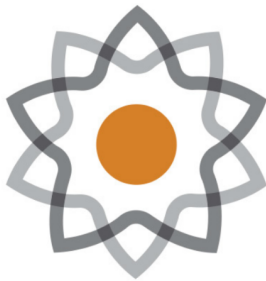
Alongside AQINet, we also presented AQISet, a dataset with over 7600 satellite images paired with their AQI and various meteorological data from the time and location of capture. This dataset can help future researchers continue to tackle the issues of air quality monitoring by developing their own models. AQISet is publicly available on GitHub [8].

Together, AQINet and AQISet provide a solid foundation for future endeavors in air quality prediction using remote sensing data. Further enhancements and refinements of the model could lead to even more accurate and robust predictions, ultimately contributing to the improvement of air quality and the well-being of communities around the world.

I would like to acknowledge Dr. Xiaoming Liu and Dr. Feng Liu for providing me with a great introduction to computer vision, as well as the rest of the CV Lab for their help during my research.

## REFERENCES

- [1] “Trends Report 2003.” [Online]. Available: [https://www.epa.gov/sites/default/files/2017-11/documents/trends\\_report\\_2003.pdf](https://www.epa.gov/sites/default/files/2017-11/documents/trends_report_2003.pdf)
- [2] “Ambient (outdoor) air pollution.” [Online]. Available: [https://www.who.int/news-room/fact-sheets/detail/ambient-\(outdoor\)-air-quality-and-health](https://www.who.int/news-room/fact-sheets/detail/ambient-(outdoor)-air-quality-and-health)
- [3] “AQI Basics | AirNow.gov.” [Online]. Available: <https://www.airnow.gov/aqi/aqi-basics>
- [4] “FRM/FEM and Air Sensors.” [Online]. Available: [https://www.epa.gov/sites/default/files/2019-12/documents/frm-fem\\_and\\_air\\_sensors\\_dec\\_2019\\_webinar\\_slides\\_508\\_compliant.pdf](https://www.epa.gov/sites/default/files/2019-12/documents/frm-fem_and_air_sensors_dec_2019_webinar_slides_508_compliant.pdf)
- [5] “Silent Suffocation in Africa: Air Pollution.” [Online]. Available: <https://www.unicef.org/media/55081/file/Silent%20suffocation%20in%20africa%20air%20pollution%202019%20.pdf>
- [6] L. Scheibenreif, M. Mommert, and D. Borth, “Toward Global Estimation of Ground-Level NO<sub>2</sub> Pollution With Deep Learning and Remote Sensing,” *IEEE Transactions on Geoscience and Remote Sensing*, vol. 60, pp. 1–14, 2022, doi: [10.1109/TGRS.2022.3160827](https://doi.org/10.1109/TGRS.2022.3160827).
- [7] A. Rowley and O. Karakus, “Predicting air quality via multimodal AI and satellite imagery,” 2022, doi: [10.48550/ARXIV.2211.00780](https://doi.org/10.48550/ARXIV.2211.00780).
- [8] Z. Sihorwala, “AQISet.” [Online]. Available: <https://github.com/zoaibs/AQISet>
- [9] “National Agriculture Imagery Program - NAIP Hub Site.” [Online]. Available: <https://naip-usdaonline.hub.arcgis.com/>
- [10] “Google Earth Engine.” [Online]. Available: <https://earthengine.google.com/>
- [11] “Current weather and forecast - OpenWeatherMap.” [Online]. Available: <https://openweathermap.org/>
- [12] “Danish National Environmental Research Institute.”
- [13] “Air quality index.” [Online]. Available: [https://en.wikipedia.org/w/index.php?title=Air\\_quality\\_index&oldid=1221043689](https://en.wikipedia.org/w/index.php?title=Air_quality_index&oldid=1221043689)
- [14] “AQI Technical Assistance Document.” [Online]. Available: <https://www.airnow.gov/sites/default/files/2020-05/aqi-technical-assistance-document-sept2018.pdf>
- [15] “Open-Meteo.” [Online]. Available: <https://open-meteo.com/>
- [16] K. He, X. Zhang, S. Ren, and J. Sun, “Deep Residual Learning for Image Recognition,” 2015, doi: [10.48550/ARXIV.1512.03385](https://doi.org/10.48550/ARXIV.1512.03385).



# An Analysis on Genomic Correlation for Gallstone Susceptibility

Sanjita Srinath<sup>1</sup>  

<sup>1</sup>North Carolina School of Science and Mathematics  

## The Morganton Scientific

North Carolina  
School of Science and  
Mathematics

Journal of Student STEM Research

Published Jun 27, 2024

Correspondence to  
Sanjita Srinath  
[srinath24s@ncssm.edu](mailto:srinath24s@ncssm.edu)

Open Access 

Copyright © 2024 Srinath. This is an open-access article distributed under the terms of the [Creative Commons Attribution 4.0 International license](#), which enables reusers to distribute, remix, adapt, and build upon the material in any medium or format, so long as attribution is given to the creator.

### Abstract

Gallstones, typically benign and harmless hardened deposits of digestive fluids, present in the gallbladder can cause severe painful complications if left untreated and can lead to removal surgery. [1] Quantitative Trait Loci (QTL) analysis can be used to find potential genetic links through the analysis of logarithm of the odds (LOD) scores which can indicate a possible connection between those loci on the mouse chromosome and phenotypic presentation of a trait [2] linked to gallstone susceptibility such as weight, presence, severity and liver weight. Analyses were performed using the R/QTL package on a cohort of mice, in an intercross breed and fed a high-fat diet [3]. Analyses were compared between augmented data sets (to possibly prevent overfitting) and an analysis run on a non-augmented data set.

**Keywords** QTL Analysis, Gallstone Disease, Genomic Correlation

### 1. INTRODUCTION

The gallbladder is an organ in the upper right portion of the abdomen, directly below the liver, that releases bile, a fluid that the liver produces, that digests fats. Bile is a solution of cholesterol, bilirubin, and bile salts [4]. There are two primary categories of gallstones, cholesterol and pigment stones. Cholesterol stones form due to a lack of balance of cholesterol, bilirubin, and bile salts in the bile. It can form due to excess bilirubin or cholesterol or a lack of bile salts. The cause of pigment stones is currently unknown, but they tend to develop in patients already suffering from cirrhosis, biliary tract infections, and hereditary blood disorders such as sickle cell anemia [1].

While some traits are very clearly and individually linked to a single particular spot on the genome, most traits are inherently complex and thus, there are multiple locations on the genome that can influence the manifestation of that trait. Gallstone disease and susceptibility fall under that umbrella of traits. Gallstone susceptibility is a multifaceted trait influenced by both genetic and environmental factors and represents a significant health concern with considerable variability in its occurrence among individuals. The development of gallstones is associated with a complex interplay of genetic predisposition and lifestyle factors such as diet and obesity [1].

Quantitative Trait Loci (QTL) analyses can be used to find multiple locations on the genome with high logarithm of the odds (LOD) scores which can indicate a possible correlation or causation between the two. QTL analysis uses statistical methods to link quantitative phenotypic traits to genetic markers on the chromosome to try to genetically explain extremely complex phenotypes [2].

We seek to uncover QTLs that may harbor candidate genes influencing gallstone formation.

The findings from this data-driven approach not only contribute to our understanding of the genetic determinants of gallstone susceptibility but also pave the way for potential insights into personalized preventive strategies and therapeutic interventions.

## 2. DATA SET(S)

### 2.1. Setup

In this study, we used the R/qt package in R [5], developed by Bromen et. al as well as Ritsert Jansen's MQM method [6] to perform our data analysis. R is a programming language and open-source software environment specifically designed for statistical computing and data analysis. Widely used by statisticians, data scientists, and researchers, R provides a comprehensive suite of tools for data manipulation, statistical modeling, visualization, and the development of custom analytical workflows. R/qt is an R package designed for conducting Quantitative Trait Locus (QTL) analysis, a statistical method used to identify genetic loci associated with variations in quantitative traits. Developed for genetic mapping studies, R/qt provides a range of tools for analyzing experimental cross populations, facilitating the detection and characterization of genomic regions influencing complex traits.

### 2.2. Data collection

Data for this project was obtained from the Mouse Phenome Database at the Jackson Laboratory, a grant-funded resource that provides integrated genomic and phenomic data on behavioral, morphological, and physiological characteristics in mice [7]. The Jackson Lab is an independent non-profit biomedical research lab that primarily conducts genomic research with mice.

[Figure 1](#) shows an in-depth chart, demonstrating visually how the mice are bred for effective analysis. This specific dataset, the Lyons1 data set, looks at plasma lipids and gallstone susceptibility in the F2 progeny of a DBA/2J x CAST/Eij intercross. [3] There are two primary crosses of mice used for QTL analyses, intercross and backcross. As depicted by [Figure 1](#), an intercross is characterized by two homozygous mice in the parental generation bred to produce heterozygous F1 or first-filial generation children. These F1 mice are then bred together to produce the F2 generation who are then utilized in experiments and studies. An interesting side note is that all of the AA, or homozygous dominant mice in the parental generation are deeply inbred and thus genetically identical, and so are all of the BB, or homozygous recessive mice in the parental generation [8, Chapter 3, Section 2].

Only male mice were utilized in the study. The animals had unrestricted access to both food and water and were housed in a temperature-regulated environment (71.6°F - 73.4°F approximately) which had a 14 hours of light and 10 hours of dark cycle. The animals were initially fed a low-cholesterol diet until the age of 6-8 weeks when they were switched to a lithogenic, high-cholesterol diet. This diet was composed of 15 percent butterfat, 1 percent

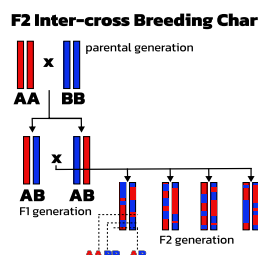


**Figure 1.** Breeding Chart for Intercross Strains

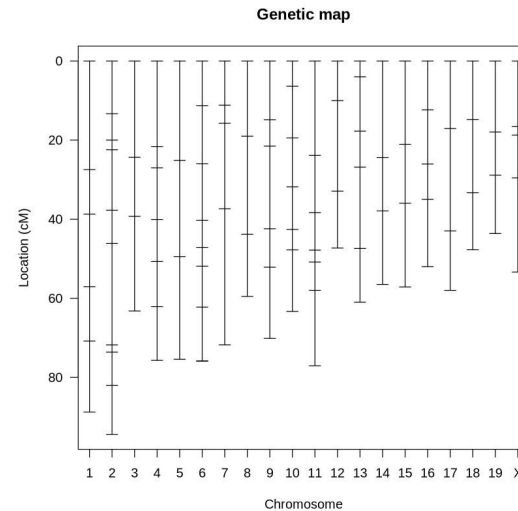


**Figure 2.** Genetic Map for Markers on Mouse Chromosome

cholesterol, 0.5 percent cholic acid, 2 percent corn oil, 50 percent sucrose, and 20 percent casein. All experimental protocols were approved by the Institutional Animal Care and Use Committees of The Jackson Laboratory and Harvard University [9].

### 2.3. Data structure

The data used was an F2 intercross with 278 individuals. There were 15 phenotypes and all 15 phenotypes had over 96.8 percent of the individual mice phenotyped. Mice have 20 chromosomes, 19 autosomes, and one sex chromosome, the X chromosome. There are 109 molecular markers in this data and the genetic map is shown above in [Figure 2](#).

There was a 97.4 percent rate of genotyping, meaning this data is extremely complete and this is shown in [Figure 3](#) below. We can see that there is very little missing data which is 2.6 percent of total data missing according to the summary function in R/qt.

Of the 15 phenotypes presented in the dataset, we chose to focus on four: a score on the severity of the gallstone, the number of gallstones measured, the weight of the gallstones, and the aggregates of the severity of cholesterol monohydrate crystals, which is a key indicator of gallstone development.

## 3. DATA PREPARATION AND MODELING

### 3.1. Data Preparation

Prior to running the analyses, we had to prepare the data further. We first completed a pairwise recombination factor plot to take a look at the physical distances between markers on the chromosome and ensure that they are accurate. We first estimate recombination fractions between markers within a genetic cross with the est.rf function. Recombination fractions are crucial in genetic mapping as they indicate the likelihood of genetic crossovers occurring between markers during the formation of gametes. These fractions are fundamental for constructing genetic maps, elucidating the distances between genetic markers, and identifying regions of the genome associated with specific traits through QTL analyses. We then generate a visual representation of the estimated

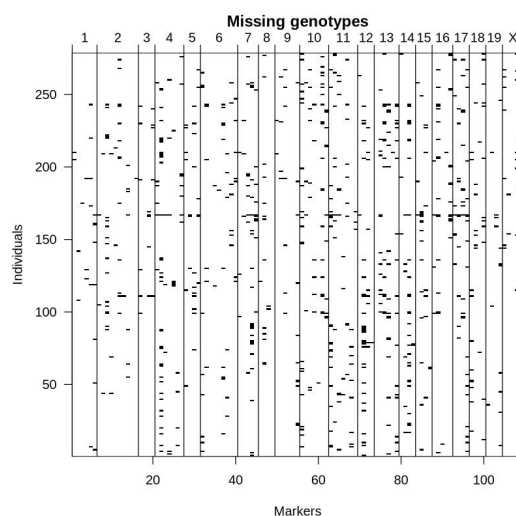


**Figure 3.** Missing Data Map

recombination fractions which is essential in understanding the genetic linkage and physical distances between markers along the chromosomes, providing researchers with insights into the genetic architecture of traits and facilitating the identification of potential genomic regions influencing complex phenotypes. We then plotted our pairwise recombination scores and LOD scores in [Figure 4](#).

As evidenced by the lack of large red spots and a clean line, this data is clean and alright to use for further analysis.

### 3.2. Exploratory Data Analysis

After cleaning our data set and ensuring quality control, we then began exploratory data analysis. The first step was using the R/ggplot2 library to explore trends within the phenotypic data. We used a correlation heat map to identify correlations between phenotypes and the manifestation of gallstones. Correlation heat maps are a visual representation of the coefficient of determination between various factors, or the r-squared value in a color-coded matrix. A value with an absolute value of 1 has a very strong

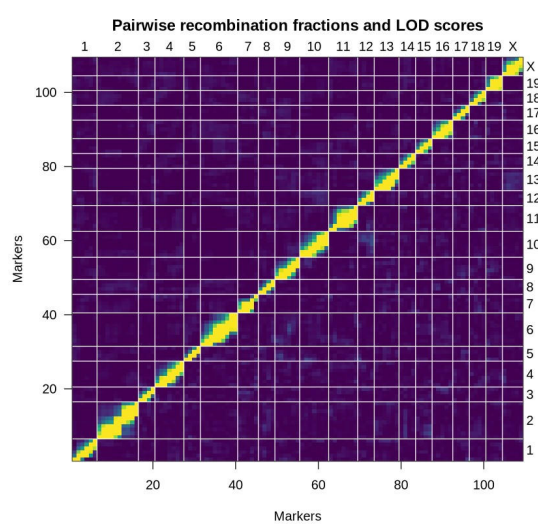


**Figure 4.** Pairwise Recombination Scores and LOD Scores

correlation, either positive or negative. A value closer to 0 has less correlation and is more random. A positive number correlates to a positive correlation, meaning as the x-value increases, so does the y-value. A negative number correlates to a negative correlation, meaning as the x-value increases, the y-value decreases. This is shown below in [Figure 5](#).

```

      pgm          liver_wt
gallstone_presence gallstone_score
  Min. :0.0000  Min.  :0.9225  Length:278
Length:278
  1st Qu.:0.0000  1st Qu.:1.3244
Class :character Class :character
  Median :1.0000  Median :1.5524
Mode  :character Mode  :character
  Mean   :0.7266  Mean   :1.6115
  3rd Qu.:1.0000  3rd Qu.:1.8027
  Max.   :1.0000  Max.   :3.2405
gallstone_count    gallstone_weight
gallstone_sandy    gallstone_solid
  Length:278       Length:278
Length:278
  Class :character Class :character
  Class :character Class :character
  Mode  :character Mode  :character
  Mode  :character Mode  :character

```

ChMC_agg HDL_log Length:278 Length:278 Class :character Class :character Mode  :character Mode  :character	ChMC_ind Length:278 Length:278 Class :character Class :character Mode  :character Mode  :character	chol nonHDL Length:278 Class :character Mode  :character
---	--	--

```

Warning message in lapply(data, as.numeric):
“NAs introduced by coercion”
Warning message in lapply(data, as.numeric):
“NAs introduced by coercion”
Warning message in lapply(data, as.numeric):
“NAs introduced by coercion”
Warning message in lapply(data, as.numeric):
“NAs introduced by coercion”
Warning message in lapply(data, as.numeric):
“NAs introduced by coercion”
Warning message in lapply(data, as.numeric):

```

3rd Qu.:1.991  
 Max. :4.000 Max. :4.0000 Max. :668.0  
 Max. :2.455  
 NA's :7 NA's :7 NA's :1  
 NA's :1  
 nonHDL  
 Min. : 8.0  
 1st Qu.:102.0  
 Median :137.0  
 Mean :158.0  
 3rd Qu.:194.5  
 Max. :631.0  
 NA's :3

```

      pgm          liver_wt
gallstone_presence gallstone_score
  Min. :0.0000   Min. :0.9225
Min. :0.0000   Min. :0.000
  1st Qu.:0.0000  1st Qu.:1.3244  1st
Qu.:0.0000    1st Qu.:0.000
  Median :1.0000   Median :1.5524
Median :1.0000   Median :2.000
  Mean   :0.7266   Mean   :1.6115
Mean   :0.6015   Mean   :1.288
  3rd Qu.:1.0000  3rd Qu.:1.8027  3rd
Qu.:1.0000    3rd Qu.:2.000
  Max.  :1.0000   Max.  :3.2405
Max. :1.0000   Max.  :2.000

NA's :7

      gallstone_count gallstone_weight
gallstone_sandy gallstone_solid
  Min. : 0.000   Min. :0.0000   Min. :0.000
Min. :0.0000
  1st Qu.: 0.000  1st Qu.:0.0000  1st Qu.:0.000
1st Qu.:0.0000
  Median : 0.000  Median :0.0000  Median :1.000
Median :0.0000
  Mean   : 1.129  Mean   :0.1508  Mean   :1.443
Mean   :0.6494
  3rd Qu.: 0.000  3rd Qu.:0.0000  3rd Qu.:3.000
3rd Qu.:0.0000
  Max.  :28.000  Max.  :3.1600  Max.  :4.000
Max. :4.0000

NA's :7           NA's :9           NA's :7
NA's :7

      ChMC_agg        ChMC_ind       chol
HDL_log
  Min. :0.000   Min. :0.0000   Min. : 67.0
Min. :1.079
  1st Qu.:0.000  1st Qu.:0.0000  1st Qu.:185.0
1st Qu.:1.806
  Median :1.000  Median :0.0000  Median :223.0
Median :1.892
  Mean   :1.601  Mean   :0.7232  Mean   :243.9
Mean   :1.901
  3rd Qu.:3.000  3rd Qu.:1.0000  3rd Qu.:285.0

```

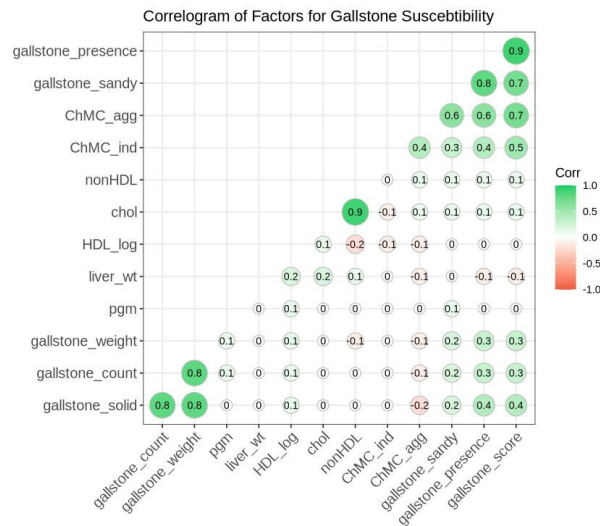


**Figure 5.** Correlation Heat Map

In this figure, we can see that there is a high positive correlation between multiple factors, particularly between the binary classification of the solidity of gallstones and the number of gallstones, the weight of gallstones and the number of gallstones, the weight of the gallstones and the binary solidity classification, and the presence of gallstones and the severity score.

We also ran a dendrogram heat map to analyze correlations as well as find hierarchical correlations between our phenotypic factors, shown in Figure 6. This map shows both a heat map to show correlations between various factors, similar to our previous graph, but also shows hierarchical relationships between our phenotypic factors. This helps us understand the degree of the relationship between the factors.

### 3.3. QTL Analyses

Following this, we can begin the setup for the QTL analysis. We first calculated the genotypic probabilities for individuals in the genetic cross by determining the likelihood of different genetic marker configurations based on specified parameters such as recombination step size, genotyping error probability, and the Haldane map function. We then simulated genotypic data for the markers in the

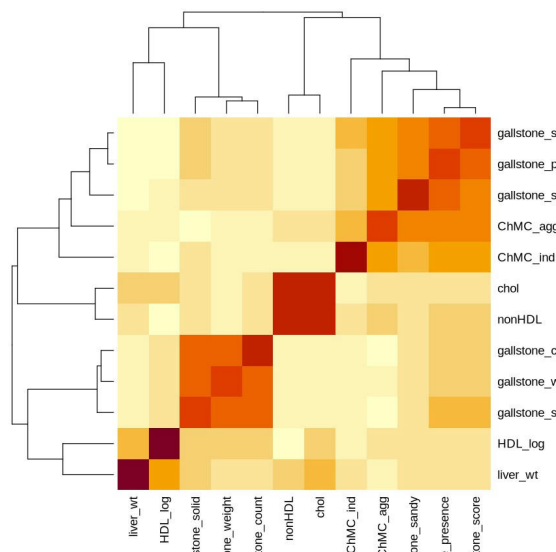


**Figure 6.** Dendrogram Hierarchical Heat Map

genetic cross, incorporating factors like recombination, genotyping errors, and mapping functions. This is the primary first step we must do prior to running any analyses and determining the locus of interest.

Following this, we completed the same steps for each of our four factors to generate a main scan analysis as well as effect plots for the highest probability locus of interest as determined by LOD scores. We first used the function scanone with a normal model and the “em” method, which is the Expectation-Maximization method which estimates missing genotype probabilities in the genetic mapping analysis. While this is specifically excellent for data sets with missing phenotypic information, we find that it is still a robust method of analysis.

For each method, we then completed a permutation on the scan with 100 permutations to assess the significance of LOD peaks for each phenotype. We then assigned threshold values based on our permutation results with confidence intervals of 95 percent, 90 percent, and 63 percent respectively. After this, we plotted the results onto a main scan plot with colored lines representing our thresholds. We also ran a summary of the scan per phenotype and identified the most probable locus of interest per scan. We then used this location to identify a molecular marker in our data set and run an effect plot. These plots are particularly useful for understanding how genetic variation at specific loci influences the phenotypic variation in a quantitative trait. We can see how homozygous recessive or dominant, or heterozygous affects the manifestation of different phenotypic traits.

Completing this, we decided to explore augmented data to see if results run on augmented data on a total QTL analysis for the data set. To do this, we first created an augmented data set derived from our cross with a minprob of 0.1. This establishes a minimum probability threshold for considering the effects of additional markers or QTLs. This threshold, which influences the augmentation step, allows us to filter out less statistically significant QTL effects, refining the model and focusing on those with higher confidence. The choice of the minprob threshold serves as a key determinant in

balancing sensitivity and specificity in the identification of quantitative trait loci, tailoring the analysis to the desired level of statistical rigor. We chose 0.1 because we wanted more statistically significant results rather than a broader overview with less statistically significant results. We then ran a geno.image on both the augmented cross and the original cross and compared the plots. Following this we took a scan of each cross, using the mqm scan for the augmented set and scanone for the original set, and found the peaks on each plot. We then found a molecular marker corresponding to each peak and compared it to each other. Following this, we used that marker we identified earlier as a cofactors and took another mqm scan with the cofactor of D18Mit64, the marker we identified. We then proceeded to plot all three main scans together on the same plot and compared the peaks.

## 4. RESULTS

### 4.1. Expectation-Maximization Model

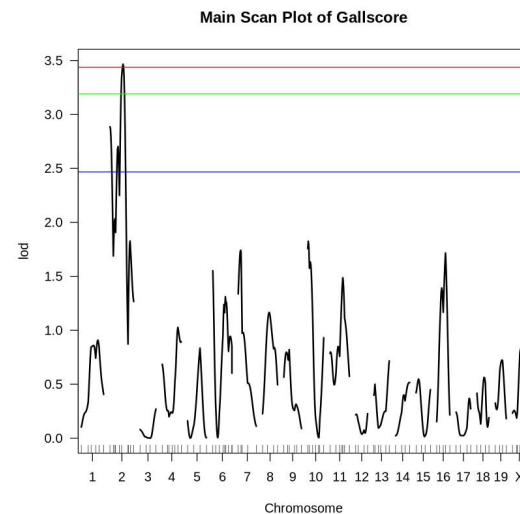
Using the Expectation-Maximization model, we generate 4 separate main scans with threshold lines at 95 percent confidence, 90 percent confidence, and 63 percent respectively.

#### 4.1.1. Gall Count:

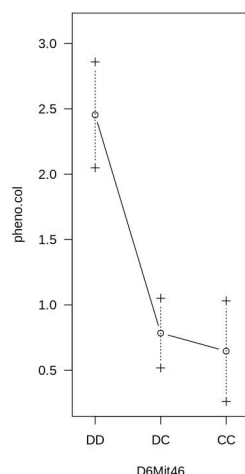
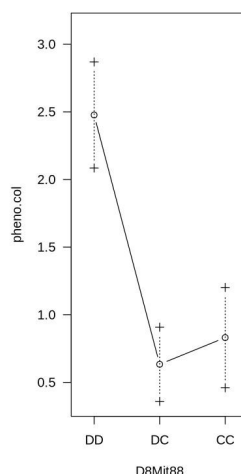
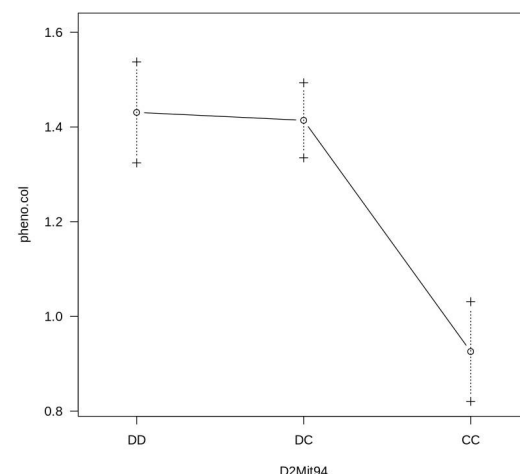
As shown below in Figure 7, for a count of gallstones present, we found two loci with a peak over 95 percent confidence.

There was 98 percent confidence in the correlation between c6.loc6 and phenotypic manifestation and 96 percent confidence in the correlation between c8.loc58 and phenotypic manifestation. We then found the correlated molecular markers for those two spots which were D6Mit46 and D8Mit88 respectively. Using those two markers, we then plotted an effect plot as shown below in Figure 8. As we can see in both figures, a homozygous DD genotype at both of these locations can correlate to gallstone susceptibility and a higher amount of gallstones while heterozygous DC and homozygous CC both present lower amounts of gallstones.

#### 4.1.2. Gall Score:



**Figure 7.** Main Scan for Gall Count

**Effect plot for D6Mit46****Effect plot for D8Mit88****Effect plot for D2Mit94****Figure 8. Effect Plot showing Allele vs Phenotypic Presentation**

As shown below in [Figure 9](#), for a score on how severe the gallstones were, we found one locus with a peak over or equal to 95 percent confidence.

There was 95 percent confidence of correlation between c2.loc52 and phenotypic manifestation. We then found the correlated molecular markers for this spot which was D8Mit88. Using this marker, we then plotted an effect plot as shown below in [Figure 10](#). As we can see, a homozygous CC genotype at this location can correlate to a lower gallstone severity score while heterozygous DC and homozygous D both present higher scores. It can be said then that high gallstone severity is a dominant trait at this location in the genome.

#### 4.1.3. Gall Weight:

As shown below in [Figure 11](#), for a score on how severe the gallstones were, we found one locus with a peak over or equal to 95 percent confidence.

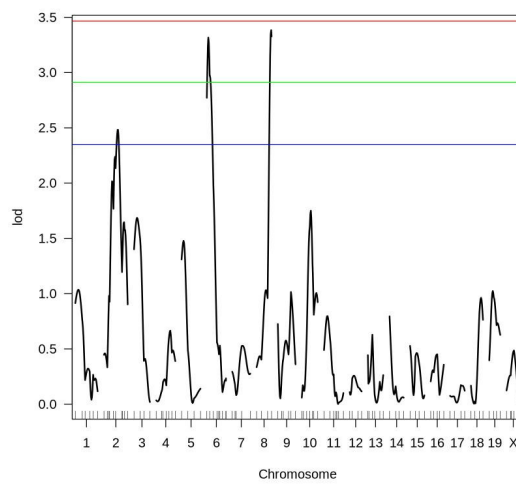
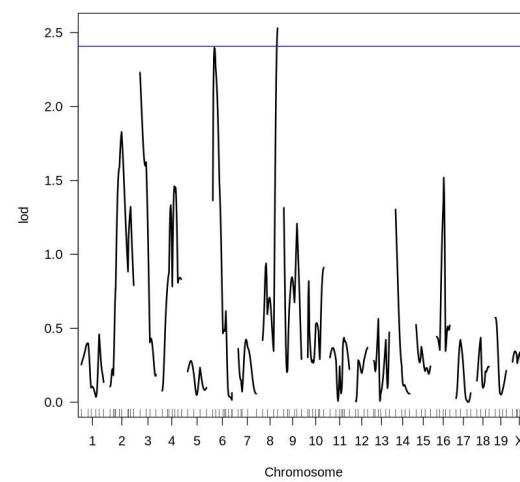
**Figure 10. Effect Plot showing Allele vs Phenotypic Presentation**

There was 95 percent confidence in the correlation between c2.loc52 and phenotypic manifestation. We then found the correlated molecular markers for this spot which was D8Mit88. Using this marker, we then plotted an effect plot as shown below in [Figure 12](#). As we can see, a homozygous DD genotype at this location can correlate to a higher gallstone weight score while heterozygous DC and homozygous C both present lower weights. It can be said then that high gallstone weight is a recessive trait at this location in the genome.

#### 4.1.4. Cholesterol Monohydrate Crystals, aggregates:

As shown below in [Figure 13](#), for a score on the cholesterol monohydrate crystals, we found one locus with a peak over or equal to 95 percent confidence.

There was 95 percent confidence of correlation between c6.loc56 and phenotypic manifestation. We then found the correlated molecular markers for this spot which was D6Mit62. Using this marker, we then plotted an effect plot as shown below in [Figure 14](#). As we can

**Main Scan Plot of Gall Count****Figure 9. Main Scan for Gall Score****Main Scan Plot of Gall Weight****Figure 11. Main Scan for Gall Weight**

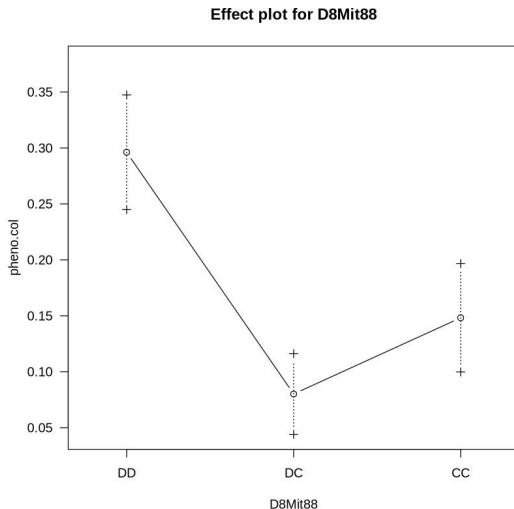


**Figure 13.** Effect Plot showing Allele vs Phenotypic Presentation

see, a homozygous DD genotype at this location can correlate to a lower cholesterol monohydrate crystal score while heterozygous DC and homozygous D both present higher scores.

#### 4.2. Augmented QTL Analyses Comparison

After generating an augmented dataset, we then used geno.image to plot both crosses respectively as shown below in [Figure 15](#).

The genotypes CC, DC, and DD are displayed in the colors red, blue, and green, respectively. The white spaces represent missing data. As we can see, the augmented data is filled in much better, and there is no missing data. While running the summary function on the data, we see that nothing has changed in the augmented as compared to this original other than there being much more individuals in the data set (1343 as compared to 278). Additionally, the percent phenotyped remains approximately the same and the percent genotyped jumps up to 100 percent.

Next, we complete an mqmscan on the augmented dataset and a scanone on the original dataset and take a look at the maximum

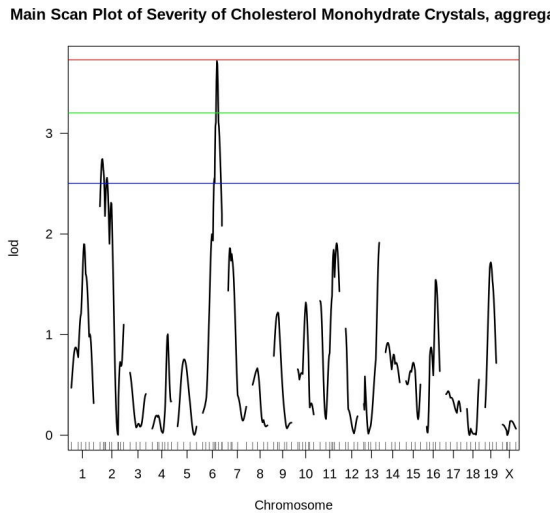


**Figure 13.** Main Scan for Gall Weight

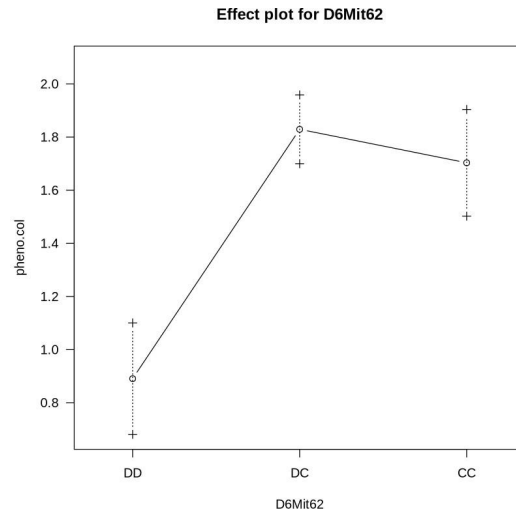


**Figure 15.** Effect Plot showing Allele vs Phenotypic Presentation

point on both of these. The augmented dataset has a peak at c18.loc5 which is 5 centimorgans on chromosome 18. The original dataset has a peak at c18.loc4 which is 8.46 centimorgans on chromosome 18. We then extract a marker for both of these positions which both are D18Mit64. We can then set that marker as a covariate and analyze for a new peak, with this marker as an additional variable.

We then plotted all three of these plots on the same map with green representing the original data, red representing the augmented data, and blue representing augmented data with the peak as a covariate, as shown in [Figure 16](#) below.

As we can see, the augmented data narrows down the peaks into only a few spots, showing how it counters overfitting due to the small nature of the original data set. As the original data set was much smaller than the augmented one, we can hypothesize that

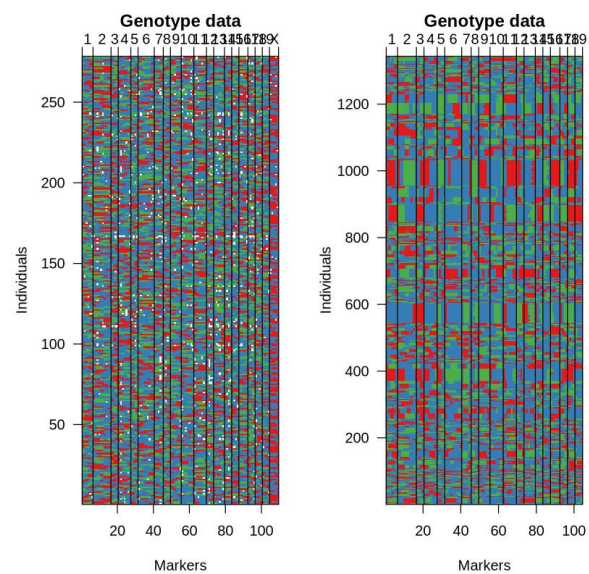


**Figure 15.** Plot Grid of Original Genotype Data (left) and Augmented Genotype Data (right)

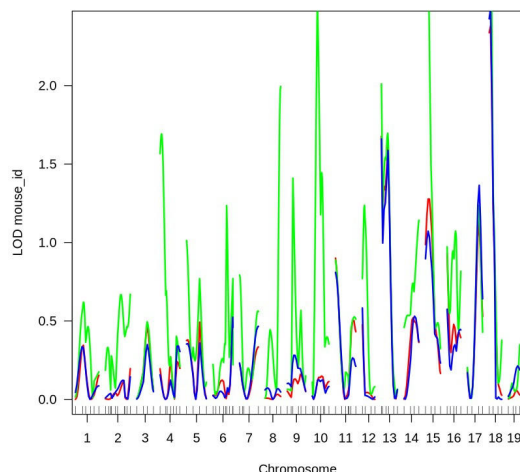


**Figure 16.** Overlayed Scans on Three Models

there are fewer peaks on the augmented model as it eliminates peaks on the original which could be due to overfitting.

## 5. DISCUSSION

In this study, we identified a great many loci of interest to investigate as shown in the table above.

These results are statistically significant as each of them passes the threshold value of 0.05 meaning that there is a 95 percent confidence rate for a correlation between that loci and the associated genotypes. In targeting this disease from a genomic standpoint, it may be worthy to first target those markers that are dominant for the associated phenotype. These would be D2Mit94 and D6Mit62. Research may be further made into chromosomes 2, 6, 8, and 18 as those are the most prominent chromosomes which correlate to increased gallstone susceptibility.

## 6. CONCLUSION

Molecular Marker	Dominant/Recessive	Threshold	Phenotype
D6Mit46	Recessive	0.05	High Gall Count
D8Mit88	Recessive	0.05	High Gall Count
D2Mit94	Dominant	0.05	High Gall Score
D8Mit88	Recessive	0.05	High Gall Weight
D6Mit62	Dominant	0.05	High Cholesterol Aggregate Crystal Formation
D18Mit64	Recessive	0.05	High Susceptibility (Augmented Data)
D18Mit64	Recessive	0.05	High Susceptibility (Original Data)

Through our comprehensive QTL analysis exploring the genomic correlation for gallstone susceptibility, we uncovered three chromosomes of interest and 2 molecular markers of interest to target first. We conducted a robust exploration using the R/qt1 package, leveraging the power of statistical methods like the Expectation-Maximization model.

Our findings illuminated several key loci with high logarithm of the odds (LOD) scores, providing significant insights into the genetic underpinnings of gallstone susceptibility. Notably, we identified loci associated with gallstone count, severity, weight, and cholesterol monohydrate crystals. The allelic variations at these loci demonstrated correlations with distinct phenotypic presentations, unraveling the complexity of genetic influences on gallstone-related traits. Furthermore, by employing an augmented dataset and comparing results with the original dataset, we sought to enhance the robustness of our analysis. The augmented data, with its increased sample size, presented a more comprehensive view of the genomic landscape associated with gallstone susceptibility. The overlay of scans from the original and augmented datasets, along with the inclusion of a covariate, provided a nuanced understanding of the genetic factors at play.

Our study contributes to the fundamental understanding of gallstone susceptibility and lays the foundation for personalized preventive strategies and therapeutic interventions. The identified QTLs harbor candidate genes that may play pivotal roles in gallstone formation, paving the way for further targeted research.

## ACKNOWLEDGMENTS

Special thanks are extended to Mr. Robert Gotwals of the North Carolina School of Science and Math and the Mouse Phenotype Database at the Jackson Laboratory.

This paper is solely the work of the author. All references are included in the bibliography and are cited appropriately.

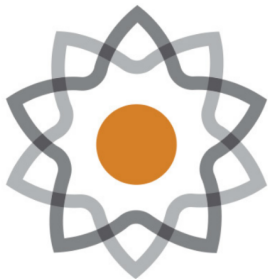
The authors declare that they have no competing interests.

The data for this work was obtained from <https://phenome.jax.org/projects/Lyons1>.

## REFERENCES

- [1] "Gallstones." [Online]. Available: <https://www.hopkinsmedicine.org/health/conditions-and-diseases/gallstones>
- [2] C. Myles and M. Wayne, "Quantitative trait locus (QTL) analysis," *Nature Education* 1 (1), vol. 208, 2008.
- [3] Lyons, "Lyons1: Plasma lipids and susceptibility to gallstones in F2 progeny of DBA/2J x CAST/Eij." [Online]. Available: <https://phenome.jax.org/projects/Lyons1>
- [4] "Gallbladder: What Is It, Function, Location & Anatomy." [Online]. Available: <https://my.clevelandclinic.org/health/body/21690-gallbladder>
- [5] K. W. Broman, H. Wu, S. Sen, and G. A. Churchill, "R/qt1: QTL mapping in experimental crosses," *Bioinformatics*, vol. 19, no. 7, pp. 889–890, 2003.
- [6] D. Arends, P. Prins, R. C. Jansen, and K. W. Broman, "R/qt1: high-throughput multiple QTL mapping," *Bioinformatics*, vol. 26, no. 23, pp. 2990–2992, 2010.
- [7] M. A. Bogue *et al.*, "Mouse phenome database: curated data repository with interactive multi-population and multi-trait analyses," *Mammalian Genome*, vol. 34, no. 4, pp. 509–519, 2023, doi: [10.1007/s00335-023-10014-3](https://doi.org/10.1007/s00335-023-10014-3).
- [8] L. M. Silver, *Mouse genetics concepts and applications*. Oxford University Press, 1995.

- [9] M. A. Lyons *et al.*, “Quantitative trait loci that determine lipoprotein cholesterol levels in DBA/2J and CAST/Ei inbred mice1, 2,” *Journal of lipid research*, vol. 44, no. 5, pp. 953–967, 2003.



# The Morganton Scientific

*North Carolina  
School of Science and  
Mathematics*

Journal of Student STEM Research

Published Jun 27, 2024

Correspondence to  
Caroline Zhang  
[zhang24c1@nessm.edu](mailto:zhang24c1@nessm.edu)

Open Access 

Copyright © 2024 Zhang. This is an open-access article distributed under the terms of the [Creative Commons Attribution 4.0 International license](#), which enables reusers to distribute, remix, adapt, and build upon the material in any medium or format, so long as attribution is given to the creator.

## Effect of Sulfakinin/Cholecystokinin-type Peptide ArSK/CCK1 on Satiety and Energy Metabolism of *Asterias vulgaris*

Caroline Zhang<sup>1</sup> 

<sup>1</sup>North Carolina School of Science and Mathematics 

### Abstract

Depression is the persistent sadness or lack of interest in previously rewarding activities and has devastating effects on much of the global population. The neuropeptide cholecystokinin (CCK) controls satiety in humans and travels along a signaling pathway related to the brain-gut axis in humans. This suggests a relationship between the pathway and experienced emotions in relation to depression. Increased levels of CCK have been correlated with increased suicide attempts, and the effects of CCK-like pathways in arthropods have exhibited an increased correlation between peptide levels and feelings of satiety. Though a similar pathway (using the ArSK/CCK neuropeptide) has been identified in the evolutionarily proximal echinoderm *Asterias rubens*, little is known about the effects of these peptide levels on depressive symptoms through observation of feeding and energy metabolism. This study observed the effect of injected ArSK/CCK1 peptide on satiety and energy homeostasis through examination of initial and final stomach eversion areas of *Asterias vulgaris*, synonymous with *A. rubens*. Energy homeostasis was observed using a constructed open-flow respirometer taking measurements, which predicted energy creation using the rate of dissolved oxygen consumption to be used for cellular respiration. Exposure to ArSK/CCK1 was found to yield lower rates of dissolved oxygen decrease compared to basal rate and control measurements, suggesting a resulting decreased satiety and rate of energy metabolism.

**Keywords** Sulfakinin, *Asterias vulgaris*, Cholecystokinin

### 1. INTRODUCTION

Depression, defined as the persistent sadness and lack of interest or pleasure in previously rewarding activities, affects much of the world today. It is one of the most prevalent mental health disorders in the United States and the second leading cause of disability worldwide, proving to be an immense global and economic burden in addition to the emotional distress felt by those affected. Some symptoms of the disease include feelings of sadness or hopelessness, sudden angry outbursts, reduced appetite, and anxiety. Despite the large quantity of research done on the topic, the exact mechanisms underlying depression are unknown. However, research has shown that changes in the gut microbiome (the variety of microorganisms living in the digestive tract) play an important role in the brain-gut axis, and thus hold influence in the neural and immune systems. More specifically, changes in the composition of the gut microbiome in mice have caused the demonstration of resilience when exposed to stress [1].

Cholecystokinin (CCK) is a neuropeptide, or chemical messenger, synthesized by neurons and involved in a signaling pathway along the brain-gut axis. The peptide hormone was discovered and named due to its stimulatory effects on gallbladder contraction as well as the gastric secretion of pepsin and acid in mammals [2]. Neuropeptides such as CCK are composed of small chains of amino acids and are synthesized and released by neurons, binding to G protein-coupled receptors to modulate tissue activity. CCK is an important moderator of food intake and energy homeostasis, having been found to generate anxiety and aggression once simulated in mice [3]. Increased levels of CCK are related to stronger feelings of satiety as well. In human patients suffering from depression, significant inverse correlations were found between CCK levels and depression and anxiety parameters. Patients who had made one or

more suicide attempts generally had higher CCK levels in their cerebrospinal fluid (CSF) than those who had not [4].

A CCK-type pathway has been discovered in a variety of insects, with similar G Protein Coupled Receptors that act as receptors for these CCK-like signaling molecules. Named sulfakinins (SKs), these neuropeptides have proven to be a family of neuropeptides homologous to mammalian CCK and caused the reduction of food intake by either direct peptide injection [5] or sk gene silencing [6], similar to the effect of CCK in mammals. The homologous nature of CCK and SK suggests that insects with SK signaling pathways can serve as model organisms utilized in the study of CCK signaling pathways [7]. Its inhibitory action on feeding in insects has been quantified and discovered to affect the regulation of insulin-like peptides and carbohydrates in insect hemolymph [8].

The presence of SK-type signaling in various insects and arthropods indicates that SK/CCK-type signaling has evolutionary origins in the common ancestor of Bilateria. These signaling systems have similarly been discovered in protostome invertebrates such as the nematode *Caenorhabditis elegans* and mollusk *Crassostrea gigas* [9], [10]. The roles of SK/CCK-type signaling in non-arthropod protostomes also play a role in digestion regulation similar to ones observed in mammals. These include a decrease in the frequency of contractions for the hindgut as well as the regulation of energy storage and feeding in *C. gigas* [11].

Sharing a position under the category of deuterostomes similar to chordates, echinodermata hold an intermediary position in the phylogenetic position between vertebrates and arthropoda, in which CCK-type signaling pathways have been commonly observed [12]. This intermediary phylogenetic position makes echinodermata a more accurate model for such pathways, as organisms share a more recent common ancestor with chordata when compared to arthropoda. CCK-type immunoreactive cells have been discovered in the intestines of sea cucumbers from the phylum echinodermata, and the use of vertebrate CCK-type peptides was also observed to cause the relaxation of sea cucumber intestines [13]. The amino acid sequences of native SK/CCK-type neuropeptides in sea cucumbers have also been identified, yielding possibilities for studies regarding its pharmacological effects in sea cucumbers [14].

*Asterias rubens*, or the common sea star, is a European starfish typically found in the northeast Atlantic Ocean. Favoured due to its wide availability, *A. rubens* has served as a model organism for processes ranging from salinity tolerance [15] to immune response [16]. Recently, a study characterized SK/CCK-type signaling for *A. rubens*, the first such characterization for non-chordate deuterostomes [17]. Two CCK-type neuropeptides (ArSK/CCK1 and ArSK/CCK2) were successfully derived from the precursor protein ArSK/CCKP and were found to travel along a similar signaling pathway. They are expressed in the nervous system, digestive system, tube feet, and body wall of *A. rubens*, causing feeding inhibition and cardiac stomach retraction similar to the observed effect of CCK-type signaling in other organisms. Comparison of the peptide sequences composing ArSK/CCK1 and ArSK/CCK2 with SK/CCK-type neuropeptides from other taxa indicate the shared presence of tyrosine (typically sulfated) and a C-terminal amide group also characteristic of most SK/CCK-type peptides [17].

Little is known about the quantitative effect of CCK-type signaling on energy homeostasis in Ambulacraria including echinoderms and hemichordates, or invertebrates in an intermediate phylogenetic position between protostomes such as arthropoda and chordates [18]. With depression, little work has been done to observe the effects of natural antidepressant compounds on the CCK-type signaling pathway in relation to energy homeostasis and feeding behavior. This experiment aims to quantitatively explore the effect of increased levels of CCK-type neuropeptides on energy homeostasis by observing the resulting changes in dissolved oxygen in the water surrounding *A. vulgaris*. This will be done by creating an open-flow respirometer and presenting a quantitative perspective on energy homeostasis as a means of predicting cellular respiration rates, with higher rates accompanied by increased dissolved oxygen consumption and vice versa. Due to the homologous nature of *A. rubens* and *A. vulgaris*, it is predicted that the SK/CCK-type neuropeptides sequenced from *A. rubens* will similarly cause cardiac stomach contraction and feeding inhibition in *A. vulgaris*. Increased levels of CCK-type peptides are predicted to cause a lower rate of dissolved oxygen decrease, thus indicating the decreased production of energy through cellular respiration.

## 2. METHODS

### 2.1. Animal Care and Maintenance

Adult *Asterias vulgaris* (synonymous with the common sea star *Asterias rubens*) were acquired from the Gulf of Maine (736 Leighton Point Rd. Pembroke, Maine 04666) and kept in a 10-gallon tank at 4.8 degrees Celsius. Saltwater was used in the tank and was prepared with 31.2 mL of InstantOcean aquarium salt for every 1 liter of distilled water. Water was chilled to aquarium temperature and conductivity was measured relating to salinity (about 30‰) before each water replacement. 3 liters of tank water were replaced once or twice a week.

Organisms were exposed to a 12-hour light/dark cycle to model their natural environments (Seaoura Aquarium Light was used) and clams were fed as a food source every 2-3 days (see Figure 1). For each feeding, clams were dropped into the tank in proximity to the organisms and were taken out the next day to prevent excessive bacterial growth. An aquarium filter (PULACO Aquarium Internal Filter) was used to maintain water condition and provide aeration to the water. The filter cartridge was replaced once every month with Tetra Whisper Bio-Bag Filter Cartridges. Temperature probes were placed in the tank and hooked up to a Vernier LabQuest sensor to monitor tank temperatures at all times.

### 2.2. Respirometer Design and Construction

An open-flow respirometer was constructed to reduce stress upon the model organism according to a basic structure described by [19] with modifications to measure oxygen consumption in relation to energy metabolism. The chamber the organism was placed in was made of a 9.6-cup plastic Rubbermaid container with holes drilled in the lid for rubber tubing. A Stepper peristaltic pump (24V) was used to cycle water throughout the system in a clockwise manner drawing water away from the chamber (at approximately 268 rpm). The water exiting the chamber entered another chamber (plastic, empty 100 mL distilled water bottle with a hole drilled in lid)



**Figure 1.** Organisms in their natural environments

containing a Vernier dissolved oxygen sensor hooked up to a Vernier LabQuest sensor monitoring dissolved oxygen levels in the closed system. This chamber was placed in a water bath to exert external pressure and prevent leakage and air exchange out of the container.

All chambers and the pump were connected via ANPTGHT  $\frac{3}{8}$ " by  $\frac{3}{8}$ " aquatic connectors (between tubes and chambers) and sealed with aquarium sealant (Loctite 2.7 oz Clear Silicone Waterproof Sealant) to prevent water and air leakage. A Horiznext brass  $\frac{3}{8}$ " O.D. three-way brass ball valve was used as the control center to control the cycling of water in the closed "loop" and "flush" cycles (oxygenated water cycled through the system). Both chambers containing organisms and the bin containing oxygenated water supply were kept on ice with salt to maintain a constant temperature during cycles. All water was cycled through the system with the same composition as the original tank water (saltwater solution) and an added 2% Magnesium chloride solution (20 g of magnesium chloride hexahydrate to every 1 L of distilled water). See [Figure 2](#) for a visualization of the respirometer.

### 2.3. In Vivo Tests on Stomach Contraction

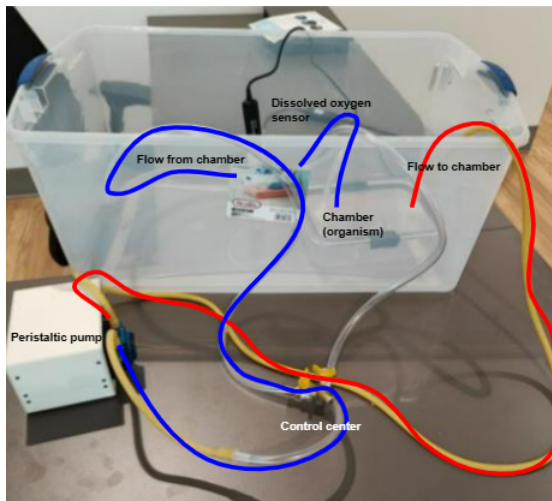


**Figure 2.** Respirometer diagram

Measurement of satiety was performed using in vivo tests observing stomach contraction. Organisms were deprived of food supply for 10 days before experimentation and placed in the organismal chamber of the respirometer and exposed to a 2% magnesium chloride solution in the organismal chamber, a marine muscle relaxant [17]. After about 30 minutes or when stomach eversion has been observed for a period of time, the chamber was closed and a cycle was run for 180 seconds. Data was tracked with the Vernier Dissolved Oxygen probe and a line of best fit was observed for the dissolved oxygen levels across the 180 seconds. The slope of the line of best fit was noted as the change in dissolved oxygen consumption (mg/L/s). This was repeated a series of times for each *A. vulgaris* of differing diameters and established their basal rate of dissolved oxygen consumption. The correlation coefficient ( $r^2$  value) was noted for each slope and only  $r^2$  values with an absolute value of 0.5 or higher were considered in data analysis. A flush cycle was used to reoxygenate the water when oxygen levels were getting low between trials and to aid in the cleaning of the respirometer.

For the control experiment, each of the *A. vulgaris* was injected with 10 microliters of distilled water for a 12 cm diameter starfish using a Model 7001KH 1 microliter Hamilton syringe. Volumes of water injected were adjusted accordingly with varied diameters of organisms and the needle was disinfected with 70% ethanol before and after use. The injections were performed with the tip of the needle facing the central disk of the organism and at the base of each arm (5 microliters at the base of one arm and 5 at the base of another, care was taken to inject the liquid into the coelomic cavity of the organism, see [Figure 3](#)). Water was cycled through in the manner described above, and flush cycles were performed to reoxygenate the water. Data was collected in accordance to the standards presented above.

The same process was repeated with 10 microliters of the neuropeptide ArSK/CCK1 (peptide sequence pQSKVDDY(SO3H)GHGLFW-NH<sub>2</sub>, synthesized by ThermoFisher) for a 12 cm starfish of the experimental group. The peptide injected was adjusted for concentration and volume and was diluted according to the diameter of the organism. The concentration of the neuropeptide was chosen due to its ability to form a more pronounced difference and caused the greatest effects on in vitro preparations of the cardiac stomach during prior experimentation [17]. Cycles were not run until an observed cardiac stomach retraction occurred, signaling the effects of the peptide had taken place and dissolved oxygen levels observed reflected this state of satiety. Data was collected in accordance to the standards presented above.

## 3. RESULTS

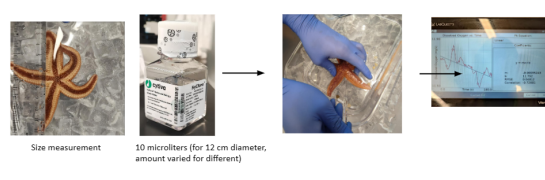


**Figure 3.** Size measurement, injection, and data collection process

### 3.1. Effectiveness of Respirometer in Measuring Dissolved Oxygen Consumption

The effectiveness of the open-flow respirometer in measuring dissolved oxygen consumption rates as a reflection of energy metabolism was observed by changes in dissolved oxygen levels in cycling water in the presence and absence of *A. vulgaris*. Rates of dissolved oxygen change in the closed system were measured in 180-second intervals across the span of several days and yielded an average rate of 0.00697 mg/L/s. All values yielded a positive value, thus indicating that dissolved oxygen was not consumed by the system.

*Asterias vulgaris* were also placed in the organismal chamber to observe rates of dissolved oxygen consumption. All rates observed across several days for each organism yielded negative values, indicating a decrease in dissolved oxygen levels with the presence of *A. vulgaris*, and thus the respirometer was an effective measurement for dissolved oxygen consumption in reflection of energy metabolism.

### 3.2. Measurement of Dissolved Oxygen Consumption

The rates of dissolved oxygen consumption were measured at basal rate, H<sub>2</sub>O injections (control), and ArSK/CCK1 injection (experimental) for each organism. Measurements for each organism of varied diameter were taken individually for groups but were averaged for consideration together with values from other organisms for final comparison across sections.

Across all organisms of varying diameters, the basal rate measurements yielded the highest rate of decrease for dissolved oxygen overall with the strongest negative values (see Fig. 4). This illustrates the highest amount of dissolved oxygen consumption and a reflected energy production in the organism. The dissolved oxygen consumption rate measurements for the control (H<sub>2</sub>O injection) fell near the measurements for the basal rate as well, tending to hold a rate slightly lower than the basal rate measurements. Dissolved oxygen consumption rates for the experimental peptide injection group showed much less change in dissolved oxygen levels, however, with rate values approaching or greater than zero. This suggests a general decrease in the amount of dissolved oxygen consumed by *A. vulgaris* under exposure to ArSK/CCK1.

The average change in dissolved oxygen consumption was taken across all organisms and averaged to achieve a value for comparison. To establish the validity of the H<sub>2</sub>O injection as a control, the average change in dissolved oxygen consumption for the basal rate and H<sub>2</sub>O injection measurements were compared. A one-tailed T-test was performed for the two means to determine if the average dissolved oxygen consumption rate for the basal rates (-0.0008728646154 mg/L/s) was significantly greater than the average rate for the H<sub>2</sub>O injection (-0.0008281736364 mg/L/s), as shown in Figure 5. A p-value less than 0.05 was acquired, thus demonstrating that the difference between the two values was not significant and factors such as the injection process or addition of fluid into the coelomic cavity did not have a significant impact on the results obtained.

The quantitative effects of exposure of ArSK/CCK1 on the dissolved oxygen consumption of *A. vulgaris* was observed by averaging the

rate values from all organisms and trials considered (see Fig. 6). This average (-0.0002312072727 mg/L/s) was compared to the average dissolved oxygen consumption rate for the basal rate group with a one-tailed t-test. A p-value greater than 0.05 was achieved, indicating that the average rate for the ArSK/CCK1 injection group was significantly lower than that of the basal rate.

## 4. DISCUSSION

This study observed the effects of cholecystokinin-type neuropeptide ArSK/CCK1 on the organism *Asterias vulgaris* with consideration of its satiety-producing effects on dissolved oxygen consumption and thus energy metabolism in the organism. In considering depressive symptoms such as appetite and energy loss, this study indicated the potential of the CCK homolog ArSK/CCK1 in studies of appetite and emotional health disorders as a reflection of the mammalian CCK.

The measurement of dissolved oxygen consumption as an indicator of energy metabolism in *A. vulgaris* was established based on its consumption in the process of cellular respiration to produce ATP for cellular processes. This measurement was performed through the construction of an open-flow respirometer utilizing a Vernier dissolved oxygen sensor which effectively monitored dissolved oxygen changes in the presence and absence of an organism. The tubes connecting the chambers and the pump were sealed with aquarium sealant in an attempt to create an airtight seal, though small amounts of oxygen were able to enter through small gaps during the cycles. This caused there to be a net gain of dissolved oxygen instead of the expected constant value, though this was worked around by comparing the experimental rates with the average net gain of the respirometer. As no dissolved oxygen consumption rates yielded a value greater than the average net gain of the respirometer, it was able to indicate the desired dissolved oxygen changes and served the purpose of this experiment.

The exposure of *A. vulgaris* to the neuropeptide ArSK/CCK1 via injection demonstrated a decreased rate of dissolved oxygen consumption when compared to measurements of basal rate. This trend was observed across *A. vulgaris* of differing diameters and slight variations in lengths of starvation time. Though a base starvation interval of ten days was applied for the organisms, the time needed for the acquisition of each data point caused some organisms to be starved for more than ten days at the time of experimentation. However, the effects of ArSK/CCK1 exposure for all organisms followed a common trend throughout experimentation regardless of specific starvation times and thus suggests that it held minimal impact on the effect of the neuropeptide on behavior.

Observations of satiety and abstinence from feeding representing appetite loss were perceived through stomach eversion amounts in 2% magnesium chloride solution. Despite the slightly differing intervals of starvation organisms were exposed to, cardiac stomach eversion was observed with exposure to the MgCl<sub>2</sub> solution before the performance of any measurements or experimental injections. In cases of injection, dissolved oxygen was able to enter the system when the organismal chamber was opened to perform experimental procedures, preventing oxygen levels in the water from getting too low in the following trials. Cardiac stomach inversion was noted

with the administration of ArSK/CCK1 as an indicator of satiety, and dissolved oxygen rate data was not collected until its effects were observed to ensure that the data collected represented its effects.

## 5. CONCLUSION

Induced appetite loss in the state of starvation has been shown to decrease energy production in relation to dissolved oxygen consumption, proving *A. vulgaris* as an adequate model for depression studies as a homolog to mammalian CCK signaling pathways. Acquisition of data points with a correlation ( $r^2$  greater than 0.5) demonstrated a correlation between the points composing a dissolved oxygen rate measurement, yielding higher confidence in the validity of the rate in reflecting the general changes in dissolved oxygen observed. This parameter also caused the elimination of many data points, however, and resulted in a smaller number of values that could be interpreted in the data. Future work would include performing increased trials and acquiring more basal rate, H<sub>2</sub>O injection, and ArSK/CCK1 injection data points.

Concentrations of ArSK/CCK1 selected in this study were based on optimal in vitro muscle contractions [17]. Varying concentrations and volumes of ArSK/CCK1 could be tested to observe its effects on energy metabolism in *A. vulgaris* and determine the relationship between peptide concentration and degree of appetite loss. While ArSK/CCK1 was tested in this study, further studies could utilize the homolog ArSK/CCK2 and observe the effects of its exposure to dissolved oxygen consumption and energy production [17].

The prospect of these signaling pathways in modeling depression opens up further questions regarding prospective treatments that target its behavior. With the establishment of *A. vulgaris* as an adequate model organism for studying ArSK/CCK1 signaling with its impact on satiety, this study observed its impact on the energy loss aspect of depression. Further research that could be done would include the observation of ancient herbal medicinal extracts such as *Ziziphus jujube* that had previously exhibited antidepressant effects in stress-related studies involving mammals [20], [21]. Oral administrations or a filtered extract administered by injection can be utilized to observe its impact on satiety and energy metabolism measurements [22].

## ACKNOWLEDGMENTS

The author would like to thank Jennifer Williams, North Carolina School of Science and Mathematics-Morganton, and Ana B. Tinoco for their guidance and support throughout the course of this project.

## REFERENCES

- [1] L. Chang, Y. Wei, and K. Hashimoto, "Brain-gut-microbiota axis in depression: A historical overview and future directions," *Brain Research Bulletin*, vol. 182, pp. 44–56, 2022, doi: [10.1016/j.brainresbull.2022.02.004](https://doi.org/10.1016/j.brainresbull.2022.02.004).
- [2] A. C. Ivy and E. Oldberg, "A HORMONE MECHANISM FOR GALL-BLADDER CONTRACTION AND EVACUATION," *American Journal of Physiology-Legacy Content*, vol. 86, no. 3, pp. 599–613, 1928, doi: [10.1152/ajplegacy.1928.86.3.599](https://doi.org/10.1152/ajplegacy.1928.86.3.599).
- [3] L. Singh, A. S. Lewis, M. J. Field, J. Hughes, and G. N. Woodruff, "Evidence for an involvement of the brain cholecystokinin B receptor in anxiety," *Proceedings of the National Academy of Sciences*, vol. 88, no. 4, pp. 1130–1133, 1991, doi: [10.1073/pnas.88.4.1130](https://doi.org/10.1073/pnas.88.4.1130).
- [4] C. Löfberg, H. Agren, J. Harro, and L. Oreland, "Cholecystokinin in CSF from depressed patients: possible relations to severity of depression and suicidal behaviour," *European Neuropsychopharmacology*, vol. 8, no. 2, pp. 153–157, 1998, doi: [10.1016/s0924-977x\(97\)00046-1](https://doi.org/10.1016/s0924-977x(97)00046-1).
- [5] Z. Wei *et al.*, "Sulfakinins reduce food intake in the desert locust, *Schistocerca gregaria*," *Journal of Insect Physiology*, vol. 46, no. 9, pp. 1259–1265, 2000, doi: [10.1016/s0022-1910\(00\)00046-9](https://doi.org/10.1016/s0022-1910(00)00046-9).
- [6] M. Meyering-Vos and A. Müller, "RNA interference suggests sulfakinins as satiety effectors in the cricket *Gryllus bimaculatus*," *Journal of Insect Physiology*, vol. 53, no. 8, pp. 840–848, 2007, doi: [10.1016/j.jinsphys.2007.04.003](https://doi.org/10.1016/j.jinsphys.2007.04.003).
- [7] N. Yu, R. J. Nachman, and G. Smagghe, "Characterization of sulfakinin and sulfakinin receptor and their roles in food intake in the red flour beetle *Tribolium castaneum*," *General and Comparative Endocrinology*, vol. 188, pp. 196–203, 2013, doi: [10.1016/j.ygcen.2013.03.006](https://doi.org/10.1016/j.ygcen.2013.03.006).
- [8] M. Słocińska, S. Chowański, and P. Marciniak, "Identification of sulfakinin receptors (SKR) in *Tenebrio molitor* beetle and the influence of sulfakinins on carbohydrates metabolism," *Journal of Comparative Physiology B*, vol. 190, no. 5, pp. 669–679, 2020, doi: [10.1007/s00360-020-01300-6](https://doi.org/10.1007/s00360-020-01300-6).
- [9] T. Janssen *et al.*, "Discovery of a Cholecystokinin-Gastrin-Like Signaling System in Nematodes," *Endocrinology*, vol. 149, no. 6, pp. 2826–2839, 2008, doi: [10.1210/en.2007-1772](https://doi.org/10.1210/en.2007-1772).
- [10] O. Mirabeau and J.-S. Joly, "Molecular evolution of peptidergic signaling systems in bilaterians," *Proceedings of the National Academy of Sciences*, vol. 110, no. 22, 2013, doi: [10.1073/pnas.1219956110](https://doi.org/10.1073/pnas.1219956110).
- [11] J. Schwartz, M.-P. Dubos, J. Pasquier, C. Zatylny-Gaudin, and P. Favrel, "Emergence of a cholecystokinin/sulfakinin signalling system in Lophotrochozoa," *Scientific Reports*, vol. 8, no. 1, 2018, doi: [10.1038/s41598-018-34700-4](https://doi.org/10.1038/s41598-018-34700-4).
- [12] D. C. Semmens, O. Mirabeau, I. Moghul, M. R. Pancholi, Y. Wurm, and M. R. Elphick, "Transcriptomic identification of starfish neuropeptide precursors yields new insights into neuropeptide evolution," *Open Biology*, vol. 6, no. 2, p. 150224–150225, 2016, doi: [10.1098/rsob.150224](https://doi.org/10.1098/rsob.150224).
- [13] J. Garcia-Arráras, I. Torres-Avillán, and S. Ortíz-Miranda, "Cells in the intestinal system of holothurians (echinodermata) express cholecystokinin-like immunoreactivity," *General and Comparative Endocrinology*, vol. 83, no. 2, pp. 233–242, 1991, doi: [10.1016/0016-6480\(91\)90026-3](https://doi.org/10.1016/0016-6480(91)90026-3).
- [14] M. Chen, A. Talarovicova, Y. Zheng, K. B. Storey, and M. R. Elphick, "Neuropeptide precursors and neuropeptides in the sea cucumber *Apostichopus japonicus*: a genomic, transcriptomic and proteomic analysis," *Scientific Reports*, vol. 9, no. 1, 2019, doi: [10.1038/s41598-019-45271-3](https://doi.org/10.1038/s41598-019-45271-3).
- [15] O. L. Sarantchova, "Research into tolerance for the environment salinity in sea starfish *Asterias rubens* L. from populations of the White Sea and Barentz Sea," *Journal of Experimental Marine Biology and Ecology*, vol. 264, no. 1, pp. 15–28, 2001, doi: [10.1016/s0022-0981\(01\)00298-2](https://doi.org/10.1016/s0022-0981(01)00298-2).
- [16] V. Matrangia, A. Pinsino, D. Randazzo, A. Giallongo, and P. Dubois, "Long-term environmental exposure to metals (Cu, Cd, Pb, Zn) activates the immune cell stress response in the common European sea star (*Asterias rubens*)," *Marine Environmental Research*, vol. 76, pp. 122–127, 2012, doi: [10.1016/j.marenvres.2011.09.008](https://doi.org/10.1016/j.marenvres.2011.09.008).
- [17] A. B. Tinoco *et al.*, "Ancient role of sulfakinin/cholecystokinin-type signalling in inhibitory regulation of feeding processes revealed in an echinoderm," *eLife*, vol. 10, 2021, doi: [10.7554/elife.65667](https://doi.org/10.7554/elife.65667).
- [18] R. F. Furlong and P. W. H. Holland, "Bayesian Phylogenetic Analysis Supports Monophony of Ambulacraria and of Cyclostomes," *Zoological Science*, vol. 19, no. 5, pp. 593–599, 2002, doi: [10.2108/zsj.19.593](https://doi.org/10.2108/zsj.19.593).
- [19] M. K. Drown, A. N. DeLiberto, D. L. Crawford, and M. F. Oleksiak, "An Innovative Setup for High-Throughput Respirometry of Small Aquatic Animals," *Frontiers in Marine Science*, vol. 7, 2020, doi: [10.3389/fmars.2020.581104](https://doi.org/10.3389/fmars.2020.581104).
- [20] J. M. Oh *et al.*, "Antidepressant-Like Effects of Ethanol Extract of *Ziziphus jujuba* Mill Seeds in Mice," *Applied Sciences*, vol. 10, no. 20, p. 7374–7375, 2020, doi: [10.3390/app10207374](https://doi.org/10.3390/app10207374).
- [21] H. J. Park *et al.*, "The ethanol extract of *Ziziphus jujuba* var. spinosa seeds ameliorates the memory deficits in Alzheimer's disease model mice," *Journal of Ethnopharmacology*, vol. 233, pp. 73–79, 2019, doi: [10.1016/j.jep.2018.12.043](https://doi.org/10.1016/j.jep.2018.12.043).
- [22] S. McLean, R. Patel, and R. Bruno, "Injection of Pharmaceuticals Designed for Oral Use: Harms Experienced and Effective Harm Reduction Through Filtration," in *Current Topics in Behavioral Neurosciences*, Springer International Publishing, 2016, pp. 77–98. doi: [10.1007/7854\\_2016\\_470](https://doi.org/10.1007/7854_2016_470).